

ABSTRACT

MATHEMATICAL MODELS AND TOOLS TO UNDERSTAND COUPLED CIRCADIAN OSCILLATIONS AND LIMIT CYCLING SYSTEMS

by
Guangyuan Liao

The circadian rhythm refers to an internal body process that regulates many body processes including the sleep-wake cycle, digestion and hormone release. The ability of a circadian system to entrain to the 24-hour light-dark cycle is one of the most important properties. There are several scenarios in which circadian oscillators do not directly receive light-dark forcing. Instead they are part of hierarchical systems in which, as “peripheral” oscillators, they are periodically forced by other “central” circadian oscillators that do directly receive light input. Such dynamics are modeled as hierarchical coupled limit cycle systems. Those models usually have a large population, and are non-autonomous. In this dissertation, a coupled Kuramoto model and a coupled Novak-Tyson model are developed to study the entrainment of hierarchical coupled circadian oscillators. Direct simulations usually are incapable of revealing the full dynamics of such models. One goal of this dissertation is to apply proper mathematical methods to simplify the original systems. A phase reduction method is applied for reducing the original system to phase model. A parameterization method is introduced for simplifying such systems, and it is also applied for computing invariant manifolds of some biological oscillators. A novel tool, entrainment map, is developed and extended to a higher dimensional situation. Compared with direct simulations, the map has the advantages of describing the conditions for existence and stability of the limit-cycle solutions, as well as studying forcing and coupling strength dependent bifurcations. It is also more practical to calculate the entrainment times by just iterating the map rather than by direct simulations.

MATHEMATICAL MODELS AND TOOLS TO UNDERSTAND
COUPLED CIRCADIAN OSCILLATIONS AND LIMIT CYCLING
SYSTEMS

by
Guangyuan Liao

A Dissertation
Submitted to the Faculty of
New Jersey Institute of Technology and
Rutgers, The State University of New Jersey – Newark
in Partial Fulfillment of the Requirements for the Degree of
Doctor of Philosophy in Mathematical Sciences

Department of Mathematical Sciences
Department of Mathematics and Computer Science, Rutgers-Newark

August 2020

Copyright © 2020 by Guangyuan Liao

ALL RIGHTS RESERVED

APPROVAL PAGE

MATHEMATICAL MODELS AND TOOLS TO UNDERSTAND COUPLED CIRCADIAN OSCILLATIONS AND LIMIT CYCLING SYSTEMS

Guangyuan Liao

Amitabha Bose, Dissertation Advisor
Professor of Mathematical Sciences, NJIT

Date

Casey O. Diekman, Committee Member
Associate Professor of Mathematical Sciences, NJIT

Date

Horacio G. Rotstein, Committee Member
Professor of Biological Sciences, NJIT

Date

Denis Blackmore, Committee Member
Professor of Mathematical Sciences, NJIT

Date

Victor Matveev, Committee Member
Professor of Mathematical Sciences, NJIT

Date

BIOGRAPHICAL SKETCH

Author: Guangyuan Liao

Degree: Doctor of Philosophy

Date: August 2020

Undergraduate and Graduate Education:

- Doctor of Philosophy in Mathematical Sciences,
New Jersey Institute of Technology, Newark, NJ, 2020
- Master of Science in Applied Mathematics,
Sichuan University, Chengdu, China, 2014
- Bachelor of Science in Mathematical Sciences,
Sichuan University, Chengdu, China, 2011

Major: Mathematical Sciences

Presentations and Publications:

Guangyuan Liao, Casey Diekman, Amitabha Bose, “Entrainment dynamics of forced hierarchical circadian systems revealed by 2-dimensional maps”, SIADS, 2020, in press.

Guangyuan Liao, “Mathematical Models and Tools for understanding the Entrainment of Hierarchical Circadian System” *SIAM Conference on Appl. Dyn. Syst.*, Snowbird, May, 2019.

Guangyuan Liao, “Entrainment dynamics of forced hierarchical circadian systems” *Dynamics Days*, Hartford, Jan, 2020.

I dedicate my dissertation work to my life of youth.

ACKNOWLEDGMENT

I would like to thank my advisor Amitabha Bose, for his immense patience, support and incredible guidance. Professor Bose has a deep understanding of both mathematics and neural biology, which has been incredibly helpful to me for my research projects. Under his guidance, I learned how to become an independent researcher and cooperate with others.

I next thank Professors Casey Diekman, Denis Blackmore, Horacio G. Rotstein and Victor Matveev, for being on my dissertation committee. Professor Diekman provided invaluable advice, assistance, and instruction during my time at NJIT. Our collaboration has been very helpful, so that I can move those results to part of my dissertation work. Professors Denis Blackmore, Horacio G. Rotstein and Victor Matveev have taught me a lot in their classes, and they are always helpful when I ask them questions about a course or my research. I also thank Professor Roy Goodman for helpful discussions.

I also thank the Department of Mathematical Sciences for giving me the financial support to pursue my PhD degree, as well as valuable teaching experience.

In addition, thanks to my fellow graduate students: Emel Khan, Matthew Moye, Yixuan Sun, Chao Chen, Yinbo Chen, Linwan Feng, Brandon Behring and Jimmie Adriazola for countless discussions and their hard work.

Finally, special thanks to my family, especially my dear mother, Lianhui Hu and my dear father, Zailin Liao. Without their support, I never would have gotten to this point.

TABLE OF CONTENTS

Chapter	Page
1 INTRODUCTION	1
1.1 Biological Background of Circadian Oscillations	1
1.2 Classical Model Reduction Techniques in Limit Cycling Systems	1
1.3 New Reduction Tools to Simplify Circadian Oscillators	2
1.4 Structure of the Dissertation	5
2 METHODS	7
2.1 Model Reduction Techniques	7
2.1.1 Classical phase reduction technique	7
2.1.2 Floquet theory	9
2.1.3 Parameterization	10
2.1.4 A more practical expression of the parameterization $P(\theta, \sigma)$	15
2.2 Numerical Methods for Computing Limit Cycles and Visualizing Manifolds	18
2.2.1 Continuation based shooting method for computing invariant manifolds of limit cycles.	18
2.2.2 Lagrangian descriptor method of visualizing invariant manifolds	21
2.3 Reduce Dimension via Maps	22
2.3.1 Poincaré map	22
2.3.2 Entrainment map	23
3 RESULTS	25
3.1 Coupled Kuramoto Model with Forcing	25
3.1.1 Hierarchical model	25
3.1.2 Define the entrainment map	26
3.1.3 The 1-D entrainment map	28
3.1.4 Conditions of entrainment	29
3.1.5 Existence of fixed points	31

TABLE OF CONTENTS
(Continued)

Chapter	Page
3.1.6 Geometrical methods for finding fixed points and manifolds	39
3.1.7 Attempt for leading order approximation	43
3.1.8 Stability of fixed points: Numerical versus analytic results	46
3.1.9 Generalization to $N + 1$ oscillators	47
3.2 Application to Higher Dimensional Models	48
3.2.1 The Novak-Tyson model	48
3.2.2 Parameterization on other systems	55
3.2.3 Coupled Novak-Tyson model	57
3.2.4 The entrained solutions of the CNT model	64
3.2.5 The O_1 -entrained map	69
3.2.6 The results of the general 2-D map	74
4 DISCUSSION	86
4.1 Summary of the Main Results.	87
4.2 Related Work	92
4.3 Future Directions	96
REFERENCES	99

LIST OF TABLES

Table	Page
3.1 Numerical Computation of the Eigenvalues of the Map at the Four Fixed Points	75

LIST OF FIGURES

Figure		Page
3.1 The 1-D entrainment map with different k values.	29	
3.2 The time course of the original system: we start the simulation with initial value $(0,0,\pi)$. Whenever θ_2 hits 3π , we turn it back to π	30	
3.3 (a) The (α_1, k) parameter space showing how the number of fixed points depends on these parameters. There is no fixed points if either parameter lies below the critical value α_c or k_c . The number of fixed points in other regions are labeled. Squares along the green curves represent actual parameter pairs that were tested during the simulation. The rest of these curves were extrapolated. The dashed lines denote the parameter value we take for the one-dimensional bifurcation curves shown in panel (b-e). (b) We fixed $k = 0.12$, by increasing α_1 , the fixed points along the green curve stay stable, while the fixed points along the other three curves are unstable. (c) $k = 0.35$. (d) $\alpha_1 = 0.1$. (e) $\alpha_1 = 0.4$	35	
3.4 (a) and (b): Contour plots of the map $F_1 - x$ and $F_2 - y$. (c) Nullclines of the 2-D map which correspond to the zero level curves of the contour plots (blue for (a) and red for (b)). Points of intersection are fixed points of the map. (d) Return time map $\rho(x, y)$. Note the similarities with panel (a). The parameter set is $k = 0.1, \alpha = 0.08$	40	
3.5 Nulclines of the 3-oscillator model for different coupling strengths: (a) $k = k_c, \alpha_1 = 0.1$. (b) Large k : $k = 2, \alpha_1 = 0.1$. (c) Large α_1 : $\alpha_1 = 2, k = 0.12$. (d) Both large: $\alpha_1 = 2, k = 2$	42	
3.6 (a) Manifolds visualization with Lagrangian descriptor. (b) The contour plot of the Lagrangian descriptor $M(y, N)$. (c) Entrainment time plot.	43	
3.7 The left panel shows the time course of the solution in one period. The right panel shows the solution in the phase plane.	51	
3.8 The red curve is $\nabla\theta$ in x direction, and the blue curve is $\nabla\theta$ in y direction.	53	
3.9 Single isochron at phase $\theta = 0$, along with two testing trajectories. . . .	54	
3.10 The left panel shows 40 isochrons of unforced NT. The right panel is a zoom in figure of the isochrons near the fixed point.	54	
3.11 The left panel shows 20 isochrons of the F-N model. The right panel is a zoom in figure of the isochrons near the fixed point.	55	
3.12 The left panel shows 30 isochrons of the M-L model. The right panel is a zoom in figure of the isochrons near the fixed point.	56	

LIST OF FIGURES (Continued)

Figure	Page
3.13 (a) Model with strict hierarchical coupling. (b) Semi-hierarchical model when both oscillators receive light input, but the light into O_2 is much weaker than the light into O_1	57
3.14 (a) The upper panel shows a schematic of the homeomorphism from the unit circle \mathbb{S}^1 to Γ_{O_1} . The lower panel shows how we construct the map in two different conditions; the left one shows the case when the phase angle θ associated with the trajectory of O_1 rotates through more than 2π , the right one is where the rotation is less than 2π . (b) In both panel schematics, the first blue vertical line segment denotes where we chose the initial phase of light. After time $\rho(x_n, y_n)$, the trajectory returns to \mathcal{P} , and the new phase of light is y_{n+1} . For the upper panel, $y_n + \rho(x_n, y_n) > 24$, so $y_{n+1} = y_n + \rho(x_n, y_n) - 24$. For the lower panel, $y_n + \rho(x_n, y_n) < 24$, so $y_{n+1} = y_n + \rho(x_n, y_n)$. The black square wave $f(t)$ in both panels represents the LD forcing.	61
3.15 (a) The periodic solutions of O_1 in DD, LL and LD conditions. The dashed black trajectory represents the DD limit cycle ($f(t) \equiv 0$), the dashed red trajectory represents the LL limit cycle ($f(t) \equiv 1$). The solid trajectory represents the LD solution with green hourly markers. The two different P_1 nullclines, N_{P_D} and N_{P_L} and the single M_1 nullcline, N_M are shown. Note that for panels (a) and (c) the horizontal scale is much larger than the vertical scale. (b) The time course plots: P_1 vs t in all three cases (blue line lies at 0, 1 or is a square wave for DD, LL or LD, respectively. (c) The periodic solutions of O_2 when O_1 is in DD, LL and LD conditions. Same color scheme as in (a). The Poincaré section is represented at $P_2 = 1.72$ by a small vertical line segment. Note that only the maximal and minimal sigmoidal M_2 nullclines, N_M^{min} and N_M^{max} , are shown that bound the family of nullclines that exist for this case. (d) The time course plots: P_2 vs t in DD, LL and LD conditions.	66
3.16 (a) The cobweb diagram for the O_1 -entrained map. We pick two different initial conditions and show how the iterates move to the stable fixed point. (b) The approach to the stable solution (black curve) in the t vs P plane; the colors correspond to the two initial conditions in (a). (c) The map displays a saddle-node bifurcation by decreasing α_1 . (d) Decreasing the intrinsic period of O_2 by decreasing ϕ_2 also leads the map to display a saddle-node bifurcation. Fixed points shown as open circles are unstable, and those shown with solid circles are stable. . . .	71

LIST OF FIGURES (Continued)

Figure	Page
3.17 Non-monotonicity in the entrainment map leads to convergence initially due to phase delay but ultimately due to phase advance. (a) The non-monotone O_1 -entrained map and two choices of initial conditions near the local maximum. Note that the local maximum lies above the value of the fixed point of the map. (b) The return time plot associated with the two initial conditions. (c) The corresponding phase plane. The solid blue trajectory for $y_0 = 8$ does not approach the left branch of N_P , while the solid red trajectory for $y_0 = 6$ does, causing its evolution to slow down. (d) Starting with an initial condition $y_0 = 18$, the first four iterates phase delay. The fourth iterate lands near the local max of the map, and subsequent iterates then phase advance.	73
3.18 (a) and (b) The 2-D entrainment map is plotted as two separate maps Π_1 and Π_2 , and projected onto the domain space (x_n, y_n) . The purple and red color in both maps denote all points that are above the diagonal plane. The grey color denotes points that are below the diagonal plane. The white curves denote the discontinuity. (c) The purple curves denote points of Π_1 's nullcline N_x where $x = \Pi_1(x, y)$, the red curves denote points of Π_2 's nullcline N_y where $y = \Pi_2(x, y)$. Their intersections are the four fixed points of the map. (d) The entrainment time is plotted with a heatmap. The color denotes the entrainment time starting from a specific initial condition. The light green curves locate $W^s(B)$ and $W^s(C)$ from near which the longest entrainment times occur.	77
3.19 (a) $N = 10$ iterates from various initial points are shown. The arrows at each coordinate point in the direction of the next iterate. The vector field indicates that there may exist a separatrix type structure at both points B and C. (b) Stable and unstable manifolds of B and C as generated through the generalization of the search circle and growing methods (see text). The labeled manifolds do appear to provide a separatrix type behavior despite this being a map and not a flow.	79
3.20 Direction of entrainment depends sensitively on initial conditions. (a) The initial point (labeled 1) in the left panel lies above $W^s(C)$, while the similarly labeled point in the panel to the right lies below $W^s(C)$. Numbers indicate iterates. As shown, the direction of entrainment differs significantly. (b) Corresponding simulations agree with the iterates. Note the top panel shows that O_2 (red time course) entrains through phase delay to the entrained solution (black time course); the lower panel shows O_2 entraining through phase delay-advance.	81

LIST OF FIGURES
(Continued)

Figure	Page
3.21 (a)-(b) The x and y nullclines under different α_1 values. Solid circles denote unstable fixed points, open circles stable fixed points, and stars saddle points. (c)-(d) The heatmap of entrainment times for different values of α_1 . Note the difference in numeric value of the maximum value of the color scale.	83
3.22 2-D semi-hierarchical case. (a)-(b) The top view of Π_1 and Π_2 are presented; see Figure 3.18a and 3.18b for an explanation of color coding. (c) we obtained 4 fixed points (A,B,C,D) with similar stability of the canonical model. (d) Ten iterates of each point. The vector field looks qualitatively similar to the strictly hierarchical case shown in Figure 3.19a.	85

CHAPTER 1

INTRODUCTION

1.1 Biological Background of Circadian Oscillations

Circadian rhythms refer to a variety of oscillatory processes that occur over a roughly 24-hour time period. Circadian oscillations are found in a variety of animal and plant species [5]. In humans a common example involves our core body temperature which shows a local minimum typically in the early morning hours ($\sim 4:00$ AM) and a local maximum roughly twelve hours later [31]. Similarly, concentrations of certain hormone levels within our bodies oscillate over the course of a day [23]. In the absence of any explicit forcing from naturally occurring light-dark cycles, circadian oscillators possess endogenous periods of roughly 24 hours. Their ability to also entrain to 24-hour periodic cycles of light and dark is one of their most important properties.

1.2 Classical Model Reduction Techniques in Limit Cycling Systems

The models for circadian oscillations are often developed as a system of ODEs, which has a limit cycle solution in its phase space (Novak-Tyson model [54, 46], Gonze model [22], Kim-Forger [28]). The ability of a circadian system to entrain to the light-dark cycle is modeled by adding external forcings to the original system. For such non-autonomous, multi-dimensional models, direct simulation is incapable of revealing the full dynamics. Model reduction techniques play a very important role in the analysis.

The phase reduction method was one of the most famous classical methods, as formulated in Winfree's book [55], where he studied biological synchronization. The phase reduction method is capable of studying nonlinear oscillations under weak perturbations. With this method, the full dynamics of the original system are reduced to study the phase dynamics. For a detailed introduction to the theory, the paper of

Brown et al. [8] is a good reference. A brief introduction is also provided in Chapter 2.

Another interesting tool is the parameterization method [9]. The idea of parameterization is to find a coordinate change, such that the original coordinate system is mapped to the phase-amplitude coordinate system. It is usually applied for finding invariant manifolds of fixed points. For a system with a periodic orbit, parameterization of the manifolds associated to the limit cycle is useful and often simplifies the original system. Cabré et al. [9] generalized the parameterization method for periodic orbits. It has been shown to be useful in computing isochrons of a limit cycle, where Guillamon et al. [11] provides a practical numerical strategy. This method is also introduced in Chapter 2, and then some applications are presented in Chapter 3.

The last and important tool is the Poincaré map, which is widely used to study dynamics near a periodic orbit. In the dissertation, the idea of map will be widely used as described below.

1.3 New Reduction Tools to Simplify Circadian Oscillators

While there exist several tools for studying circadian oscillations, there is still a need for the development of others. Traditionally, phase response curves (PRCs) have mostly been used to understand entrainment. However, to predict entrainment properties due to periodic light-dark forcing, the perturbations must be weak such that the oscillators can relax back to the DD or LL limit cycle when the light is off within one LD cycle. PRC based methods also rely on short duration perturbations. In the case of circadian oscillators, the light duration lasts longer such that the limit cycle might not relax back to its DD or LL limit cycle, the PRCs may lose accuracy in this situation. Diekman and Bose [14] show that PRCs do not accurately predict the phase of entrainment in three different mathematical models of circadian

clocks that are subjected to 12-h:12-h light-dark (12:12 LD) cycles. A tool, which is not based on perturbing the DD or LL oscillators, is required. The entrainment of circadian oscillators has been mathematically analyzed using a variety of techniques. Often this involves describing the circadian oscillator with a reduced phase description such as that given by a Kuramoto oscillator [7, 33]. The problem then reduces to studying periodically forced Kuramoto systems. Other approaches include deriving model equations that retain more of their connection to the underlying biological process [54, 46]. Recently Diekman and Bose [14] introduced a novel tool called the entrainment map to determine whether a circadian oscillator can entrain to the 24-hour light-dark cycle, and if so, at what phase. The derived map is equivalent to a 1-D Poincaré map that tracks the phase of light onset of the light-dark forcing on a cycle-by-cycle basis. In principle, the dimension of the underlying circadian oscillator model is not relevant. Diekman and Bose derived entrainment maps for the 2-D Novak-Tyson model [54, 46], the 3-D Gonze model [22] and the 180-D Kim-Forger model [28]. In general, the map can be used to estimate both entrainment times and whether entrainment occurs through phase advance or delay with respect to the daily onset of lights.

There are several scenarios in which circadian oscillators do not directly receive light-dark forcing [22, 24, 35]. Instead they are part of hierarchical systems in which, as “peripheral” oscillators, they are periodically forced by other “central” circadian oscillators that do directly receive light input. Cells within major organs in our bodies fall into this category. Several natural questions arise about the entrainment process of these peripheral oscillators. For example, do they entrain through phase advance or phase delay as central oscillators do? To what extent is their entrainment time dependent on the entrainment process of the central oscillator from which they receive forcing? To study such questions, we generalize the entrainment map to a 2-D map

where we track from the perspective of the peripheral oscillator both the phase of the central oscillator as well as the phase of light onset.

In this dissertation, we first consider the situation in which a single central oscillator receives light-dark input. In turn, this central oscillator sends input to a single peripheral oscillator. To focus on the mathematical aspects of the derivation and analysis of the 2-D entrainment map. A hierarchical coupled Kuramoto oscillator is studied as our first model, where we put the Poincaré section on the peripheral oscillator, track the phase of light and the central oscillator. Then we utilized the planar Novak-Tyson model [46] for both the central and peripheral oscillators. The phase space for this problem is 5-D, two for each of the oscillators and a fifth that accounts for the light-dark forcing. We will define a Poincaré section transversal to the flow allowing us to derive a 2-D map that determines the phase of light and the phase of the central oscillator at each cycle when the peripheral oscillator lies on the Poincaré section. We analyzed the map by extending techniques first introduced in Akcay et al [1, 2]. We will show that for a range of parameter values, the map possesses four fixed points: one asymptotically stable and three unstable fixed points, two of which are saddle points. All of these fixed points are related to actual periodic orbits of the flow. By numerically calculating entrainment times (defined precisely later in the text), we are able to uncover how the stable and unstable manifolds of the saddle points organize the iterates of the map, determine the direction of entrainment and give rise to a rich set of dynamics. The findings of the map are then validated by comparing them to direct simulations of the model equations. We also extend the analysis to the case of a semi-hierarchical system that consists of a second central oscillator that receives less light input than the first central oscillator.

Analysis of the map reveals several important insights into the entrainment and reentrainment process. First, bounds on important parameters, such as the intensity of light input and the strength of the coupling from the central oscillator

that lead to entrainment, are easily identified. We are able to determine which kinds of perturbations lead to faster or slower reentrainment, e.g., whether perturbations that desynchronize only the peripheral oscillator but not the central one lead to quick reconvergence. Interestingly, we found that the straightforward notion of convergence via phase advance or phase delay needs to be generalized. Indeed, the peripheral oscillator can converge by a combination of phase advance and delay while the central oscillator typically converges by either phase advancing or delaying. This result has implications for recovery from jet lag and abrupt changes in sleep-wake schedules. In experimental studies of aircrews, some subjects experienced internal dissociation with different components of the circadian system converging in opposite directions [29]. Specifically, after an eastbound flight across nine time zones, activity rhythms reentrained through phase advances while body temperature reentrained through phase delays. In hospital studies, a 12-hour phase shift of sleep time results in a phase advance of urinary potassium but a phase delay in urinary hydroxycorticosteroids [37]. Aschoff [4] referred to this behavior as “reentrainment by partition” and suggested that it may impact health and contribute to the degradation of psychomotor performance observed on post-flight days. The saddle fixed points of our map provide a dynamical explanation for the partitioning phenomenon, as will be elaborated upon in the Discussion.

1.4 Structure of the Dissertation

The full structure of the Dissertation is the following. In the first chapter, the background of circadian rhythm and some existing models and tools are introduced in Section 1.1-1.2. Our motivation of developing new tools for circadian models are stated in Section 1.3. The main theory and numerical methods are developed in Chapter 2. In Section 2.1, the phase reduction method, Floquet theory, and the parameterization method are well posed. In Section 2.2, numerical methods for

computing limit cycle and manifolds are derived. In Section 2.3, the classical Poincaré map and the idea of developing entrainment map are described. Then the main results are collected in Chapter 3. They are divided into three parts, coupled Kuramoto model, coupled Novak-Tyson model and visualization of invariant manifolds. At last in Chapter 4, a conclusion of the research work and their possible future directions are discussed.

CHAPTER 2

METHODS

2.1 Model Reduction Techniques

2.1.1 Classical phase reduction technique

In math biology, many models are related to systems of ODEs with a limit cycle solution. The phase reduction technique [18, 27] has been widely used in the analysis of limit cycle oscillators. For completeness, a brief introduction to phase reduction is provided.

Consider a dynamical system in \mathbb{R}^n

$$\dot{x} = f(x), \quad (2.1)$$

which has a limit cycle solution $\gamma(t)$ with period T . The idea of the phase reduction is to define a new variable: phase, such that each point on the phase plane has the same asymptotic phase as a point on $\gamma(t)$. To do that, first we define phase on the limit cycle. Since the limit cycle is a closed curve in the space, we can topologically map it onto a unit circle, and define the phase as the angle θ , where $\theta \in \mathbb{S}^1$.

$$\theta(\gamma(t)) := \omega t = \frac{2\pi}{T} \cdot t \quad (2.2)$$

T is defined as the period of the original system. We can then define the phase for points not on $\gamma(t)$ asymptotically.

Definition 1. $\forall x_0 \in \mathbb{R}^n$, if there is a point $\gamma(t_0) \in \gamma$, such that $\lim_{t \rightarrow \infty} \|\varphi(t, x_0) - \gamma(t_0 + t)\| = 0$, then we say that $\theta(x_0) = \theta(\gamma(t_0))$.

The dynamics of the original system is simply reduced as

$$\dot{\theta} = \omega = \nabla\theta \frac{dx}{dt} = \nabla\theta f(x). \quad (2.3)$$

Now suppose there is a small perturbation.

$$\dot{x} = f(x) + \epsilon g(x, t) \quad (2.4)$$

Then the phase equation is

$$\dot{\theta} = \nabla\theta \frac{dx}{dt} = \nabla\theta[f(x) + \epsilon g(x, t)] = \omega + \epsilon \nabla\theta g(x, t). \quad (2.5)$$

If x is near the limit cycle, we can use $\nabla\theta(\gamma(t))$ to approximate $\nabla\theta(x)$. The x variable in $g(x, t)$ is also approximated by $\gamma(t)$. There are many methods to determine $\nabla\theta(\gamma(t))$, here we only introduce the adjoint method [18]. Define $x = \gamma + y$, where y is a small perturbation to the limit cycle, the variation equation is

$$\dot{y} = Df(\gamma)y + O(||y||^2) \quad (2.6)$$

Then define the phase shift as

$$\Delta\theta = \theta(x) - \theta(\gamma) = \langle \nabla\theta(\gamma), y \rangle + O(||y||^2) \quad (2.7)$$

Because the change of θ is independent of time, the left hand side is zero when we take a time derivative.

$$\begin{aligned}\frac{d\Delta\theta}{dt} &= 0 = \left\langle \frac{d\nabla\theta(\gamma)}{dt}, y \right\rangle + \left\langle \nabla\theta, \frac{dy}{dt} \right\rangle \\ 0 &= \left\langle \frac{d\nabla\theta(\gamma)}{dt}, y \right\rangle + \left\langle \nabla\theta, Df(\gamma)y \right\rangle \\ \left\langle -Df(\gamma)^T \nabla\theta, y \right\rangle &= \left\langle \frac{d\nabla\theta(\gamma)}{dt}, y \right\rangle\end{aligned}\tag{2.8}$$

y is nonzero, so

$$\frac{d\nabla\theta(\gamma)}{dt} = -Df(\gamma)^T \nabla\theta.\tag{2.9}$$

This can be solved numerically with an initial condition from (2.3):

$$\nabla\theta(\gamma(0))f(\gamma(0)) = \omega\tag{2.10}$$

In fact, the phase reduction is a coordinate change to phase variables that simplified the analysis of the original systems [8]. As long as the perturbation is $O(\epsilon)$ small, the phase reduction works well as the trajectory stays in the basin of attraction of the limit cycle. But if the perturbation is not so weak, the assumption of this method breaks down.

2.1.2 Floquet theory

Gaston Floquet developed the theory for the solutions of time dependent linear systems of ordinary differential equations [20]. The theory is applied for the stability of limit cycle solutions. It also provides a coordinate change for simplification of the original systems. In this section, a brief introduction for Floquet theory is presented.

We will show that the phase reduction method is an application of the Floquet theory.

Consider the following system:

$$\dot{x} = A(t)x, \quad x(0) = x_0, \quad x \in \mathbb{R}^n, \quad (2.11)$$

where the matrix A is a time dependent periodic function, $A(t+T) = A(t)$. Define $\Phi(t)$ as the fundamental matrix solution of the system, where $\Phi(t)$ solves

$$\dot{\Phi} = A(t)\Phi, \quad \Phi(0) = I. \quad (2.12)$$

An important quantity is the value of $\Phi(t)$ at one period, which is defined as

Definition 2. *The monodromy matrix, $M := \Phi(T)$*

Given an initial condition $x(0) = x_0$, then by the definition of the fundamental matrix solution, $x(T) = \Phi(T)x_0 = Mx_0$. If we then let $x(T)$ as initial condition of (2.12):

$$\dot{x} = A(t)x, \quad x(0) = x(T) = Mx_0. \quad (2.13)$$

We can show that $x(2T) = M^2x_0$. Hence, the stability of the solution of such system actually depends on the convergence of M^n , which is then related to study the eigenvalues of M . The eigenvalues of M are defined to be the **Floquet multipliers**.

If x_0 is the eigenvector of M with eigenvalue λ , then

$$x(T) = Mx_0 = \lambda x_0 = e^{\ln \lambda} x_0. \quad (2.14)$$

Here $\frac{\ln \lambda}{T}$ is called **Floquet exponent**.

Theorem 1. (*Floquet*) Let M be the monodromy matrix of system 2.11 and $TB = \ln M$. Then there is a T -periodic matrix \mathcal{P} such that

$$\Phi(t) = \mathcal{P}(t)e^{tB}. \quad (2.15)$$

Notice that, \mathcal{P} could be complex functions for the real linear system. The following lemma give a way to avoid it.

Lemma 1. There exists a $2T$ -periodic real matrix function $\mathcal{Q}(t)$ and a real matrix R which satisfies $M^2 = e^{tR}$ such that

$$\Phi(t) = \mathcal{Q}(t)e^{tR}. \quad (2.16)$$

The solution (2.16) is also called the Floquet normal form of system (2.11) [12].

2.1.3 Parameterization

With the Floquet normal form, we can find a coordinate change such that the original variables are simplified to phase and amplitude variables. Following [12], a brief explanation is provided in the following.

Suppose we have a dynamical system with external forcing:

$$\frac{dx}{dt} = f(x) + \epsilon g(x, t), \quad x \in \mathbb{R}^n \quad (2.17)$$

and the corresponding unforced system

$$\frac{dx}{dt} = f(x) \quad (2.18)$$

has a T -periodic solution denoted by $\Gamma \stackrel{\text{def}}{=} \{\gamma_\theta(t) = \gamma(t + \theta) : t \in [0, T]\}$, where $\theta \in (0, T)$ is the initial phase angle of Γ , let $x(t) = \gamma_\theta(t) + y(t)$, $\|y\| < 1$, we linearize (2.18) near $\gamma_\theta(t)$, and get the variational equation as below:

$$\begin{cases} \dot{y} = Df(\gamma_\theta(t))y \\ y(0) = y_0 \end{cases} \quad (2.19)$$

This is exactly a nonautonomous linear system like (2.11) if we let $A(t) = Df(\gamma_\theta(t))$. Additionally, for such system derived from the linearization near Γ , an important theorem [42] states that:

Theorem 2. *The monodromy matrix of system (2.19) always has at least one eigenvalue equal to one. Additionally, the corresponding eigenvector is $\dot{\gamma}(t)$.*

Eigen decomposition Now the Floquet theory can be applied to simplify the dynamics of system (2.19). To be specific, simplifying the dynamics means we would like to find a parameterization, such that the parameterized space has simpler dynamics for understanding. To do that, consider any points $x(0)$ on the phase space of the unforced system (2.18), and the isochron of such system is defined to be $\mathcal{I}(\theta) := \lim_{t \rightarrow \infty} \|x(t) - \gamma_\theta(t)\| = 0$. If $x(0) \in \mathcal{I}(\theta)$, then we can write $x(0) = \gamma_\theta(0) + y(0) = \gamma(\theta) + y(0)$. Now we choose θ as a parameter, and the dynamics of y satisfies (2.19). We would like to find a parameterization of y to simplify the dynamics of (2.19) one step further. From the Floquet theory, there is a

Floquet normal form for the fundamental matrix solution $\Phi(t)$ (see Equation (2.16)).

According to it, we apply a time dependant change of variables:

$$y = \mathcal{Q}(t)z, \quad (2.20)$$

substitute it into (2.19) to obtain

$$\begin{aligned} \frac{d\mathcal{Q}z}{dt} &= A(t)\mathcal{Q}z \\ \dot{\mathcal{Q}}z + \mathcal{Q}\dot{z} &= A(t)\mathcal{Q}z \\ \dot{z} &= \mathcal{Q}^{-1}(A(t)\mathcal{Q} - \dot{\mathcal{Q}})z \end{aligned} \quad (2.21)$$

We also know that $\Phi(t)$ is a solution of (2.19), so:

$$\begin{aligned} \frac{d\mathcal{Q}e^{tR}}{dt} &= A(t)\mathcal{Q}e^{tR} \\ \dot{\mathcal{Q}}e^{tR} + \mathcal{Q}Re^{tR} &= A(t)\mathcal{Q}e^{tR} \end{aligned} \quad (2.22)$$

Hence

$$\dot{\mathcal{Q}} = A(t)\mathcal{Q} - \mathcal{Q}R. \quad (2.23)$$

Substitute (2.23) into (2.21), we have

$$\dot{z} = Rz. \quad (2.24)$$

Now the system can be reduced one step further. Suppose we know that the eigenpair of R is $(\mu_i, u_i), \forall i = 1, \dots, n$, we define a coordinate change

$$z = U\sigma, \quad (2.25)$$

where U is the matrix combination of the eigenvectors, then (2.24) becomes

$$\begin{aligned} U\dot{\sigma} &= RU\sigma \\ \dot{\sigma} &= U^{-1}RU\sigma = \mu\sigma. \end{aligned} \quad (2.26)$$

According to the change of coordinates and the definition of θ , The simplified vector field in (θ, σ) space is obtained:

$$\dot{\theta} = \omega, \quad \dot{\sigma} = \mu \cdot \sigma, \quad \mu := \begin{pmatrix} \mu_1 \\ \ddots \\ \mu_i \\ \ddots \\ \mu_s \end{pmatrix} \quad (2.27)$$

Here $\mu_i = \frac{\ln \lambda_i^2}{T} < 0$ is the stable Floquet exponent of (2.19), λ_i is the Floquet multipliers.

Now a parameterization (θ, σ) for stable foliations of γ is formulated as

$$\begin{aligned} x &= P(\theta, \sigma) = \gamma(\theta) + \mathcal{Q}(\theta)U\sigma \\ &= \gamma(\theta) + \sum_{i=1}^n \sigma_i u_i(\theta), \end{aligned} \quad (2.28)$$

where $u_i(\theta) = \mathcal{Q}(\theta)u_i$. The dynamics of $x \in \mathbb{R}^n$ is transformed to the dynamics in the (θ, σ) space, which is a cylinder. If we can find the parameterization, we can then write the flow explicitly by

$$\varphi(t, P(\theta, \sigma)) = P(\theta + \omega t, \sigma e^{\mu t}). \quad (2.29)$$

Computing the parameterization (2.28) requires $\mathcal{Q}(t)$ and u_i . $\mathcal{Q}(t)$ can be obtained by solving (2.23).

Remark: This parameterization gives a linear normal bundle of the invariant manifolds of the limit cycle γ_θ . The full parameterization in the basin of attraction has been introduced by Shirasaka et al. [52], where they applied koopman operator. Higher order approximation of the parameterization is introduced by [10], where they introduced a fourier-power series.

Theorem 3. *The eigenvectors u_i of R are identical to the eigenvectors of the monodromy matrix.*

Proof: From lemma 1, we know that

$$M^2 = e^{TR}. \quad (2.30)$$

Multiply by u_i , we have

$$M^2 u_i = e^{TR} u_i = e^{T\mu_i} u_i. \quad (2.31)$$

Since $\mu_i = \frac{\ln \lambda_i^2}{T}$,

$$M^2 u_i = \lambda_i^2 u_i \quad (2.32)$$

This theorem is useful for our numerical implementation. When computing the eigenvector of R , we only need to compute the eigenvector of the monodromy matrix.

Properties of the parameterization The parameterization has the following nice properties:

- $P(\theta, 0) = \gamma(\theta)$
- $\forall \sigma$, fix θ_0 , $P(\theta_0, \sigma)$ denotes the linear approximation of isochron $\mathcal{I}(\theta_0)$.
- $\forall \theta$, fix σ_0 , $P(\theta, \sigma_0)$ denotes the linear approximation of isostable curves.

Reduction for system with external forcing Now the parameterization is applied to the forced system (2.17). It can also be viewed as a generalization of phase reduction [8].

$$\begin{aligned}\frac{d\theta(x)}{dt} &= \nabla\theta(x)\frac{dx}{dt} = \nabla\theta(x)[f(x) + \epsilon g(x, t)] = \omega + \epsilon\nabla\theta(x)g(x, t) \\ \frac{d\sigma(x)}{dt} &= D\sigma(x)\frac{dx}{dt} = D\sigma(x)[f(x) + \epsilon g(x, t)] = \mu\sigma + \epsilon D\sigma(x)g(x, t)\end{aligned}\tag{2.33}$$

By phase reduction method, $\nabla\theta(x) = \nabla\theta(\gamma(t))$ can be solved locally with adjoint method near the limit cycle:

$$\begin{aligned}\frac{d\nabla_{\gamma_0(t)}\theta}{dt} &= -Df^T(\gamma_0(t))\nabla_{\gamma_0(t)}\theta \\ \nabla_{\gamma_0(0)}\theta \cdot F(\gamma_0(0)) &= \omega.\end{aligned}\tag{2.34}$$

We can also assume that $D\sigma(x) = D\sigma(\gamma(t))$ near Γ . Next we derive a computable formula for $D\sigma(\gamma(t))$.

Derivation: Linearize equation (2.17) near $\gamma(t)$, and keep the linear term of $f(x)$:

$$\dot{y} = Df(\gamma(t))y + \epsilon g(x, t) + o(y^2).$$

Ignore $o(y^2)$, then plug in $y = \mathcal{Q}(t)z$.

$$\dot{Q}z + Q\dot{z} = Df(\gamma(t))Qz + \epsilon g(x, t).$$

Since $QR = Df(\gamma(t))Q - \dot{Q}$, we have

$$\dot{z} = Rz + \epsilon Q^{-1}g(x, t).$$

Notice that $z = U\sigma$, we have

$$\dot{\sigma} = \mu\sigma + \epsilon U^{-1}Q^{-1}g(x, t). \quad (2.35)$$

Compare it with (2.33), we get

$$D\sigma(\gamma(t)) = U^{-1}Q^{-1}(t). \quad (2.36)$$

2.1.4 A more practical expression of the parameterization $P(\theta, \sigma)$

From above, we applied Floquet normal form theory to obtain a formula for $P(\theta, \sigma)$, which is linear in σ . In this section, we will follow the general parameterization theory of invariant manifold (see [12]) to get a more practical formulation for $P(\theta, \sigma)$.

Consider system (2.18), which has a stable limit cycle solution $\gamma(\theta)$ with period T . Our goal is to find a parameterization for the isochrons of the $\gamma(\theta)$. From the previous section, we would like the parameterized space (θ, σ) to obey the following dynamics:

$$\begin{aligned}\dot{\theta} &= \omega \\ \dot{\sigma} &= \mu\sigma,\end{aligned}\tag{2.37}$$

where $\theta \in \mathbb{S}^1$, and $\sigma \in \mathbb{R}^+$, $\mu = \frac{\ln \lambda}{T}$ where λ represents the Floquet multiplier less than one. We plug $x = P(\theta, \sigma)$ into (2.18)

$$\begin{aligned}\dot{x} &= D_\theta P \dot{\theta} + D_\sigma P \dot{\sigma} = f(P(\theta, \sigma)) \\ D_\theta P \omega + D_\sigma P \mu \sigma &= f(P(\theta, \sigma)),\end{aligned}\tag{2.38}$$

which is the invariance equation for $P(\theta, \sigma)$.

In order to compute P , we seek a power series

$$P(\theta, \sigma) = \sum_{n=0}^{\infty} P_n(\theta) \sigma^n.\tag{2.39}$$

We substitute (2.39) into (2.38) and equate the coefficients of σ to obtain a formal solution of $P(\theta, \sigma)$.

For σ^0 , we have

$$\omega \frac{dP_0(\theta)}{d\theta} = f(P_0(\theta)),\tag{2.40}$$

which means that $P_0(\theta) = \gamma(\theta)$. Notice that, because of the arbitrary of initial phase, $P_0(\theta) = \gamma(\theta + a)$ is also a solution for any number $a \in \mathbb{S}^1$.

Equating terms of σ^1 , we have

$$\omega \frac{dP_1(\theta)}{d\theta} + P_1(\theta)\mu = Df(P_0(\theta))P_1(\theta). \quad (2.41)$$

We define an operator $\mathcal{L} = \omega \frac{d}{d\theta} - Df \circ P_0(\theta)$, such that

$$\mathcal{L}P_1(\theta) = -\mu P_1(\theta). \quad (2.42)$$

Hence, $P_1(\theta)$ is an eigenfunction of \mathcal{L} with the eigenvalue $-\mu$. Notice that the homogeneous equation of (2.42) is the first variational equation of (2.18). From the Floquet theory, it has a fundamental periodic matrix solution $\Phi(\theta)$, and $\Phi(2\pi)$ is the monodromy matrix.

Then by eigenproblem theory, it is easy to show that $\Phi(\theta)e^{-\mu\theta}$ is the fundamental solution of (2.42). We want to choose a proper initial condition $P_1(0)$, such that the solution of (2.42) is non-trivial. Notice that $P_1(0)$ satisfies

$$P_1(0) = P_1(2\pi) = \Phi(2\pi)e^{-2\pi\mu}P_1(0). \quad (2.43)$$

So there is a non-trivial solution if $e^{2\pi\mu}$ is an eigenvalue of the monodromy matrix. So far, we can conclude that if we choose $P_1(0)$ as a eigenvector of the monodromy matrix associate with the eigenvalue $e^{2\pi\mu}$. $P_1(\theta)$ is determined and written as

$$P_1(\theta) = \Phi(\theta)e^{-\mu\theta}P_1(0). \quad (2.44)$$

So far, the result is consistent with the result from the parameterization derived by Floquet normal form. Actually, (2.28) is the first two terms of the general series expansion.

Next we write down the invariance equations for terms of $\sigma^n, n \geq 2$,

$$\omega \frac{dP_n}{d\theta} + n\mu P_n = Df \circ P_0 P_n + R_n, \quad (2.45)$$

where R_n is a computable polynomial of $P_i, i = 0, 1, \dots, n-1$. If we apply the operator \mathcal{L} , it becomes

$$(\mathcal{L} + n\mu)P_n = R_n. \quad (2.46)$$

Such system is well known and solvable. For detailed analysis of solvability and convergence condition, one can look Cabré et al. [9]. For numerical strategy, Fourier series is often applied for $P_n(\theta)$ (Guillamon et al. [25]). In this dissertation, the linear approximation will be applied for the models discussed in Chapter 3. The equation (2.28) can be expressed in the practical way

$$x = P(\theta, \sigma) = \gamma(\theta) + \sigma e^{-\mu\theta} \Phi(\theta) \vec{u} + o(\sigma^2), \quad (2.47)$$

where $\mu < 1$ is the stable eigenvalue of the monodromy matrix, and \vec{u} is the corresponding eigenvector. This formula is more computable and is easy applied to compute the isochrons (and isostables). A numerical method based on (2.47) is introduced in the following section.

2.2 Numerical Methods for Computing Limit Cycles and Visualizing Manifolds

2.2.1 Continuation based shooting method for computing invariant manifolds of limit cycles.

In this section, we present a continuation based shooting method to compute the isochrons of any limit cycles in \mathbb{R}^2 . This method is a combination of Osigna's method [48] and the backward intergration method from Izhikevich [27].

Suppose $\varphi(t, x)$ is the flow of the autonomous system:

$$\frac{dx}{dt} = F(x), \quad x \in \mathbb{R}^n \tag{2.48}$$

which has a limit cycle with period T . In order to solve for the limit cycle, we can derive a boundary value problem

$$\begin{aligned} \frac{dx}{dt} &= F(x) \\ x(0) &= x(T). \end{aligned} \tag{2.49}$$

We solve this BVP by shooting, the idea is the following:

Start with any initial condion T_0 and x_0 , we want to shoot for the period T of limit cycle, and an initial condition x such that $x(0) = x(T)$, where $T = T_0 + \Delta T, x = x_0 + \Delta x$. By the definition of the limit cycle, we have

$$\begin{aligned} \varphi(T, x) &= x \\ \varphi(T_0 + \Delta T, x_0 + \Delta x) &= x_0 + \Delta x. \end{aligned} \tag{2.50}$$

Linearize the left hand side, we have an equation for Δx and ΔT .

$$\begin{aligned} \varphi(T_0, x_0) + \frac{\partial \varphi}{\partial t} \Big|_{T_0, x_0} \cdot \Delta T + \frac{\partial \varphi}{\partial x} \Big|_{T_0, x_0} \cdot \Delta x &= x_0 + \Delta x \\ \left(\frac{\partial \varphi}{\partial x} \Big|_{T_0, x_0} - \mathbf{I} \right) \Delta x + \frac{\partial \varphi}{\partial t} \Big|_{T_0, x_0} \cdot \Delta T &= x_0 - \varphi(T_0, x_0). \end{aligned} \quad (2.51)$$

To compute Δx and ΔT , we need to know $\frac{\partial \varphi}{\partial x} \Big|_{T_0, x_0}$ and $\frac{\partial \varphi}{\partial t} \Big|_{T_0, x_0}$.

For $\frac{\partial \varphi}{\partial t} \Big|_{T_0, x_0}$, it is the slope of the flow at $t = T_0$, which satisfies

$$\frac{dx}{dt} \Big|_{T_0, y_0} = \frac{\partial \varphi}{\partial t} \Big|_{T_0, x_0} = F(\varphi(T_0, x_0)) = F(x_0). \quad (2.52)$$

For $\frac{\partial \varphi}{\partial x} \Big|_{T_0, x_0}$, consider taking x derivative of (2.48):

$$\frac{\partial}{\partial x} \left(\frac{d\varphi}{dt} \right) = \frac{\partial}{\partial x} (\mathbf{F}(\varphi)) \Rightarrow \frac{d}{dt} \left(\frac{\partial \varphi}{\partial x} \right) = D_x \mathbf{F}(\varphi) \frac{\partial \varphi}{\partial x} \quad (2.53)$$

with initial condition $\varphi(0, x_0) = x_0$, $\frac{\partial \varphi}{\partial x}(0, x_0) = I$. (2.52) is actually the initial value problem of the original system, (2.53) is the first variational equation. By solving Equation (2.52) and (2.53), we obtain $\frac{\partial \varphi}{\partial t}$ and $\frac{\partial \varphi}{\partial x}$ at (x_0, T_0) . Now we have (2.51) in hand, which is n equations. To actually solve for Δx and ΔT , we need one more equation. There are several ways of giving this condition (see chapter 7 of [51]), here we use the orthogonality condition. We have the following recurrence linear system:

$$\begin{pmatrix} \frac{\partial \varphi}{\partial x}[T_{k-1}, x_{k-1}] - \mathbf{I}, & F[x_{k-1}] \\ F^T[x_{k-1}] & 0 \end{pmatrix} \begin{pmatrix} \Delta x_k \\ \Delta T_k \end{pmatrix} = \begin{pmatrix} x_{k-1} - \varphi[T_{k-1}, x_{k-1}] \\ 0 \end{pmatrix}. \quad (2.54)$$

The periodic solution is obtained when $\Delta x_k \rightarrow 0$, $\Delta T_k \rightarrow 0$, as $k \rightarrow \infty$. Numerically, we just need Δx_k and ΔT_k less than a small controlling number. The period of the limit cycle is given by $T_k = T_{k-1} + \Delta T_k$, and $\frac{\partial \varphi}{\partial x}(T_{k-1}, x_{k-1})$ gives the corresponding monodromy matrix, as well as a numerical approximation of the fundamental matrix solution. The limit cycle is obtained when integrating the initial value problem (2.52). Notice that the initial phase of the obtained limit cycle is determined by $\mathcal{I}(x_0)$.

Remark: After applying the numerical method, the periodic orbit is calculated, as well as the fundamental matrix solution of the variational equation. This means the Floquet normal form is ready for computing too! Therefore, the parameterization introduced in Section 2.1.3 is ready for formulation.

Grow isochrons by continuation. From solving the recurrence equations (2.54), the limit cycle and the fundamental matrix solution of the first variational equation $\Phi(t)$ are obtained, where the corresponding monodromy matrix is $M = \Phi(T)$. The eigenpair μ and \vec{u} in Equation (2.47) is easy to obtain. Therefore, the linear approximation of the isochrons are defined as the following,

$$\tilde{\mathcal{I}}(\theta) = P(\theta, \sigma), \forall \sigma < \epsilon. \quad (2.55)$$

In the numerical implementation, the initial segment of an isochron is selected at $\theta = 0$.

$$\tilde{\mathcal{I}}(0) = P(0, \sigma), \sigma = -\epsilon, \epsilon \quad (2.56)$$

Two points on the line segment are chosen to be an initial condition as our initial approximation of the isochron at $x(0)$, where ϵ is a small number. This defines a line segment

$$l := [P(0, -\epsilon), P(0, \epsilon)]. \quad (2.57)$$

Starting with this line segment l , we integrate the system backwardly for a short amount of time τ , so that we get a new line segment l_1 , which is close to the isochron of $\mathcal{I}(x(-\tau))$. The distance between the two points on l_1 is longer than that on l , an additional point is added if the distance is greater than a certain bound. The new point is selected as the middle point of the original points. Then l_1 is used as the initial segment, keep integrating backwardly until time T . We will get a number of new points for isochron at $\theta = 0$. So that we can continue this process to extend the isochrons to the whole basin of attraction. This method is applied to compute the isochrons of various biological systems in the next chapter.

2.2.2 Lagrangian descriptor method of visualizing invariant manifolds

In this small section, we will introduce a numerical method called Lagrangian descriptors. This method was first introduced in [40]. It was shown that this tool is able to provide a global dynamical picture of the geometric structures and their stable and unstable manifolds for arbitrary flows and maps. Additionally, the implementation is relatively simple compared to other methods. We will precisely define the term "Lagrangian descriptor", and we will apply it on a map we derived for the coupled Kuramoto model in chapter 3. Consider a general smooth vector field.

$$\frac{dx}{dt} = f(x, t), x \in \mathbb{R}^n, t \in \mathbb{R} \quad (2.58)$$

In the original definition, the Lagrangian descriptor is a measure of a certain arclength of the trajectory. Suppose we have a trajectory $x(t)$, $x(0) = y$, for a time interval $[-\tau, \tau]$, the Lagrangian descriptor is defined as

$$M(y, \tau) = \int_{-\tau}^{\tau} \sqrt{\sum_{i=1}^n \left(\frac{dx_i(t)}{dt} \right)^2} dt = \int_{-\tau}^{\tau} \|f(x(t), t)\| dt. \quad (2.59)$$

Lagrangian descriptor for maps For a map, the Lagrangian descriptor can be defined similarly [39]. A map is defined as

$$x \mapsto F(x), x \in \mathbb{R}^n. \quad (2.60)$$

Suppose we have an orbit $\{x_i\}_{-N}^N$, $x_0 = y$, the Lagrangian descriptor is

$$M(y, N) = \sum_{i=-N}^{N-1} \|x_{i+1} - x_i\|. \quad (2.61)$$

Function of the Lagrangian descriptor To understand why $M(y, \tau)$ is useful for revealing the geometric structures of the vector field, consider two initial conditions y_1, y_2 in that phase space. If y_1, y_2 are close enough, then so are $M(y_1, \tau), M(y_2, \tau)$. But this is not true when we choose two points on different dynamical regions of the vector field. For example, two regions separated by a stable manifold of a fixed point. $M(y, \tau)$ will have a qualitative difference on the boundary. Hence, the derivative of M along these boundaries is discontinuous. Such properties reveal the stable manifold of the fixed point.

2.3 Reduce Dimension via Maps

2.3.1 Poincaré map

To study the dynamics of limit cycling system, the theory of Poincaré map is a strong and widely used technique. In this section, the definition and advantages of the Poincaré map is briefly introduced.

A map in dynamical system is a discrete system, which can be written as $x_{n+1} = \Pi(x_n)$. In contrast to the flow, the orbit of a map is no longer a continuous function $x(t)$, it is instead a sequence of points $x_n : n \in N$.

The Poincaré map is a map derived for flows. Suppose we have a system

$$\dot{x} = f(x), x = (x_1, \dots, x_n) \in \mathbb{R}^n \quad (2.62)$$

with a solution of $\varphi_t(x)$. Take a $n - 1$ dimensional surface of section \mathbb{S} , such that the vector field of the flow is not tangent to \mathbb{S} . Now we can define the Poincaré map on \mathbb{S} . Choose any point $x \in \mathbb{S}$, and apply it as an initial condition of the flow, we seek a point $x' \in \mathbb{S}$, such that

$$x' = \varphi_{\rho(x)}(x), \quad (2.63)$$

where $\rho(x)$ is the time required for x to first return to \mathbb{S} .

Remark: If every point in the phase plane \mathbb{R}^n crosses \mathbb{S} and will eventually return after a certain amount of time, we call \mathbb{S} is a global section, and the corresponding Poincaré map is well defined. If the crossing is under certain conditions, we call that \mathbb{S} is a local section.

Advantages of studying map: First, the Poincaré map can reduce at least one dimension of the original system. Second, the map can provide insight into the global dynamics of the original system. Third, many concepts that are hard to explain

directly from the original problem can be explained via the Poincaré map, such as the existence of unstable limit cycles. Last, the stability of limit cycle can be analyzed by computing the linear stability of the Poincaré map numerically.

2.3.2 Entrainment map

Deriving the entrainment map is one of the major parts of this dissertation. The entrainment map is a generalized Poincaré map, which is usually developed for coupled biological oscillators. Suppose for system (2.62), a Poincaré section is taken at $x_1 = s_1$, the corresponding Poincaré map is defined as

$$y' = F(y), y = (x_2, \dots, x_n) \in \mathbb{R}^{n-1}. \quad (2.64)$$

This reduces the dimension of the system by one. The idea of entrainment map is to reduce more dimensions of the Poincaré map by understanding the geometry of the original system. In the Results chapter, the detail of developing the entrainment map for coupled Kuramoto oscillators and coupled Novak-Tyson oscillators will be introduced.

CHAPTER 3

RESULTS

3.1 Coupled Kuramoto Model with Forcing

We first study a coupled Kuramoto system. Each oscillator is already described as a phase model, so we don't need any methods of simplification (such as phase reduction and parameterization). Therefore, we can focus on the analysis of the mappings. The entrainment range for certain parameters, the numbers of fixed points and the stability of fixed points are studied.

3.1.1 Hierarchical model

A system of $N + 1$ oscillators is considered. The first, defined by the variable θ_0 , is simple time keeper for the 24 hour light-dark (LD) cycle. The other N oscillators are taken from the Kuramoto model [33], which is widely used to describe the phase of an oscillator. Each of these oscillators has its own intrinsic frequency and they are coupled together through sine function interactions based on the differences in their phases based on a hierarchical structure. Namely, oscillator 1 receives input from the LD oscillator θ_0 . Oscillator $n + 1$ receives input from oscillator n ($n \geq 2$). The equations that define the model are

$$\begin{aligned}\frac{d\theta_0}{dt} &= \omega \\ \frac{d\theta_1}{dt} &= \omega_1 + kf(\theta_0)\sin(\theta_0 - \theta_1) \\ \frac{d\theta_i}{dt} &= \omega_i + \alpha_{i-1}\sin(\theta_{i-1} - \theta_i), \quad i = 2, \dots, N.\end{aligned}\tag{3.1}$$

The frequency of the light-dark forcing is $\omega = 2\pi/24$ since the period of one day is $T = 24$. The intrinsic frequencies ω_i are taken to lie in a neighborhood of ω and

need not be the same. Each of these phase variables can be viewed as taking on values either in \mathcal{R} or restricted to any 2π interval. We will interchangeably use both interpretations depending on the context. We will study how solutions depend on the two parameters k , the strength of the light-dark forcing to θ_1 , and α_i , the strength of the forcing from θ_{i-1} to θ_i . The function $f(\theta) = \text{Heaviside}(\sin(\theta))$.

3.1.2 Define the entrainment map

To define the entrainment map, first we define an N -dimensional global section $\mathcal{P} = \{(\theta_0, \theta_1, \dots, \theta_N) : \theta_N = \pi\}$ of the flow of (3.1). On this section, $\theta_N = \pi$, thus leaving the θ_0 and θ_i , $i = 1, \dots, N - 1$ values to be determined. On the Poincaré section \mathcal{P} , we define $x = \theta_0$, $y = \theta_1$ and $z_i = \theta_i$, $i = 2 \dots N - 1$. Starting with a point on the section, flow forward in time until the trajectory returns to \mathcal{P} and denote this time as $\rho = \rho(x, y, z, k, \alpha)$, where $z = (z_2, \dots, z_{N-1})$ and $\alpha = (\alpha_1, \dots, \alpha_{N-1})$. Note that this time measures how long it takes oscillator N to complete one 2π cycle and is obtained by integrating the third equation of (3.1) with $i = N$. The new phases of x of the LD cycle, of y and z of oscillators 1 to $N - 1$ are obtained by integrating (3.1) from 0 to the return time ρ and performing a mod 2π operation. Therefore the N -dim entrainment map is defined:

$$\begin{aligned} x &\mapsto F_1(x, y, z, k, \alpha) := x + \omega\rho \bmod 2\pi \\ y &\mapsto F_2(x, y, z, k, \alpha) := y + \omega_1\rho + kI_1 \bmod 2\pi \\ z_i &\mapsto F_{i+1}(x, y, z, k, \alpha) := z_i + \omega_i\rho + \alpha_{i-1}I_i \bmod 2\pi, \end{aligned} \tag{3.2}$$

where $I_1 = \int_0^\rho f(\theta_0) \sin(\theta_0 - \theta_1) dt$ and $I_i = \int_0^\rho \sin(\theta_{i-1} - \theta_i) dt$, $i = 2, \dots, N - 1$. Because of the mod operation in both variables and periodicity, the phase space is actually a torus $S_1 \times \dots \times S_1$. When we focus on the case of $N = 2$, we will visualize

this phase space on the square where the edges $x = 0$ and $x = 2\pi$ are identified as are the lines $y = 0$ and $y = 2\pi$.

A fixed point (x^*, y^*, z^*) of the entrainment map corresponds to a periodic phase locked solution of the system (3.1). The value x^* determines the phase of lights when oscillator N is at \mathcal{P} . This is a proportion of the 24 hour cycle. We are assuming that the LD cycle is broken up into 12 hours of light, $\theta_0 \in (0, \pi)$ and 12 hours of darkness, $\theta_0 \in (\pi, 2\pi)$. The value y^* yields the phase of oscillator 1 at the fixed point relative to oscillator N , where $y^* - \pi \in (-\pi, \pi)$ can be interpreted as the phase difference of the two oscillators measured at each cycle and similarly for the oscillators corresponding to z^* . Note that since the evolution of each θ_i is not constant this phase difference may vary over the length of one cycle before returning to the original difference once oscillator 2 returns to \mathcal{P} . We will show that the entrainment map can possess anywhere from 0 to 2^N fixed points depending on the choice of parameters k and α_i . Using standard linearization techniques we will assess the stability of these fixed points to show how their characteristics organize the iterate structure of the map. Further, we will show how the system transitions through various bifurcations as it transitions between different qualitative regimes in parameters space.

While most of our results hold for the $N + 1$ dimensional system of oscillators, we will illustrate many of our results in the case of three oscillators, θ_0 , θ_1 and θ_2 . This represents the simplest hierarchical structure in which we can identify the individual contributions of the strength of the LD forcing, k , and of the coupling between oscillators, α_1 . In the following subsections, we first show numerical results for the 1-dim map, we then derive necessary conditions for entrainment. Finally, we derive analytical conditions for the existence and stability of fixed points of the 2-dim entrainment map for the three oscillator simplification. With this smaller network we will show how the system goes passes through different types of bifurcations as a function of k and α_1 .

3.1.3 The 1-D entrainment map

Consider the case of the LD forcing with strength k acting on oscillator 1. Here we are taking $\alpha_i = 0$ for all i . We place the Poincaré section at $\theta_1 = \pi$ and compute the return time $\rho = \rho(x, k)$. The 1-dimensional entrainment map is then simply given by the first equation of (3.2). In Figure 3.1, we show this map for several values of the strength k of the LD forcing. First note two distinct characteristics of the map: one, it is piecewise increasing with a discontinuity due to the mod operation; and two, it is periodic in that the value of the map at the boundaries $x = 0$ and $x = 2\pi$ are the same. If k is too small, then the map does not intersect the diagonal and there are no fixed points. In this case entrainment is not possible. But as k increases, the map shifts down and two fixed points are created through a saddle-node bifurcation at roughly $k = 0.09$. The exact value will be labeled in the section below as k_c . As k increases further the map begins to flatten out near the value π for larger parts of the domain, while the discontinuity shifts to the right. Because of the periodic boundary conditions, this implies there is a very small range of initial conditions over which the map has a very steep gradient (see the $k = 0.4$ curve). The flattening out of the map makes sense since as the LD forcing becomes stronger, almost all initial conditions quickly get entrained to the LD forcing and the values of θ_0 and θ_1 become identical. Since the x value of the map is the value of θ_0 and the map updates whenever $\theta_1 = \pi$, this implies that $x = \pi$. Using a singular perturbation argument, it can be shown that in the limit as $k \rightarrow \infty$, the discontinuity of the map converges to 2π , while $F_1(x, k) = x + \omega\rho \rightarrow \pi$. Thus, in this limit only a single stable fixed point exists.

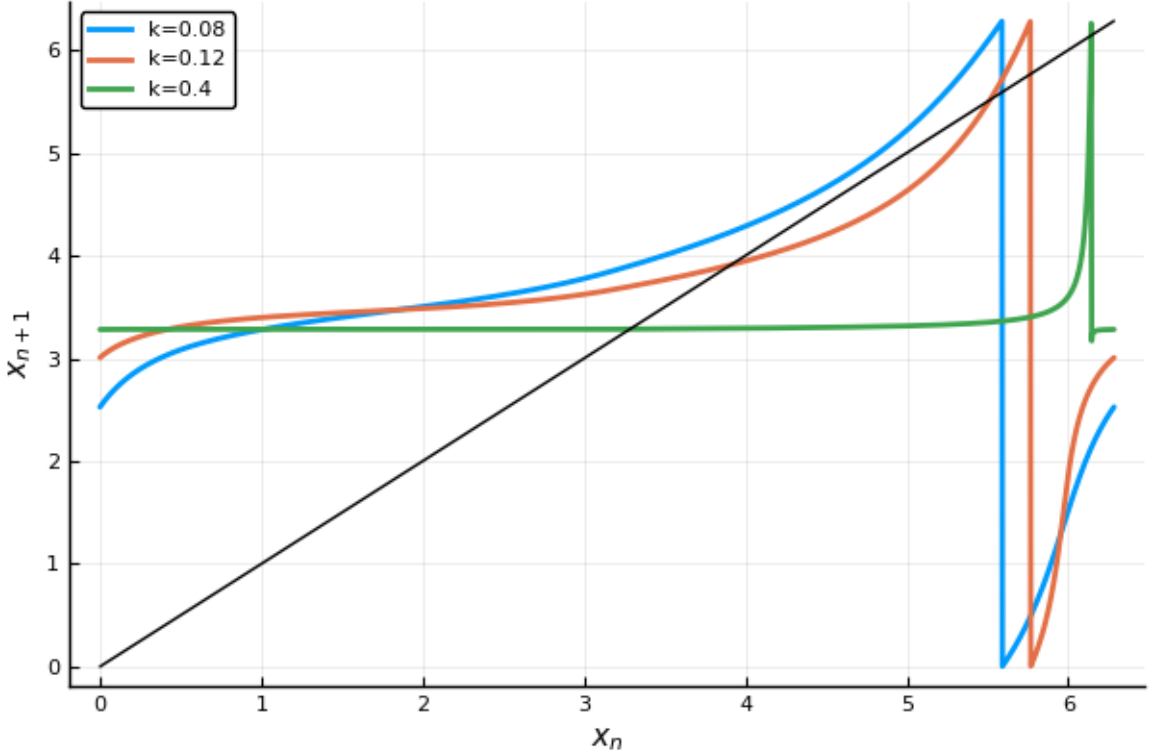


Figure 3.1 The 1-D entrainment map with different k values.

3.1.4 Conditions of entrainment

Whether an entrained solution exists or not depends on parameters. In Figure 3.2, the upper panel shows a case of non-entrainment, while the lower panel shows entrainment. In both panels, oscillator 1 (red curve) is entrained to the LD oscillator (blue curve) as the coupling constant k is sufficiently large. In the upper panel, the coupling from oscillator 1 to 2, α_1 is too small, while in the lower panel it is strong enough to yield entrainment. Here for clarity, we have allowed θ_2 to oscillate between π and 3π , while restricting the other two oscillators to the range $[0, 2\pi]$. This simulation suggests, not surprisingly, that there exist a range of parameters over which entrained solutions exist.

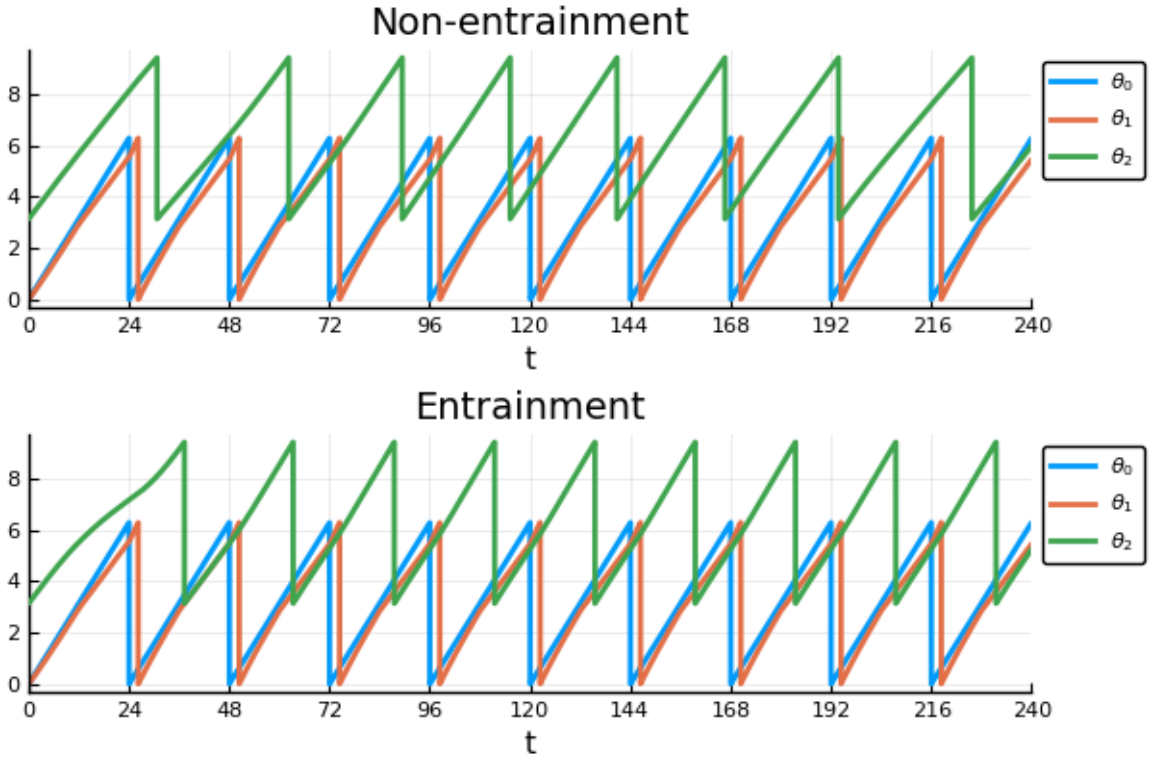


Figure 3.2 The time course of the original system: we start the simulation with initial value $(0,0,\pi)$. Whenever θ_2 hits 3π , we turn it back to π .

Finding an entrained solution of (3.1) is equivalent to finding a fixed points of the entrainment map. From the first equation of (3.2), we need $x' = x$, which implies $\rho(x, y, z) = 24$. From the second equation of (3.2) similarly, we need

$$24\omega_1 + k \int_0^{24} f(\theta_0) \sin(\theta_0 - \theta_1) dt = 2\pi. \quad (3.3)$$

Thus, we obtain the following formula for k .

$$k = \frac{2\pi - 24\omega_1}{\int_0^{24} f(\theta_0) \sin(\theta_0 - \theta_1) dt} \quad (3.4)$$

Since

$$\int_0^{24} |f(\theta_0) \sin(\theta_0 - \theta_1)| dt \leq \int_0^{24} |f(\theta_0)| dt = 12, \quad (3.5)$$

the following bound for k is obtained

$$k \geq 2|\omega - \omega_1|. \quad (3.6)$$

In other words k must be sufficiently larger than the difference between the intrinsic frequencies of the LD and first oscillator.

To obtain a bound for α_1 , note that based on the definition of Poincare section, ρ also satisfies $\theta_2(\rho) = 3\pi$. Integrating the equation for θ_2 from 0 to ρ , we obtain:

$$\begin{aligned} \theta_2(\rho) - \theta_2(0) &= \int_0^\rho [\omega_2 + \alpha_1 \sin(\theta_1 - \theta_2)] ds \\ 2\pi &= \omega_2 \rho + \alpha_1 \int_0^\rho \sin(\theta_1 - \theta_2) ds. \end{aligned} \quad (3.7)$$

Since $\rho(\theta_0, \theta_1) = 24$ is one of the necessary conditions for the system to have an entrained solution, we substitute $\rho = 24$ into (3.7).

$$\alpha_1 = \frac{2\pi - 24\omega_2}{\int_0^{24} \sin(\theta_1(s) - \theta_2(s)) ds} \quad (3.8)$$

Since $|\sin(x)| \leq 1$, we obtain a necessary condition for entrainment.

$$\alpha_1 \geq \frac{|2\pi - 24\omega_2|}{24} = |\omega - \omega_2| \quad (3.9)$$

Note that this bound does not specifically include the term ω_1 . This occurs because the necessary condition for entrainment is that oscillator 1 is already entrained and thus oscillates with a 24-hour period. Thus, it is enough to compare the intrinsic frequency ω_2 to ω that of the LD drive and ensure that coupling strength α_1 from oscillator 1 is sufficiently large.

3.1.5 Existence of fixed points

Knowing the necessary conditions for entrainment allows us to now turn to finding fixed points of the entrainment map. For the map to have fixed points, from equation (3.2) it follows that

$$\begin{aligned} F_1(x, y, k, \alpha_1) - x &= 0 \\ F_2(x, y, k, \alpha_1) - y &= 0. \end{aligned} \tag{3.10}$$

From the first of these two equations, $\rho(x, y, k, \alpha_1) = 24$. Substituting into equation (3.7), and simplifying yields,

$$\int_0^{24} \sin(\theta_1(s) - \theta_2(s)) ds = \frac{2\pi - 24\omega_2}{\alpha_1}. \tag{3.11}$$

From the Mean Value Theorem for integrals, there exists a $s_1 \in [0, 24]$, such that

$$\sin(\theta_1(s_1) - \theta_2(s_1)) = \frac{2\pi - 24\omega_2}{24\alpha_1} = \frac{\omega - \omega_2}{\alpha_1}. \tag{3.12}$$

Now we simplify the second equation of (3.10). Rearranging equation (3.4), we obtain

$$\int_0^{24} f(\theta_0(s)) \sin(\theta_0(s) - \theta_1(s)) ds = \frac{2\pi - 24\omega_1}{k}. \tag{3.13}$$

Notice that, $\theta_0(s) = x + ws$, so we apply a change of variable $u = x + ws$, to obtain

$$\int_x^{x+2\pi} f(u) \sin(\hat{\theta}_0(u) - \hat{\theta}_1(u)) du = \omega \frac{2\pi - 24\omega_1}{k}. \quad (3.14)$$

If $x > \pi$, then the integral is only nonzero during the interval $[2\pi, 3\pi]$,

$$\begin{aligned} \int_{2\pi}^{3\pi} \sin(\hat{\theta}_0(u) - \hat{\theta}_1(u)) du &= \omega \frac{2\pi - 24\omega_1}{k} \\ \sin(\theta_0(s_2) - \theta_1(s_2)) &= \frac{2(\omega - \omega_1)}{k}. \end{aligned} \quad (3.15)$$

If $x < \pi$, the integral has two nonzero parts.

$$\left(\int_x^\pi + \int_{2\pi}^{x+2\pi} \right) \sin(\hat{\theta}_0(u) - \hat{\theta}_1(u)) du = \omega \frac{2\pi - 24\omega_1}{k} \quad (3.16)$$

Using the periodicity of sine function, we can shift the second integral by 2π ,

$$\begin{aligned} \left(\int_x^\pi + \int_0^x \right) \sin(\hat{\theta}_0(u) - \hat{\theta}_1(u)) du &= \omega \frac{2\pi - 24\omega_1}{k} \\ \int_0^\pi \sin(\hat{\theta}_0(u) - \hat{\theta}_1(u)) du &= \omega \frac{2\pi - 24\omega_1}{k} \\ \sin(\theta_0(s_2) - \theta_1(s_2)) &= \frac{2(\omega - \omega_1)}{k}, \end{aligned} \quad (3.17)$$

where the last equality again uses the Mean Value Theorem. Hence, the condition for the existence of fixed points reduces to

$$\begin{aligned} \sin(\theta_1(s_1) - \theta_2(s_1)) &= \frac{\omega - \omega_2}{\alpha_1} \\ \sin(\theta_0(s_2) - \theta_1(s_2)) &= \frac{2(\omega - \omega_1)}{k}. \end{aligned} \quad (3.18)$$

Notice that the absolute value of left hand side of both of equations is bounded by one which immediately allows us to recover the necessary conditions on parameters for entrainment, (3.6) and (3.9). We will use the above equations to show that the number of fixed points of the map are bounded between 0 and 4, depending on the values of the parameters k and α_1 . To find fixed points however, both of the equations must be solved simultaneously. In particular, there must be values of s_1 and s_2 such that $\theta_1(s_1) = \theta_1(s_2)$. We will show this later when we define and analyze the nullclines of the map.

To obtain the bounds on the number of fixed points, define

$$\begin{aligned} k_c &= 2(\omega - \omega_1) \\ \alpha_c &= \omega - \omega_2. \end{aligned} \tag{3.19}$$

These are the critical values of k and α_1 . When $k < k_c$, θ_1 can not be entrained by the light forcing; when $\alpha_1 < \alpha_c$, θ_2 can not be entrained by θ_1 . Thus, a necessary condition for entrainment is that both $k \geq k_c$ and $\alpha_1 \geq \alpha_c$.

In the following, we will provide numerical experiments that show that these conditions are also sufficient for entrainment, but that the nature of entrainment depends on the choice of the parameter pair (k, α_1) . Specifically, there exist four curves in the parameter space that separate regions where there are four, two or one fixed point (Figure 3.3a). Two of these curves are the lines $k = k_c$ and $\alpha = \alpha_c$. The other two curves are described below in Case I.

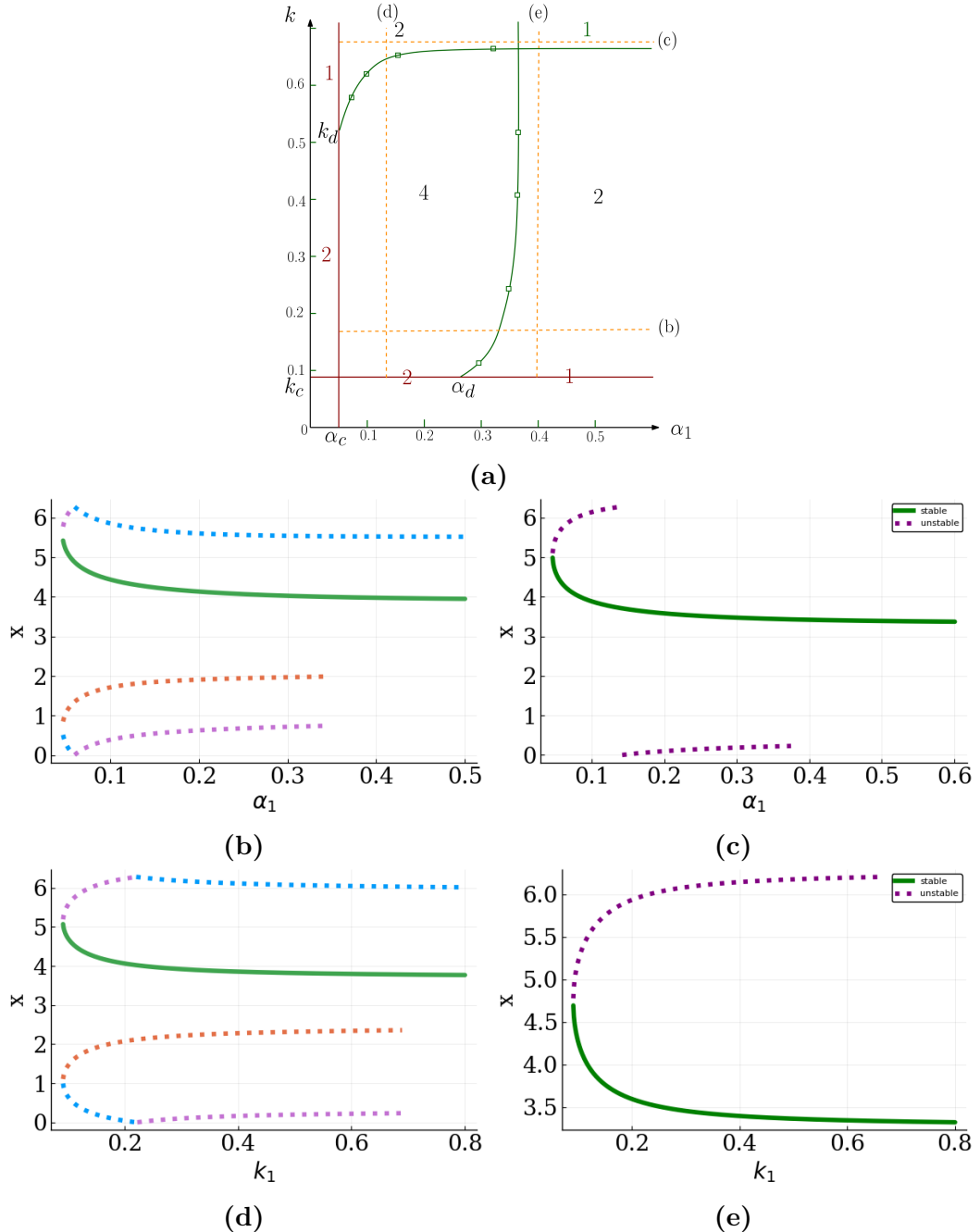


Figure 3.3 (a) The (α_1, k) parameter space showing how the number of fixed points depends on these parameters. There is no fixed points if either parameter lies below the critical value α_c or k_c . The number of fixed points in other regions are labeled. Squares along the green curves represent actual parameter pairs that were tested during the simulation. The rest of these curves were extrapolated. The dashed lines denote the parameter value we take for the one-dimensional bifurcation curves shown in panel (b-e). (b) We fixed $k = 0.12$, by increasing α_1 , the fixed points along the green curve stay stable, while the fixed points along the other three curves are unstable. (c) $k = 0.35$. (d) $\alpha_1 = 0.1$. (e) $\alpha_1 = 0.4$.

Case I: There exist curves $k_{ub}(\alpha_1)$ and $\alpha_{ub}(k)$ that together with the lines $k = k_c$ and $\alpha_1 = \alpha_c$ bound a region R in parameter space such that for any parameter pair chosen in the interior of R , the two-dimensional map has four fixed points. The subscript ub denotes the upper bound.

Case II: If $\alpha_1 < \alpha_{ub}(k)$ and $k > k_{ub}(\alpha)$, or if $\alpha_1 > \alpha_{ub}(k)$ and $k < k_{ub}(\alpha)$ then for any parameter pair chosen in either of those regions, the map possesses two fixed points.

Case III: Define $\alpha_d = \alpha_{ub}(k_c)$ and $k_d = k_{ub}(\alpha_c)$. If $k = k_c$, for $\alpha_c < \alpha_1 < \alpha_d$ there are two fixed points and for $\alpha_1 > \alpha_d$ there is one fixed point. Similarly, if $\alpha_1 = \alpha_c$, for $k_c < k < k_d$, there are two fixed points and for $k > k_d$, there is one fixed point.

Case IV: If $k > k_{ub}(\alpha)$ and $\alpha_1 > \alpha_{ub}(k)$, then the map possesses exactly one fixed point.

Let us first show that the number of fixed points is bounded above by four. From the first equation of (3.18), $0 < \sin(\theta_1(s_1) - \theta_2(s_1)) < 1$ when $\alpha_c < \alpha_1 < \alpha_{ub}$. Because of the periodicity of the sine function, there exists two possible angles $\beta_i(s_1)$, $i = 1, 2$, such that

$$\theta_1(s_1) - \theta_2(s_1) = \beta_i(s_1). \quad (3.20)$$

On the periodic orbit, the phase difference is also periodic, which means that by flowing backward s_1 amount of time, the phase difference goes to a specific value

$$\theta_1(0) - \theta_2(0) = \beta_i(0). \quad (3.21)$$

Since $\theta_2(0) = \pi$,

$$y_0 = \theta_1(0) = \beta_i(0) + \pi. \quad (3.22)$$

Hence there are two possible initial conditions for y_0 that satisfy the above. For second equation of (3.18), we have:

$$\theta_0(s_2) - \theta_1(s_2) = \zeta_j(s_2), j = 1, 2. \quad (3.23)$$

Going backward s_2 amount of time, we have

$$\theta_0(0) - \theta_1(0) = \zeta_j(0). \quad (3.24)$$

Combining with (3.22), we have

$$x_0 = \theta_0(0) = \zeta_j(0) + \theta_1(0) = \zeta_j(0) + \beta_i(0) + \pi. \quad (3.25)$$

Hence, the total number of fixed point is at most four.

Geometrically there is a nice interpretation of this result. The left-hand sides of (3.18) are both periodic sine functions. The right-hand sides are just horizontal lines. Thus, these lines each intersect the sine functions at two points. By choosing one intersection point from each of these graphs, we obtain four possible fixed points, subject to whether the condition $\theta_1(s_1) = \theta_1(s_2)$ holds. We can also see why fixed points arise at small values of k or α_1 due to saddle-node bifurcations. For example, when k is decreased towards k_c , the horizontal line defining the right-hand side of the first equation in (3.18) increases towards the value 1. Thus, this equation can have at most one solution before those disappear with a further decrease in k . The signature of a saddle node-bifurcation is shown in Figure 3.3(b)-(e). where solid (dashed) curves denote stable (unstable) fixed points.

To understand why there is a change in a number of fixed points for large values of either of the parameters, consider Case II when α_1 is sufficiently large so that we can consider the singular limit. Make a change of time variable $\tau = \alpha_1 t$, then τ can be considered as a fast time variable. Equation (3.1) becomes:

$$\begin{aligned}\frac{d\theta_0}{d\tau} &= \frac{\omega}{\alpha_1} \\ \frac{d\theta_1}{d\tau} &= \frac{\omega_1}{\alpha_1} + \frac{k}{\alpha_1} f(\theta_0) \sin(\theta_0 - \theta_1) \\ \frac{d\theta_2}{d\tau} &= \frac{\omega_2}{\alpha_1} + \sin(\theta_1 - \theta_2)\end{aligned}\tag{3.26}$$

When $\alpha_1 \gg 0$, we obtain the fast equations

$$\begin{aligned}\frac{d\theta_0}{d\tau} &= 0 \\ \frac{d\theta_1}{d\tau} &= 0 \\ \frac{d\theta_2}{d\tau} &= \sin(\theta_1 - \theta_2)\end{aligned}\tag{3.27}$$

On the fast time scale, neither θ_0 or θ_1 evolve, but θ_2 is free to evolve to the initial value of θ_1 . This is exactly the initial value $y = \theta_1(0)$ of the map. Hence, the system is reduced to study

$$\frac{d\theta_2}{d\tau} = \sin(y - \theta_2).\tag{3.28}$$

The reduced system for this flow has two fixed points, $\theta_2 = y$, or $\theta_2 = y + \pi$, where $\theta_2 = y$ is stable, and the other is unstable. What this means is that on the fast time scale, θ_2 becomes equal to $y = \theta_1(0)$. This makes sense since if the coupling from oscillator 1 to oscillator 2 is sufficiently strong, these two oscillators should synchronize. By returning to the original time scale and now letting $\epsilon = 1/\alpha_1$, we

obtain

$$\begin{aligned}\frac{d\theta_0}{dt} &= \omega \\ \frac{d\theta_1}{dt} &= \omega_1 + kf(\theta_0) \sin(\theta_0 - \theta_1) \\ \epsilon \frac{d\theta_2}{dt} &= \epsilon\omega_2 + \sin(\theta_1 - \theta_2),\end{aligned}\tag{3.29}$$

which when $\epsilon \rightarrow 0$ yields

$$\begin{aligned}\frac{d\theta_0}{dt} &= \omega \\ \frac{d\theta_1}{dt} &= \omega_1 + kf(\theta_0) \sin(\theta_0 - \theta_1) \\ 0 &= \sin(\theta_1 - \theta_2).\end{aligned}\tag{3.30}$$

Thus, on the original time scale, $\theta_1 = \theta_2$ remains. Thus, when θ_2 returns to the Poincaré section again, $\theta_1 = \pi$ and therefore $y = \pi$.

Remark The singular perturbation results show that the number of fixed points changes as $\alpha_1 \rightarrow \infty$. Our numerical results in Figure 3.3 indicate that the changes may occur at large finite values of the parameters.

3.1.6 Geometrical methods for finding fixed points and manifolds

Fixed points of the map can be found by geometrically solving equation (3.10). Namely, in Figure 3.4(a, b), we show contour plots of the functions $F_1(x, y, k, \alpha_1) - x$ and $F_2(x, y, k, \alpha_1) - y$. The zero level curves of each constitute the x - and y -nullclines of (3.10) and are plotted on common $x - y$ plane; Fig 3.4(c). The blue (red) curve corresponds to the x -(y)-nullcline. The four intersection points are fixed points of the map. The contour plots and nullclines also reveal more information that will be useful for understanding the dynamics of the map. The region between the two blue curves where the level curves have a positive value corresponds to values for which the

return time of θ_2 to the Poincare section \mathcal{P} is less than 24 hours. The complementary region therefore corresponds to values for which the return is greater than 24 hours. In Figure 3.4(d), we show the return time map $\rho(x, y)$ which allows us to also easily visualize its gradient, which will be important for the stability analysis.

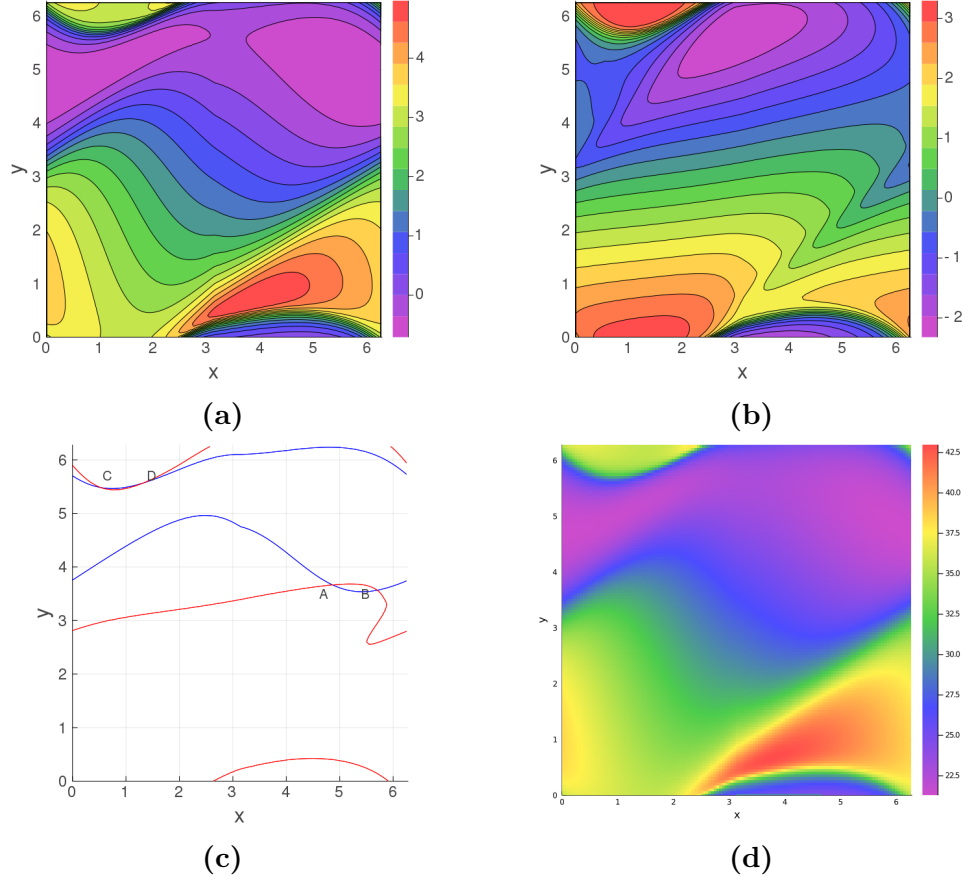


Figure 3.4 (a) and (b): Contour plots of the map $F_1 - x$ and $F_2 - y$. (c) Nullclines of the 2-D map which correspond to the zero level curves of the contour plots (blue for (a) and red for (b)). Points of intersection are fixed points of the map. (d) Return time map $\rho(x, y)$. Note the similarities with panel (a). The parameter set is $k = 0.1, \alpha = 0.08$.

In Figure 3.5, we show the nullclines for several different choices of parameters that indicate how the number of fixed points can vary. Panel (a) shows a case where the x and y -nullclines intersect tangentially at two different points. These points of tangency correspond to the existence of a saddle-node bifurcation that exists at $k = k_c$. Increasing k leads to a region in parameter space of four fixed points as indicated

in panel (c) from Figure 3.5. Further increasing k leads to another bifurcation (Figure 3.5(b)) for which there are only two fixed points. In this case, a portion of the two curves of x -nullcline (upper left hand parts) merge and disappear. This does not appear to be a saddle-node bifurcation of fixed points which causes two of the fixed points to disappear. In fact, it may be the case that the numerical methods that we are using are not sufficiently accurate and are incapable of resolving the issue. Panel (c) shows the case of large α_1 where again only two fixed points exist. Note here that a portion of the y -nullcline is nearly horizontal at $y = \pi$. The x -nullcline is now a single curve as the upper portion from Figure 3.4(c) is destroyed by a discontinuity in the return time map (not shown). Panel (d) shows the case for which both α_1 and k are sufficiently large. Note here that the x -nullcline is vertical at $x = \pi$, and the y -nullcline is horizontal at $y = \pi$. The reason for this is relatively easy to explain. When the coupling strength from the oscillator one to oscillator two is large enough, then these two oscillators quickly synchronize. Similarly the large LD coupling to oscillator one quickly synchronizes that pair. Thus, all three oscillators quickly synchronize and since the Poincare map measures their relative values when $\theta_2 = \pi$, the x and y variables will also equal π . The figure does not reveal that the return time map for the time it takes oscillator 1 to return to \mathcal{P} possesses several curves of discontinuity.

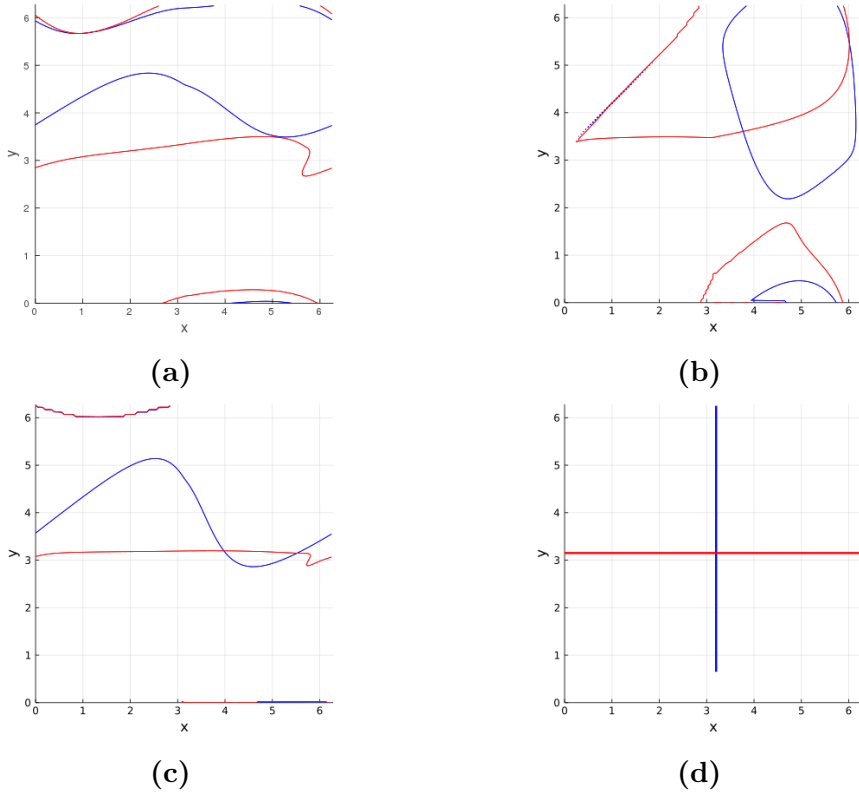


Figure 3.5 Nuclines of the 3-oscillator model for different coupling strengths: (a) $k = k_c$, $\alpha_1 = 0.1$. (b) Large k : $k = 2$, $\alpha_1 = 0.1$. (c) Large α_1 : $\alpha_1 = 2$, $k = 0.12$. (d) Both large: $\alpha_1 = 2$, $k = 2$.

Visualization of manifolds and entrainment times. An application of the Lagrangian descriptor method is now presented for the coupled Kuramoto model. In Figure 3.6(a), the gradient of the Lagrangian descriptor $M(y, N)$ is plotted in a heatmap, where $N = 5$ and the 2-norm is used. The curves in different colors represent the discontinuity of $M(y, N)$. By the definition of the Lagrangian descriptor, those curves are the invariant manifolds of the fixed points of the map. In Figure 3.6(b), the original values of $M(y, N)$ are presented as a contour plot. In Figure 3.6(c), an entrainment time is plotted as a heatmap, which reflects the stable manifolds of the saddle points B and C. It is also consistent with the result obtained by Lagrangian descriptor. Note that they both show the existence of various stable manifolds of the

fixed points A, B and C. The Lagrangian descriptor method also reveals the unstable manifolds of points B, C and D.

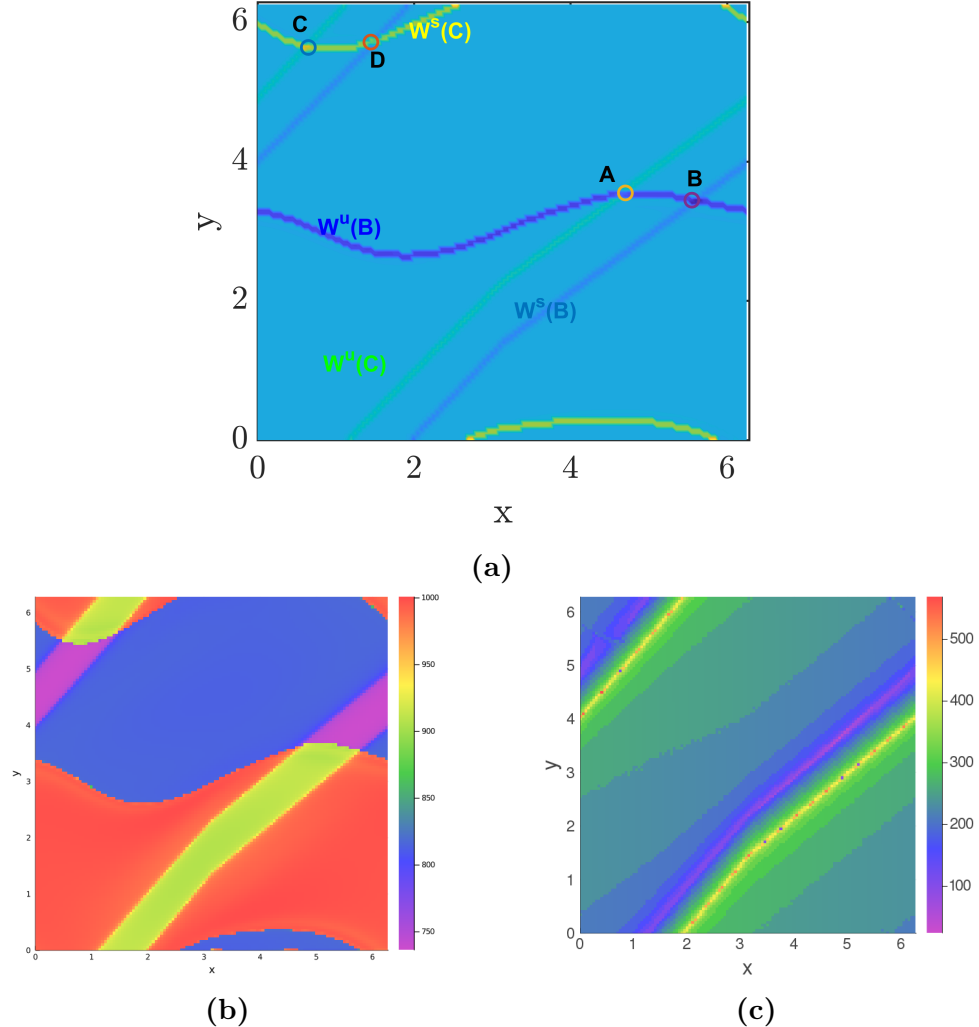


Figure 3.6 (a) Manifolds visualization with Lagrangian descriptor. (b) The contour plot of the Lagrangian descriptor $M(y, N)$. (c) Entrainment time plot.

3.1.7 Attempt for leading order approximation

Since our map (3.2) is written implicitly, we will approximate the flow of $\theta_1(t)$ as a first order power series, then write down the map explicitly in terms of initial condition of x, y and return time $\rho(x, y)$. Because of the discontinuity of $f(\theta_0)$, the flow of θ_1 is a combination of two flows in light and darkness conditions.

In darkness, the solution only depend on initial θ_1 value y and t :

$$\theta_1^D(y, t) = y + \omega_1 t \quad (3.31)$$

In light, we solved it as a power series of order 1:

$$\theta_1^L(x, y, t) = y + (\omega_1 + k_1 \sin(x - y))t \quad (3.32)$$

Evaluate $\theta_1(\rho)$

Once we get that, we get an approximation of Π_2 .

Case I: $x > \pi$

θ_1 will evolve on θ_1^D for $\frac{2\pi-x}{\omega}$ hours, then evolve on θ_1^L for 12 hours, then back to θ_1^D for $\rho - \frac{2\pi-x}{\omega} - 12$ hours, hence

$$\begin{aligned} \theta_1(x, y, \rho) &= \theta_1^D(y, \frac{2\pi-x}{\omega}) + \theta_1^L(2\pi, \theta_1^D(y, \frac{2\pi-x}{\omega}), 12) \\ &\quad + \theta_1^D(\theta_1^L(2\pi, \theta_1^D(y, \frac{2\pi-x}{\omega}), 12), \rho - \frac{2\pi-x}{\omega} - 12) \\ &= \omega\rho(x, y) + 24k_1 \sin(x - y) - 2x + 3y - 12\omega \\ &\quad + 24\omega_1 + 4\pi \end{aligned} \quad (3.33)$$

Then we obtain the Jacobian matrix for case I:

$$\begin{pmatrix} \omega\rho_x + 1 & \omega\rho_y \\ \omega(\rho_x + \frac{1}{\omega}) + C & \omega\rho_y - C \end{pmatrix} \quad (3.34)$$

Where $C = 24k_1 \cos(x - y) - 3$. The eigenvalues are:

$$\begin{aligned}\lambda_1 &= 3 - 24k_1 \cos(x - y) \\ \lambda_2 &= 1 + \omega\rho_y + \omega\rho_x\end{aligned}\tag{3.35}$$

Now the stability of fixed points in case I can be determined by just analyzing these equations.

Case II: $x < \pi$

θ_1 will evolve on θ_1^L for $\frac{\pi-x}{\omega}$ hours, then evolve on θ_1^D for 12 hours, then back to θ_1^L for $\rho - \frac{\pi-x}{\omega} - 12$ hours, hence

$$\begin{aligned}\theta_1(x, y, \rho) &= \theta_1^L(x, y, \frac{\pi-x}{\omega}) + \theta_1^D(\theta_1^L(x, y, \frac{\pi-x}{\omega}), 12) \\ &\quad + \theta_1^L(2\pi, \theta_1^D(\theta_1^L(x, y, \frac{\pi-x}{\omega}), 12), \rho - \frac{\pi-x}{\omega} - 12) \\ &= 24\omega + 3\mathcal{F} + [\omega_1 - k_1 \sin(12\omega + \mathcal{F})](\rho(x, y) - 12 \\ &\quad - \frac{\pi-x}{\omega}) \\ &= 24\omega + 3\mathcal{F} + (\omega_1 + k_1 \sin \mathcal{F})(\rho(x, y) + \frac{x}{\omega} - 24) \\ &= \frac{\omega_1}{\omega}x + \omega_1\rho(x, y) + 3\mathcal{F} + k_1 \sin \mathcal{F}(\rho(x, y) + \frac{x}{\omega} - 24) \\ &\quad + 24(\omega - \omega_1)\end{aligned}$$

Where

$$\begin{aligned}\mathcal{F} &= y + \frac{(\pi-x)\omega_1}{\omega} + \frac{k_1(\pi-x) \sin(x-y)}{\omega} \\ &= y - \frac{\omega_1}{\omega}x - \frac{k_1}{\omega}x \sin(x-y) + 12(\omega_1 + k_1)\end{aligned}$$

Then we compute the Jacobian matrix:

$$\begin{pmatrix} \omega\rho_x + 1 & \omega\rho_y \\ A\mathcal{F}_x + B\rho_x + B/\omega & A\mathcal{F}_y + B\rho_y \end{pmatrix} \quad (3.36)$$

Where

$$\begin{aligned} \mathcal{F}_x &= -\frac{1}{w}(w_1 + k_1 \sin(x-y) + x \cos(x-y)) \\ \mathcal{F}_y &= 1 + \frac{k_1}{w}x \cos(x-y) \\ A &= 3 + \frac{k_1}{w}x \cos \mathcal{F} \\ B &= w_1 + k_1 \sin \mathcal{F} \end{aligned}$$

The eigenvalues are:

$$\lambda = \frac{1 + \omega\rho_x + A\mathcal{F}_y + B\rho_y}{2} \pm \frac{\sqrt{\Delta}}{2} \quad (3.37)$$

Where

$$\begin{aligned} \Delta &= ((A\mathcal{F}_y + B\rho_y + \omega\rho_x + 1)^2 \\ &\quad - 4A(-\mathcal{F}_x\omega\rho_y + \mathcal{F}_y\omega\rho_x + \mathcal{F}_y)) \end{aligned}$$

Combined with the our numerical result, the leading order approximation shows that the derivative of $\rho(x, y)$ plays an important role in determining the stability.

3.1.8 Stability of fixed points: Numerical versus analytic results

With the leading order approximation obtained above, we will first describe the stability result that we obtained numerically. We use Figure 3.3(b) as an example.

Suppose we take $\alpha_1 = 0.1$, the fixed point on the blue curve ($x = 5.85, y = 3.42$) is a saddle. We find $\lambda_1 = 0.12 < 1, \lambda_2 = 2.51 > 1$. As we increase α_1 , and numerically calculate the Jacobian directly, we found that λ_2 doesn't change too much, and it's always greater than 1. But $\lambda_1 \rightarrow 0$. We substitute the values of parameters and fixed points into the second equation of (3.35),

$$\begin{aligned} \lambda_2 &= 3 - 2.88 \cdot \cos(x - y) \\ &\quad 3 < \lambda_2 < 5.88. \end{aligned} \tag{3.38}$$

This indicates that λ_2 is greater than 1 and doesn't change too much. For λ_1 , our numerical results show that the eigenvalue goes to zero as α_1 increases. From the first order approximation, we also numerically verified that $\rho_x + \rho_y \mapsto \frac{-1}{\omega}$ from the second equation of (3.35).

For the curve green, the fixed point ($x = 4.43, y = 3.57$) is stable, $\lambda_1 = 0.119 < 1, \lambda_2 = 0.398 < 1$, as α_1 increases, λ_1 approaches zero while λ_2 doesn't change much. A similar argument using (3.35) using the first order approximation with $\cos(x - y) > 0$, shows $\lambda_2 < 1$. The fixed points on the purple and red curves can be explained by equation (3.37). The derivative of the return time ρ can be very large when we increase α_1 , which, in turn, causes large eigenvalues. For the red curve, the fixed point is unstable, $\lambda_1 > 1, \lambda_2 > 1$. As α_1 increases, both eigenvalues diverge to a large number (numerically $\lambda_1 > 100, \lambda_2 > 6000$, when $\alpha_1 = 0.35$), making this fixed point extremely unstable. For the purple curve, the fixed point is also unstable, $\lambda_1 < 1, \lambda_2 > 1$. As α_1 increases, one eigenvalue diverges to a large number (numerically $\lambda_2 > 6000$, and $\lambda_1 < -5$ when $\alpha_1 = 0.35$), making this fixed point extremely unstable as well.

While these numerical results, coupled with the first order approximation are suggestive of the change in number of fixed points from four to two across the green bifurcation curves shown in Figure 3.3(a), they don't prove that those curves actually exist. Indeed the singular perturbation argument shown earlier as $\alpha_1 \rightarrow \infty$ only guarantees that in that limit, two fixed points exist. It could be that our numerical methods are not fully resolved, or are not resolvable. Perhaps the large eigenvalues obtained at the linearization are indicative of the difficulty in ascertaining whether these fixed points actually exist since numerically, at least, iterates diverge quickly from a vicinity of the proposed fixed points. Thus, we acknowledge here that there is still a discrepancy with the numerical results that we have presented and that which we can actually prove.

3.1.9 Generalization to $N + 1$ oscillators

We now briefly return to study the full hierarchical system consisting of $N + 1$ oscillators (Equation (3.1)). From our study of the three-oscillator problem above and given that the coupling between the i^{th} and $i^{th} + 1$ oscillators for any $i \geq 1$ is symmetric, we conjecture that the addition of each new oscillator to the hierarchical chain introduces two new fixed points. Thus, in the $N + 1$ dimensional system, there are 2^N fixed points. Of these, only one is stable, while the remaining fixed points are all unstable. Of those, one of them has eigenvalues that are all larger than one in absolute value. The remaining unstable fixed points all possess both stable and unstable directions (i.e., higher dimensional saddle points).

Regarding the direction of and time to entrainment, it is too difficult to fully categorize each of the possibilities. Instead we note that based on our three-oscillator results, we conjecture that the fastest path to entrainment is when oscillators in the chain get progressively entrained. By this we mean that oscillator 1 is first entrained (or becomes close to entrained) by the LD forcing. This is followed by

oscillator 2 becoming nearly entrained and so on. The direction of entrainment is extremely difficult to give general conditions for since this depends critically on the initial position of each oscillator. Our results from the three-oscillator case suggest that the stable and unstable manifolds of the unstable fixed points will divide the phase space into regions where oscillators converge in different directions.

3.2 Application to Higher Dimensional Models

3.2.1 The Novak-Tyson model

In this section, we introduce the Novak-Tyson(NT) model [54]. It is a model for the molecular circadian clock in the fruit fly Drosophila. Mathematically, it can be written in the following form:

$$\begin{aligned} \frac{1}{\phi} \frac{dP}{dt} &= F_1(P, M) + G(P, t) = M - k_f h(P) - k_D P - k_L f(t) P \\ \frac{1}{\phi} \frac{dM}{dt} &= \epsilon F_2(P, M) = \epsilon(g(P) - M), \end{aligned} \tag{3.39}$$

where $g(P) = \frac{1}{1+P^4}$, and $h(P) = \frac{P}{0.1+P+2P^2}$ are nonlinear functions. The M variable represents mRNA concentration, and P variable represents the protein concentration. The parameter ϵ is small, which separates P and M into fast and slow variables. The parameter ϕ will directly affect the period of the solutions of this system. The function $f(t)$ describes the LD forcing, which is defined by a periodic step function: $f(t) = 1, \forall t \in (0, 12]$, which denotes the complete light condition; $f(t) = 0, \forall t \in (12, 24]$, which denotes the complete darkness condition. Mathematically, it can be written as $f(t) = \mathcal{H}(\sin(\frac{\pi}{12}t))$. In Drosophila, there is protein degradation during darkness, and the light will increase the degradation. So k_D represents the degradation rate during darkness, and k_L represents the degradation

rate which is caused by light. The parameter k_f is a combination of two variables from the original model in their paper [54].

Let's consider the unforced system first, which is also equivalent as the complete darkness case. Let $k_L = 0$, we have

$$\begin{aligned} \frac{1}{\phi} \frac{dP}{dt} &= M - k_f h(P) - k_D P \\ \frac{1}{\phi} \frac{dM}{dt} &= \epsilon(g(P) - M). \end{aligned} \quad (3.40)$$

Under our choice of parameters, the system has a fixed point at $(P, M) = (1.167556, 0.349082)$ calculated by Newton's method. The Jacobian of the unforced system is calculated as below:

$$D_{(P,M)} F = \phi \begin{pmatrix} -k_D + k_f \frac{2P^2 - 0.1}{(2P^2 + P + 0.1)^2} & 1 \\ -\frac{4\epsilon P^3}{(P^4 + 1)^2} & -\epsilon \end{pmatrix} = 2.1 \begin{pmatrix} -0.05 + \frac{2P^2 - 0.1}{(2P^2 + P + 0.1)^2} & 1 \\ -\frac{4\epsilon P^3}{(P^4 + 1)^2} & -0.05 \end{pmatrix} \quad (3.41)$$

Here the values of parameters are $k_f = 1, k_D = 0.05, \epsilon = 0.05, \phi = 2.1$. Evaluate the Jacobian at the fixed point, and calculate the eigenvalues, we found

$$DF|_{(1.167556, 0.349082)} = \begin{pmatrix} 0.24076 & 2.1 \\ -0.0818226 & -0.105 \end{pmatrix} \quad (3.42)$$

and $\lambda = 0.0678801 \pm 0.376749i$, so the fixed point is a spiral repellor. Furthermore, one can construct a region D , which is simply connected in \mathbb{R}^2 , and prove that there is a periodic orbit in D by Poincaré-Bendixson theorem.

Stability of the limit cycle We can use Floquet theory to study the stability of the unforced limit cycle. Suppose the limit cycle of system (3.40) is $\gamma(t)$, after a

change of variable $x = \gamma + y$, we have the variational equation:

$$\dot{y} = A(t)y, \quad (3.43)$$

where

$$A(t) = DF|_{\gamma(t)} = \phi \begin{pmatrix} -k_f h'(P) - k_D & 1 \\ \epsilon g'(P) & -\epsilon \end{pmatrix}_{\gamma(t)} \quad (3.44)$$

By Abel's theorem (Theorem 2.11 in [42]). The determinant of the monodromy matrix M , which is also the product of the Floquet multipliers, has the following,

$$\begin{aligned} \lambda_1 \lambda_2 &= \exp \left(\int_0^T \text{tr}(\mathbf{A}(s)) ds \right) \\ \lambda_2 &= \exp \left(\int_0^T \text{tr}(\mathbf{A}(s)) ds \right). \end{aligned} \quad (3.45)$$

Where one of the Floquet multipliers is $\lambda_1 = 1$. For the limit cycle to be stable, we must have $\lambda_2 < 1$, therefore we obtain the condition of stability.

$$\begin{aligned} \exp \left(\int_0^T \text{tr}(\mathbf{A}(s)) ds \right) &< 1 \\ \int_0^T (-k_f h'(P(s)) - k_D - \epsilon) ds &< 0 \\ (-k_D - \epsilon) T - k_f \int_0^T h'(P(s)) ds &< 0 \\ \int_0^T h'(P(s)) ds &> -\frac{(k_D + \epsilon)T}{k_f} \\ h'(P(s_c)) &> -\frac{k_D + \epsilon}{k_f}. \end{aligned} \quad (3.46)$$

This condition shows that the stability of the limit cycle depends on the slope of the nonlinear function $h(P)$.

The limit cycle solution With the classical parameter set $\phi = 2.1, k_D = 0.05, k_f = 1, \epsilon = 0.05$, we applied our continuation based shooting method, and found the limit cycling solution. The numerical results are presented below.

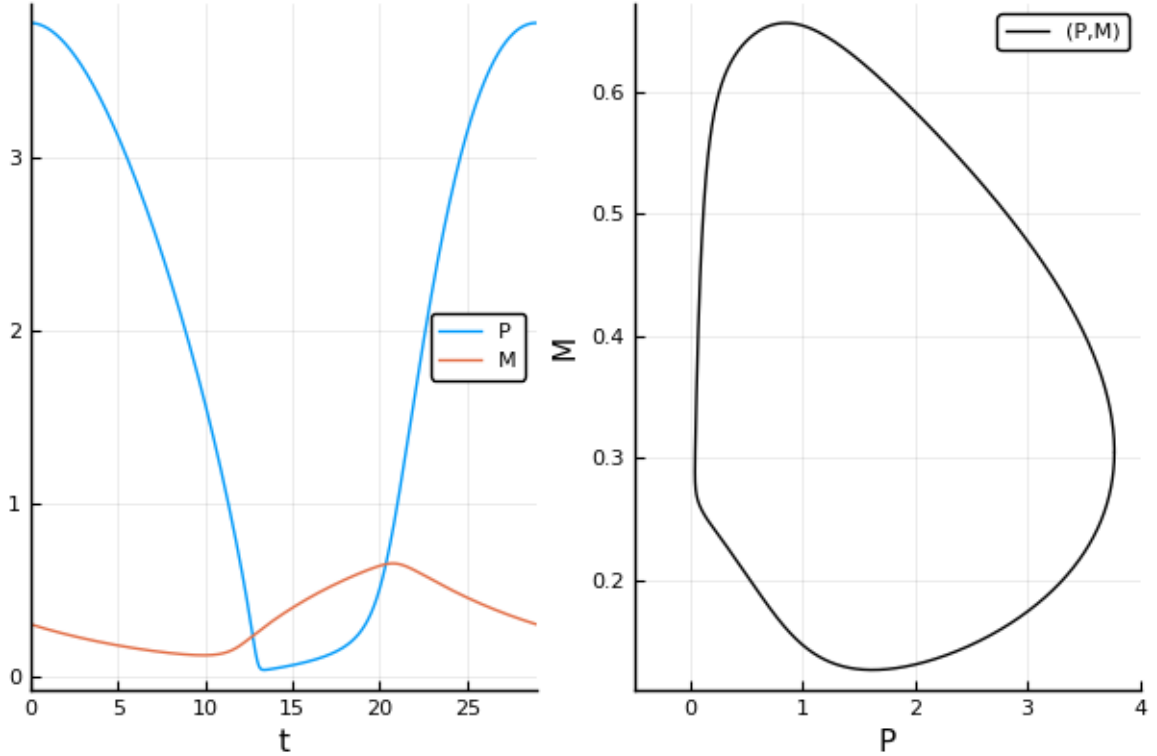


Figure 3.7 The left panel shows the time course of the solution in one period. The right panel shows the solution in the phase plane.

Phase reduction for the NT oscillator with a forcing Since the external forcing is small ($k_L = 0.05$), so we can apply phase reduction on it. Rewrite Equation (3.39) as a vectorized system:

$$\frac{d}{dt} \begin{pmatrix} P \\ M \end{pmatrix} = F(P, M) - k_L \begin{pmatrix} Pf(t) \\ 0 \end{pmatrix},$$

where $F(P, M) = \begin{pmatrix} M - k_D P - k_f \frac{P}{0.1+P+2P^2} \\ \epsilon \left(\frac{1}{1+P^4} - M \right) \end{pmatrix}$. Let $S = \omega t$, then the system is changed to be autonomous:

$$\begin{aligned} \frac{d}{dt} \begin{pmatrix} P \\ M \end{pmatrix} &= F(P, M) - k_L \begin{pmatrix} P\mathcal{H}(\sin(S)) \\ 0 \end{pmatrix} \\ \frac{dS}{dt} &= \omega \text{ mod } 24. \end{aligned} \quad (3.47)$$

Apply the phase reduction:

$$\begin{aligned} \frac{d\theta}{dt} &= \omega_0 - k_L \nabla \theta(\gamma_0(t)) \cdot \begin{pmatrix} P\mathcal{H}(\sin(S)) \\ 0 \end{pmatrix} \\ \frac{dS}{dt} &= \omega \text{ mod } 24, \end{aligned} \quad (3.48)$$

where $\gamma_0(t)$ is the unforced limit cycle, $\omega_0 = \frac{2\pi}{T_0}$ is the frequency of the NT oscillator, $\theta(\gamma_0(t))$ is the phase of $\gamma_0(t)$, $\omega = \frac{2\pi}{24}$ is the frequency of the light cycle.

Solve the adjoint equation to find $\nabla \theta(\gamma_0(t))$.

$$\begin{aligned} \frac{d\nabla_{\gamma_0(t)}\theta}{dt} &= -DF^T(\gamma_0(t))\nabla_{\gamma_0(t)}\theta \\ \nabla_{\gamma_0(0)}\theta \cdot F(\gamma_0(0)) &= \frac{2\pi}{T} \end{aligned} \quad (3.49)$$

Figure 3.8 shows the solution of the adjoint equation, which is also called the PRC (phase response curve).

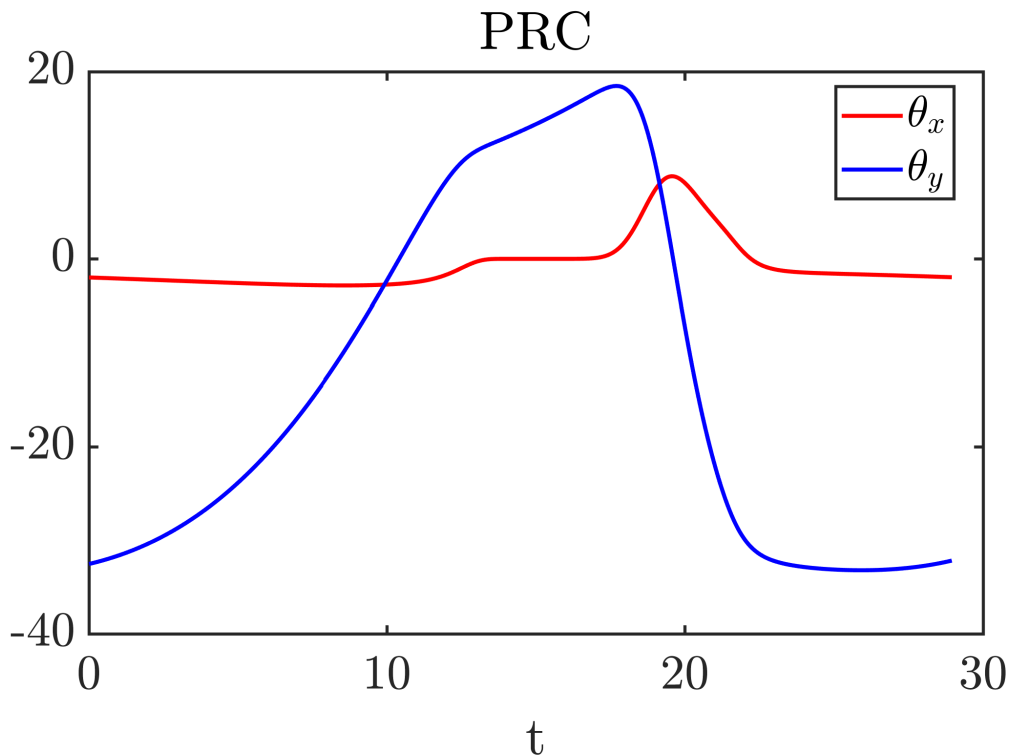


Figure 3.8 The red curve is $\nabla\theta$ in x direction, and the blue curve is $\nabla\theta$ in y direction.

The parameterization for the NT oscillator Here we applied the parameterization method introduced in chapter 2 on the unforced NT oscillator.

In Figure 3.9, we plot the limit cycle in black, the isochron curve at $\theta = 0$. We then take two points on the isochron, integrate them forward in one period of time, the two trajectories end at the same point on the limit cycle. Which is a good numerical test of our method.

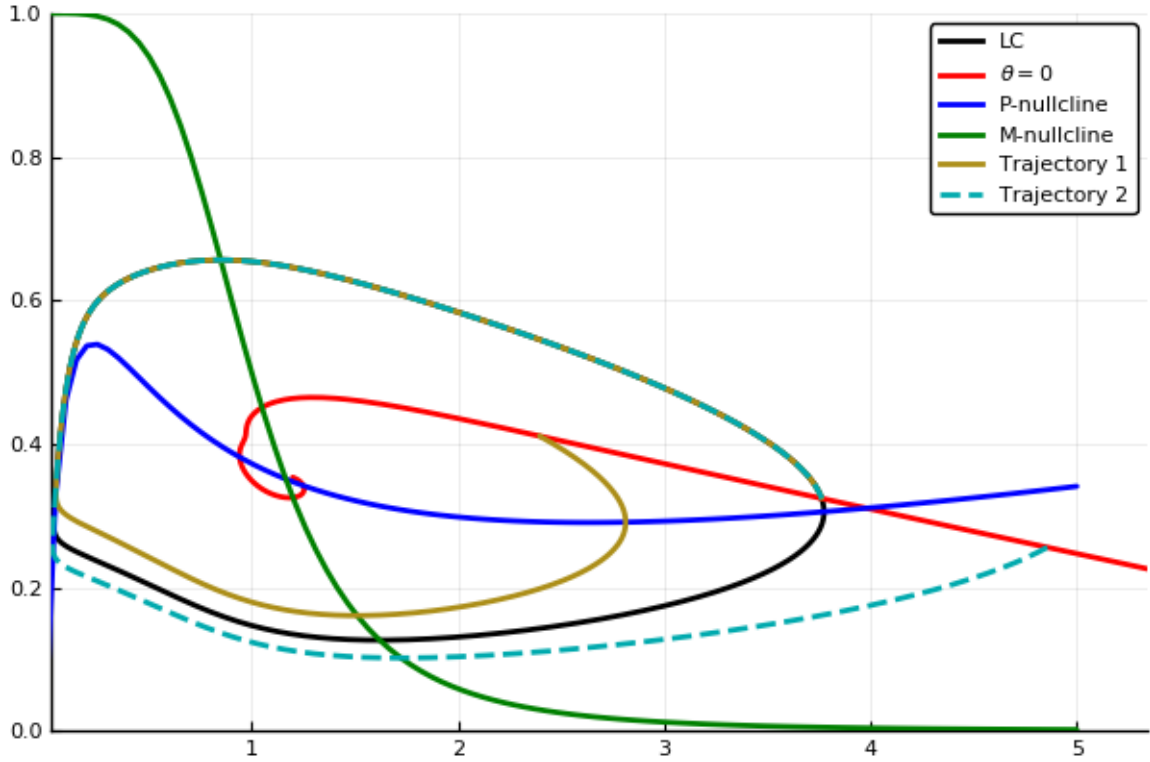


Figure 3.9 Single isochron at phase $\theta = 0$, along with two testing trajectories.

In Figure 3.10, we plot the set of isochrons $\mathcal{I}(\theta) : \theta = 0 : 1 : T$ in the same phase plane. We also add a zoom in figure on the right, where you can see that there is a phaseless region for this system.

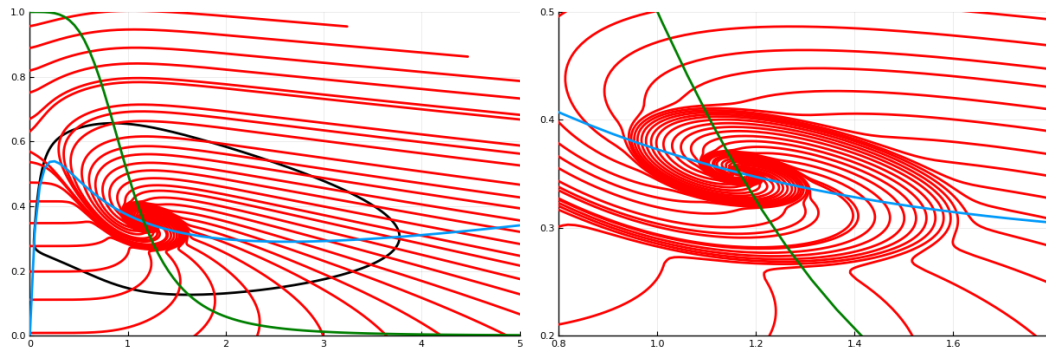


Figure 3.10 The left panel shows 40 isochrons of unforced NT. The right panel is a zoom in figure of the isochrons near the fixed point.

For a forced NT system, we can rewrite it as:

$$\begin{aligned}\frac{1}{\phi} \frac{dP}{dt} &= F_1(P, M, t) \\ \frac{1}{\phi} \frac{dM}{dt} &= \epsilon F_2(P, M)\end{aligned}\tag{3.50}$$

For such forced system with a forced periodic solution $\gamma(t)$ with period $T = 24$, the parameterization is able to be derived near the forced limit cycle. The only difference with the unforced one is that the choice of initial phase point is fixed. So we need to fix the initial condition before computing the parameterization.

3.2.2 Parameterization on other systems

We also applied the method to the Fitz-Hugh Nagumo (F-N) model [19].

$$\begin{aligned}\frac{dV}{dt} &= c(V - V^3/3 + W + I) \\ \frac{dW}{dt} &= -(V + bW - a)/c\end{aligned}\tag{3.51}$$

The parameter values are $I = -0.4, a = 0.7, b = 0.8, c = 3$, which is the choice in Winfree's paper [55]. The numerical result we found matches their result, and has a better accuracy. See Figure 3.11.

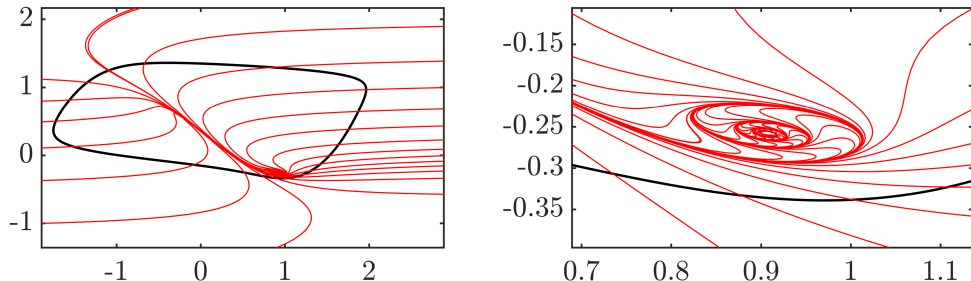


Figure 3.11 The left panel shows 20 isochrons of the F-N model. The right panel is a zoom in figure of the isochrons near the fixed point.

We then applied the method to the Morris-Lecar (M-L) model [44].

$$\begin{aligned} C_M \frac{dV}{dt} &= -g_L(V - V_L) - g_{Ca}M_\infty(V - V_{Ca}) - g_KW(V - V_K) + I_{ext} \\ \frac{dW}{dt} &= \lambda_W(W_\infty - W) \end{aligned} \quad (3.52)$$

Here we have

$$\begin{aligned} M_\infty &= 0.5[1 + \tanh\{(V - V_1)/V_2\}] \\ W_\infty &= 0.5[1 + \tanh\{(V - V_3)/V_4\}] \\ \lambda_W &= \phi \cosh\{(V - V_3)/2V_4\}. \end{aligned} \quad (3.53)$$

With parameters: $g_L = 2, g_{Ca} = 20, g_K = 20, I_{ext} = 60, V_K = -100, V_L = -70, V_{Ca} = 50, V_1 = 0, V_2 = 18, V_3 = -10, V_4 = 13, \phi = 0.15, C_M = 2$. The isochrons are presented in Figure 3.12.

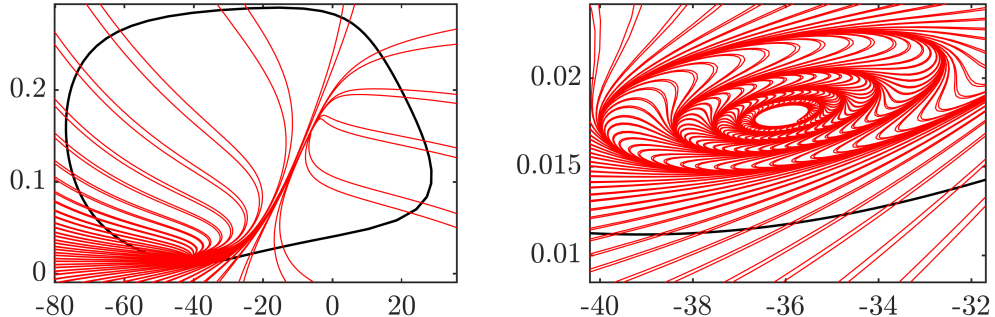


Figure 3.12 The left panel shows 30 isochrons of the M-L model. The right panel is a zoom in figure of the isochrons near the fixed point.

3.2.3 Coupled Novak-Tyson model

The coupled Novak-Tyson (CNT) model is given by the following equations:

$$\begin{aligned} \frac{1}{\phi_1} \frac{dP_1}{dt} &= M_1 - k_f h(P_1) - k_D P_1 - k_{L_1} f(t) P_1 \\ \frac{1}{\phi_1} \frac{dM_1}{dt} &= \epsilon [g(P_1) - M_1] \\ \frac{1}{\phi_2} \frac{dP_2}{dt} &= M_2 - k_f h(P_2) - k_D P_2 - k_{L_2} f(t) P_2 \\ \frac{1}{\phi_2} \frac{dM_2}{dt} &= \epsilon [g(P_2) - M_2 + \alpha_1 M_1 g(P_2)] \end{aligned} \quad (3.54)$$

The parameters and variables have the same meaning as the original NT model. We introduce a coupling term $\alpha_1 M_1 g(P_2)$, from oscillator 1 (O_1) to oscillator 2 (O_2). The parameter α_1 is a non-negative real number which denotes the coupling strength. We placed the coupling factor into the second equation of O_2 based on Roberts et al. [50], who suggest that coupling occurs between the mRNA production rates.

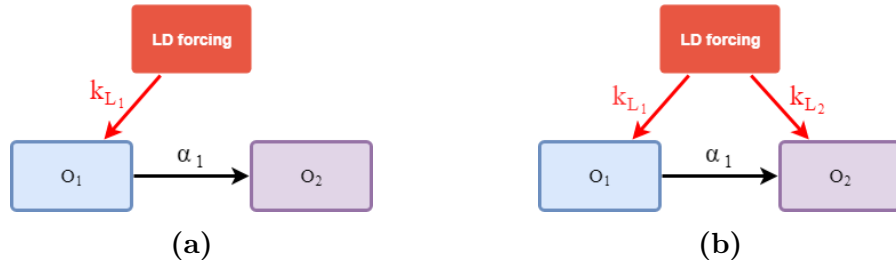


Figure 3.13 (a) Model with strict hierarchical coupling. (b) Semi-hierarchical model when both oscillators receive light input, but the light into O_2 is much weaker than the light into O_1 .

We mainly study the case with strict hierarchical coupling, which is shown in Figure 3.13a. In this case, the LD forcing is applied only on O_1 , which then has feedforward coupling onto O_2 . We fix the value of parameter $k_{L_2} = 0$. Figure 3.13b shows the semi-hierarchical CNT model when both oscillators receive light forcing, but the effect of light into O_2 is taken to be less intense than that into O_1 , in other words, $k_{L_2} < k_{L_1}$.

The entrainment map When attempting to determine the existence of periodic solutions using Poincaré maps, one has to decide where in phase space to place the section. Often in circadian models, the Poincaré section is placed on the 24-hour light-dark forcing, leading to a stroboscopic map that determines the state of the system every 24 hours. In [14], Diekman and Bose instead placed the section in the phase space of the circadian oscillator and backed out the phase of light when the oscillator was at the section. Here, we follow that approach when building the 2-D map. The Poincaré section is chosen at a location in the flow that O_2 is shown in Section 3 to cross. The phase of O_1 with respect to a reference point on its own limit cycle, x , and of lights y will then be determined to derive the 2-D map. In this section, we first introduce the original 1-D map, and then generalize it to our 2-D map.

The entrainment map $\Pi(y)$ for the original NT model was introduced as a 1-D map in [14]. To define $\Pi(y)$, Diekman and Bose take a Poincaré section \mathcal{P} as a 1-D line segment which intersects the LD-trained solution of a single periodically forced NT oscillator. The section is placed along a portion of an attracting one-dimensional slow manifold where all trajectories of the NT oscillator pass. A phase variable y is defined to be the amount of time that has passed since the beginning of the most recent LD cycle. When the trajectory first returns to \mathcal{P} , the map $\Pi(y)$ is defined to be the amount of time that has passed since the onset of the most recent LD cycle, which is the new phase of the light forcing. The domain and range of $\Pi(y)$ are both $(0, 24]$. The domain is actually homeomorphic to the unit circle \mathbb{S}^1 , so $y = 0$ and $y = 24$ are equivalent. The map is written as $y_{n+1} = \Pi(y_n)$, where:

$$\Pi(y_n) = (\rho(y_n) + y_n) \bmod 24. \quad (3.55)$$

$\rho(y)$ is a return time map that measures the time a trajectory starting on \mathcal{P} takes to return to \mathcal{P} . It is continuous and periodic at its endpoints $\rho(0^+) = \rho(24^-)$. If $\rho(y) < 24 - y$, then $\Pi(x) = \rho(y) + y$, because the trajectory will return back to \mathcal{P} within the same LD cycle which it started. If $24 - y < \rho(y) < 48 - y$, then $\Pi(y) = \rho(y) + y - 24$, because the trajectory will return in the next LD cycle and so on.

If there exists a y_s , such that $y_s = \Pi(y_s)$ and $|\Pi'(y_s)| < 1$, then y_s is a stable fixed point of the map $\Pi(y)$, and it also determines a 1:1 phase locked solution. The phenomenon of 1:1 phase locking in this case occurs when the oscillator has one return to the Poincaré section for every one period of the LD forcing. When a stable solution exists, the map $\Pi(y)$ quite accurately calculates the time to approach the stable solution starting from any initial condition of y . Numerically we use the concept of entrainment to evaluate the convergence time. Suppose y_j is a sequence of iterates of the map, then we say the solution is entrained if there exists m , such that for all $j \geq m$, $|y_s - y_j| < 0.5$. The entrainment time is then $\Sigma_{i=1}^m \rho(y_i)$.

The 1-D O_1 -entrained map for the CNT system The 1-D map for the NT system can not be directly applied to the CNT system, because the second oscillator will have additional free variables to determine, meaning that the entrainment map for the CNT system will be higher dimensional. However, for the hierarchical CNT system, if we assume that O_1 is already entrained, then the chain $LD \Rightarrow O_1 \Rightarrow O_2$ is reduced to O_1 -entrained $\Rightarrow O_2$. The system can be rewritten in the following manner:

$$\begin{aligned} \frac{1}{\phi_2} \frac{dP_2}{dt} &= M_2 - k_f h(P_2) - k_D P_2 \\ \frac{1}{\phi_2} \frac{dM_2}{dt} &= \epsilon [g(P_2) - M_2 + \alpha_1 M_1 g(P_2)] \end{aligned} \tag{3.56}$$

In the O_1 -entrained case, O_2 is continuously forced by the coupling from O_1 . This differs from the coupling due to direct light input into O_1 which is a discontinuous square wave. We place a Poincaré section that intersects the entrained O_2 limit cycle solution at $\mathcal{P} : P_2 = 1.72, |M_2 - 0.1289| < \delta$ such that $P'_2 < 0$, where δ is a small control parameter. In the Results section, we will explain why trajectories are funneled into a region that forces them to cross this choice of Poincaré section. Along the section \mathcal{P} , P_2 is fixed, and M_2 is bounded by δ , so the only free variable is the phase of light. We define the 1-D O_1 -entrained map by

$$y_{n+1} = \Pi_{O_1}(y_n) = (y_n + \rho(y_n; \gamma(y_n))) \bmod 24 \quad (3.57)$$

where $y \in (0, 24]$ is defined to be the phase of the LD forcing, which has the same meaning as the 1-D entrainment map in [14]. We define $\gamma(t) := \varphi_t(X_0)$ to be the LD-entrained limit cycle of O_1 , where X_0 is a chosen reference point on $\gamma(t)$. We denote the set of points that lie on the limit cycle of O_1 by Γ_{O_1} . At X_0 , the lights just turn on for O_1 . In the O_1 -entrained case, the location of O_1 only depends on y_n and can be denoted by $\gamma(y_n)$. Based on the above definition, $\gamma(y_n)$ means a point on the limit cycle of O_1 when the light has been turned on for y_n hours. $\rho(y_n)$ measures the return time when O_2 first returns \mathcal{P} .

Notice that in the definition of the O_1 -entrained map, the phase of O_1 is determined by y (the phase of the LD forcing), since it is O_1 -entrained. This makes the O_1 -entrained map a 1-D map, and most of the properties of the NT model's 1-D map carry over to the O_1 -entrained map. For example, if there is a point y_s , such that $y_s = \Pi_{O_1}(y_s)$ and $|\Pi'_{O_1}(y_s)| < 1$, then y_s is a stable fixed point of the O_1 -entrained map. The fixed points of the map also determine 1:1 phase locked solutions of the coupled system.

The general 2-D entrainment map In the case of the O_1 -entrained map, the initial location of O_1 when O_2 lies on \mathcal{P} is always determined by y , the phase of the LD cycle. But in general, the initial location of O_1 doesn't always depend on y , rather it could lie arbitrarily in its phase space. To limit the possibilities, we restrict the initial location of O_1 to lie anywhere along its own limit cycle Γ_{O_1} . This restriction will therefore only introduce one new free variable and motivates us to generalize the map to two dimensions.

$$(x_{n+1}, y_{n+1}) = \Pi(x_n, y_n) = (\Pi_1(x_n, y_n), \Pi_2(x_n, y_n))$$

We keep the definition of y_n and the location of the Poincaré section \mathcal{P} the same as the O_1 -entrained map. We now introduce a new variable x to determine O_1 's position in phase space relative to its own LD-entrained solution. The detailed definition is explained using a phase angle.

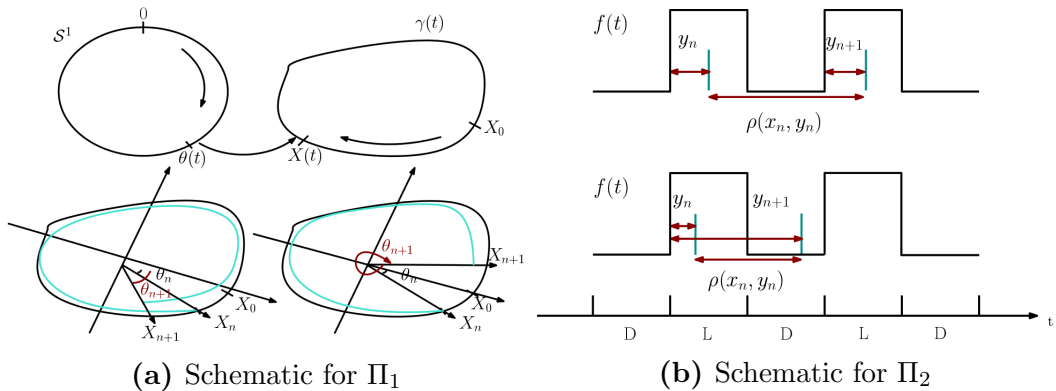


Figure 3.14 (a) The upper panel shows a schematic of the homeomorphism from the unit circle S^1 to Γ_{O_1} . The lower panel shows how we construct the map in two different conditions; the left one shows the case when the phase angle θ associated with the trajectory of O_1 rotates through more than 2π , the right one is where the rotation is less than 2π . (b) In both panel schematics, the first blue vertical line segment denotes where we chose the initial phase of light. After time $\rho(x_n, y_n)$, the trajectory returns to \mathcal{P} , and the new phase of light is y_{n+1} . For the upper panel, $y_n + \rho(x_n, y_n) > 24$, so $y_{n+1} = y_n + \rho(x_n, y_n) - 24$. For the lower panel, $y_n + \rho(x_n, y_n) < 24$, so $y_{n+1} = y_n + \rho(x_n, y_n)$. The black square wave $f(t)$ in both panels represents the LD forcing.

Defining Π_1 using a phase angle According to the O_1 -entrained map, the trajectory of O_1 always remains on Γ_{O_1} . However, if O_1 is not already entrained, then its trajectory may not lie on Γ_{O_1} but will instead approach it asymptotically. Thus, we need a new independent variable to determine the position of O_1 for this situation. From the O_1 -entrained case, the position of O_1 can always be described as $\gamma(t)$, where $t \in (0, 24]$. The idea is to define a new independent phase variable x equivalent to the time variable t that is obtained by projecting the real location of O_1 onto its limit cycle Γ_{O_1} , while keeping the error small.

We define the phase angle in the following steps:

1) Transform the coordinate system appropriately: Shift the origin to the intersection point of the uncoupled O_1 's two nullclines. Then connect the origin and the point X_0 and expand the line segment as the x-axis of the new coordinate system. The y-axis is determined automatically to be orthogonal to the x-axis, as in Figure 3.14a.

2) Define x in terms of the phase angle: Consider the phase plane as a complex plane \mathbb{C} . Let's call the point X_0 as $z_0 = r_0 e^{i\theta_0} \in \mathbb{C}$, where $\theta_0 = 0$ after the coordinate system transformation. We can then represent any point on the limit cycle $\gamma(t)$ as a complex number $z = r e^{i\theta}$, where we define $\theta \in (0, 2\pi]$. Then x is defined to be the phase of O_1 when choosing X_0 as the reference point. In other words, $z = \gamma(x) = r e^{i\theta}$. Notice that x is homeomorphic to the unit circle \mathbb{S}^1 , because $\theta = \text{Arg}(\gamma(x))$; see Figure 3.14a. The domain of x is also $\tilde{\mathbb{S}}^1 = (0, 24]$.

3) Define the map Π_1 . Suppose we start integrating the system with any initial condition (x_n, y_n) (see Figure 3.14a, lower panel as an example). After the time $\rho(x_n, y_n)$, O_2 returns to the Poincaré section, the new location of O_1 is now

$$\Psi_{\rho(x_n, y_n)}(\gamma(x_n)) = r_{n+1} e^{i\theta_{n+1}}$$

where $\Psi_t(X)$ is the flow of O_1 , and the phase angle is θ_{n+1} . We then find the unique point \hat{x} lying on Γ_{O_1} such that the phase angle of $\Psi_{\rho(x_n, y_n)}(\gamma(x_n))$ matches the angle associated with $\gamma(\hat{x})$. That is we choose \hat{x} such that $\text{Arg}(\gamma(\hat{x})) = \theta_{n+1}$. Geometrically, we are simply choosing \hat{x} as the associated value at which the ray passing through $\Psi_{\rho(x_n, y_n)}(\gamma(x_n))$ intersects $\gamma(t)$. We define $x_{n+1} = \hat{x}$. We can then write Π_1 as the following:

$$x_{n+1} = \Pi_1(x_n, y_n) = \{\hat{x} \in [0, 24) : \text{Arg}(\gamma(\hat{x})) = \theta_{n+1}\}. \quad (3.58)$$

4) To numerically compute the map Π_1 , we integrate an initial condition where O_1 lies along its limit cycle and O_2 at \mathcal{P} , and integrate the system until O_2 returns to the section. We then use a linear map to shift the new location of O_1 to the coordinate system we set up in step 1. MATLAB has a built-in function to find the phase angle of the new location. Using this angle, we locate a point on the limit cycle of O_1 , that we had previously partitioned, with the same phase angle.

The definition of Π_2 is straightforward. We just mimic the construction of the O_1 -entrained map. The only difference is that the return time function ρ depends on both x and y , because O_1 is no longer O_1 -entrained:

$$y_{n+1} = \Pi_2(x_n, y_n) = y_n + \rho(x_n, y_n) \bmod 24, \quad (3.59)$$

where $y \in \tilde{\mathbb{S}}^1 = (0, 24]$ is defined on a homeomorphism of the unit circle \mathbb{S}^1 , $y = h(\theta) = \frac{12}{\pi} \times \theta$.

The schematic Figure 3.14b depicts a way to understand the definition of Π_2 . The first blue vertical line segment signifies the initial phase of O_2 when it starts on \mathcal{P} when the light turns on y_n hours. After time $\rho(x_n, y_n)$, the trajectory returns to \mathcal{P} , signified by the second blue vertical line segment, with the lights having turned on

y_{n+1} hours ago. In the upper panel, $\rho(x_n, y_n) > 24 - y_n$, therefore the trajectory does not return to \mathcal{P} within the same LD cycle. In the lower panel, $\rho(x_n, y_n) < 24 - y_n$, therefore the trajectory does return to \mathcal{P} within the same LD cycle.

In this section, we first show simulations demonstrating the entrainment of the strictly-hierarchical CNT model. We then define and analyze a 1-D map in which O_1 is assumed to already be entrained. We call this the O_1 -entrained map. Understanding the 1-D map will facilitate the definition and analysis of the 2-D entrainment map. Finally, we extend the results to the semi-hierarchical case.

3.2.4 The entrained solutions of the CNT model

To find the entrained solutions and understand the geometry of the strictly-hierarchical CNT system in the presence of the LD cycle, the nullclines of each oscillator play an important role. The nullclines are the set of points where the right hand sides of (3.54) equal zero and will be different for each of the oscillators. For O_1 , there are two different P -nullclines corresponding to the dark or light condition manifested through the square-wave forcing $f(t)$ and a single M -nullcline.

$$\begin{aligned} N_{P_D} : M_1 &= k_f h(P_1) + k_D P_1 \\ N_{P_L} : M_1 &= k_f h(P_1) + (k_D + k_L) P_1 \\ N_{M_1} : M_1 &= g(P_1) \end{aligned} \tag{3.60}$$

For O_2 , there is a single P -nullcline (since $k_{L_2} = 0$), but a family of M -nullclines since the coupling from O_1 is continuous rather than discrete.

$$\begin{aligned} N_P : M_2 &= k_f h(P_2) - k_D P_2 \\ N_{M_2} : M_2 &= g(P_2) + \alpha_1 M_1 g(P_2) \end{aligned} \tag{3.61}$$

Each P -nullcline is a cubic shaped curve. Note that N_{P_D} and N_{P_L} are independent of the variables P_2 and M_2 . In the four-dimensional space (P_1, M_1, P_2, M_2) they actually correspond to hypersurfaces. But since the equations governing the evolution of O_1 are independent of O_2 , we simply project and view N_{P_D} and N_{P_L} as curves in (P_1, M_1) space (Figure 3.15a). We similarly view the sigmoidal nullcline N_{M_1} as a curve in this phase plane. We project the nullclines of O_2 onto the (P_2, M_2) space (Figure 3.15c). Note that N_{M_2} now represents a continuum of sigmoidal shaped curves that vary depending on the value of M_1 . When O_1 is entrained, along its limit cycle, the M_1 value is bounded between $\min|M_1(t)|$ and $\max|M_1(t)|$. Thus, N_{M_2} can oscillate between $N_M^{\min} : M_2 = g(P_2) + \alpha_1 \min|M_1(t)|g(P_2)$ and $N_M^{\max} : M_2 = g(P_2) + \alpha_1 \max|M_1(t)|g(P_2)$. We assume that any intersection between N_P and N_M occurs on the middle branch of the corresponding cubic nullclines. This will guarantee that any ensuing fixed points of the CNT system are unstable and will allow oscillations to exist.

We plot the entrained solution of the CNT by direct simulation. In our simulations, we take a specific set of parameters for equation (3.54), i.e. $\phi_1 = \phi_2 = 2.1$, $\epsilon_1 = \epsilon_2 = 0.05$, $k_D = 0.05$, $k_{L_1} = 0.05$, $k_{L_2} = 0$, $k_f = 1$, $\alpha_1 = 2$. In Figure 3.15a, the periodic solutions of O_1 are presented for different light conditions. The dashed black (red) limit cycle denotes the stable solution of O_1 in DD (LL) conditions. The solid red-black limit cycle denotes the LD-entrained solution of O_1 , with hourly markings shown by green open circles. We also show various nullclines and note that the M nullcline (yellow curve) is unique, but the P -nullcline (red and blue curve) varies between $M_1 = (k_D + k_L)P + k_f h(P)$ and $M_1 = k_D P + k_f h(P)$. The corresponding time courses are shown for the P_1 variable in Figure 3.15b.

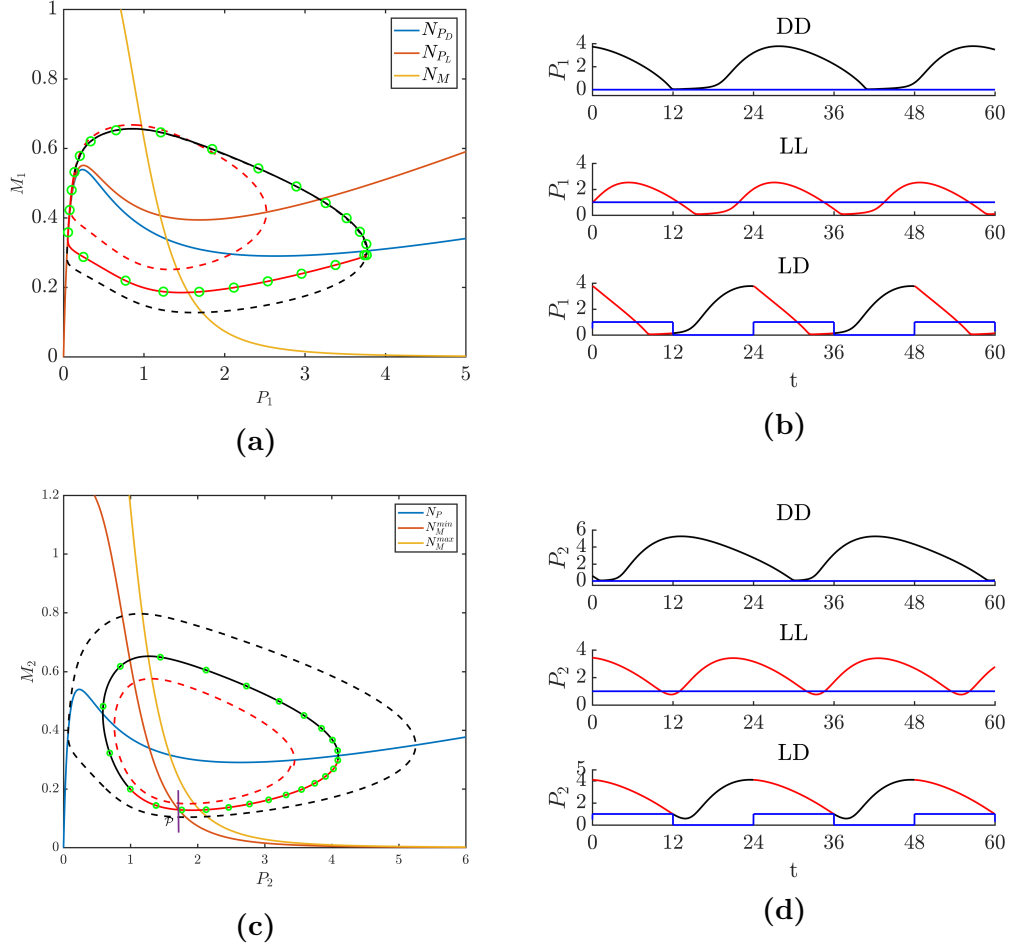


Figure 3.15 (a) The periodic solutions of O_1 in DD, LL and LD conditions. The dashed black trajectory represents the DD limit cycle ($f(t) \equiv 0$), the dashed red trajectory represents the LL limit cycle ($f(t) \equiv 1$). The solid trajectory represents the LD solution with green hourly markers. The two different P_1 nullclines, N_{P_D} and N_{P_L} and the single M_1 nullcline, N_M are shown. Note that for panels (a) and (c) the horizontal scale is much larger than the vertical scale. (b) The time course plots: P_1 vs t in all three cases (blue line lies at 0, 1 or is a square wave for DD, LL or LD, respectively. (c) The periodic solutions of O_2 when O_1 is in DD, LL and LD conditions. Same color scheme as in (a). The Poincaré section is represented at $P_2 = 1.72$ by a small vertical line segment. Note that only the maximal and minimal sigmoidal M_2 nullclines, N_M^{min} and N_M^{max} , are shown that bound the family of nullclines that exist for this case. (d) The time course plots: P_2 vs t in DD, LL and LD conditions.

In Figure 3.15c, we show the entrained solutions of O_2 when O_1 is in different light conditions. The color convention is the same as in Figure 3.15a. Here, we note that the P -nullcline (blue curve) is unique, but the M -nullcline (red and yellow curves)

varies between $M_2 = (1 + \alpha_1 \min|M_1(t)|)g(P_2)$ and $M_2 = (1 + \alpha_1 \max|M_1(t)|)g(P_2)$. We also show the time course plots related to the same condition in Figure 3.15d. The time course plots show that the period of the DD solution is longer than that of LD, and the period of LL solution is shorter than that of LD. In particular, we found that the period of the DD cycle is 28.9 h, which is the same as the DD cycle of O_1 , and the period of the LL cycle is 21.6 h, which is also the same as the LL cycle of O_1 . This is not surprising, because when the coupling strength is strong enough, O_2 is entrained by O_1 .

The nullclines shown in Figure 3.15c, together with the dashed LL and DD O_2 limit cycles, are useful to explain our choice of the Poincaré section at $P_2 = 1.72$, centered at $M_2 = 0.1289$. It is straightforward to use the vector field and phase plane analysis to show that any trajectory starting on \mathcal{P} will evolve counterclockwise and cross the right branch of N_P with $P_2 > 3$. Because of the difference in scaling of the vertical and horizontal components of that phase plane it is not so obvious to note that the M_2 value does not vary much for points along the right branch between where the LL (dashed red) and DD (dashed blue) limit cycles intersect it. In the LD situation, a trajectory will intersect the right branch of the N_P nullcline somewhere between a neighborhood of each of these points. We now show that any two trajectories with initial conditions lying on this nullcline in that region remain close in their M_2 value. Suppose we have a trajectory cross the right branch of N_P at $(\tilde{P}_2, \tilde{M}_2)$, where $\tilde{P}_2 > 3$, so that

$$\tilde{M}_2 = H(\tilde{P}_2) = k_f h(\tilde{P}_2) + k_D \tilde{P}_2$$

Taking a derivative of the function on the right hand side, and for convenience using x to represent the P_2 variable, yields

$$H'(x) = k_f h'(x) + k_D = k_f \frac{0.1 - x^2}{(0.1 + x + x^2)^2} + k_D.$$

When x is large, $H'(x) \rightarrow k_D$, implying $H(x) \approx k_D x$, where k_D is a small parameter. So when $\tilde{P}_2 > 3$,

$$H(x_1) - H(x_2) \approx k_D(x_1 - x_2)$$

Thus, the difference of M_2 between two points on the right branch of N_P is small. Next we show that those points have approximately the same dynamics in the M_2 direction. When P_2 is large, $g(P_2) \rightarrow 0$, the second equation of (3.56) is approximately

$$\begin{aligned} \frac{dM_2}{dt} &= -\phi_2 \epsilon M_2 \\ M_2(t) &= \tilde{M}_2 e^{-\phi_2 \epsilon t} \end{aligned}$$

The main point here is that the effect of M_1 is gone, so trajectories evolve largely independent of the coupling. Since any initial points lying on the region of the right branch of the N_P nullcline are close in their M_2 value, it is an easy application of Gronwall's Inequality to show that they remain close until P_2 becomes sufficiently smaller. Thus, those trajectories are funneled into the small region between the LL and DD limit cycles and cross the Poincaré section.

We note that our choice of Poincaré section is dictated by the funneling effect. For example, choosing the section elsewhere, say $P_2 = 3$, $|M_2 - 0.521| < \delta$, $\delta > 0$ but small, would not guarantee that trajectories cross through this section again.

Trajectories will, of course, cross $P_2 = 3$ with $P'_2 > 0$, but won't necessarily do so in a small neighborhood of the LD-entrained solution.

3.2.5 The O_1 -entrained map

The O_1 -entrained map we obtained from Eq. (3.57) has similar properties as the entrainment map Diekman and Bose constructed in their paper [14]. Figure 3.16 shows that there are two fixed points which correspond to different types of periodic solutions for the CNT system. The lower one with $y_{n+1} = y_n = 10.2$ is a stable fixed point of the map, which represents a stable periodic solution. The upper one with $y_{n+1} = y_n = 17.2$ is an unstable fixed point of the map.

We classify the direction of entrainment as occurring through phase advance or phase delay. Suppose $y_{n+1} = \Pi_{O_1}(y_n)$, and the return time needed from y_n to y_{n+1} is less than 24 hours. We call this a phase advance. Alternatively, if the return time is greater than 24 hours, we call it phase delay. The unstable fixed point of the map plays an important role in determining this direction. For example, pick two different initial conditions ($y_0 = 16.5, 18$) near the unstable fixed point and use the cobweb method to observe how different directions of entrainment can occur. For $y_0 = 16.5$, the iterates move to the left and converge to the stable solution by phase advance. For $y_0 = 18$ however, the iterates move to the right and converge to the stable solution by phase delay. In Figure 3.16(b), we compare the iterates with simulations; the green curve corresponds to $y_0 = 16.5$ and the magenta curve corresponds to $y_0 = 18$. The black curve is the entrained solution for O_2 . The direction of entrainment from the simulations agrees with the calculations obtained from the map.

In our model system, there are two parameters of interest, the coupling strength α_1 and the intrinsic period of O_2 governed by ϕ_2 . In Figure 3.16(c), we decrease α_1 from 2.5 to 1.4, so that the coupling strength is weaker. As a result, the return time $\rho(y)$ increases. This makes the map move up, and the stable and unstable fixed points

get closer to each other. At $\alpha_1 = 1.51$, the two fixed points collide at a saddle-node bifurcation. In Figure 3.16(d), we increase the intrinsic period of O_2 by decreasing ϕ_2 from 2.3 to 1.9, so that the difference between the intrinsic period and the 24-h forcing increases, which increases the return time to the Poincaré section. Hence the map moves up. When $\phi_2 = 1.91$, the map passes through the saddle-node bifurcation value. The disappearance of the stable fixed point means that in the full system 1:1 entrainment is lost and replaced by higher order periodic behavior. The details of this kind of behavior are interesting in their own right and we are systematically studying this in a separate paper.

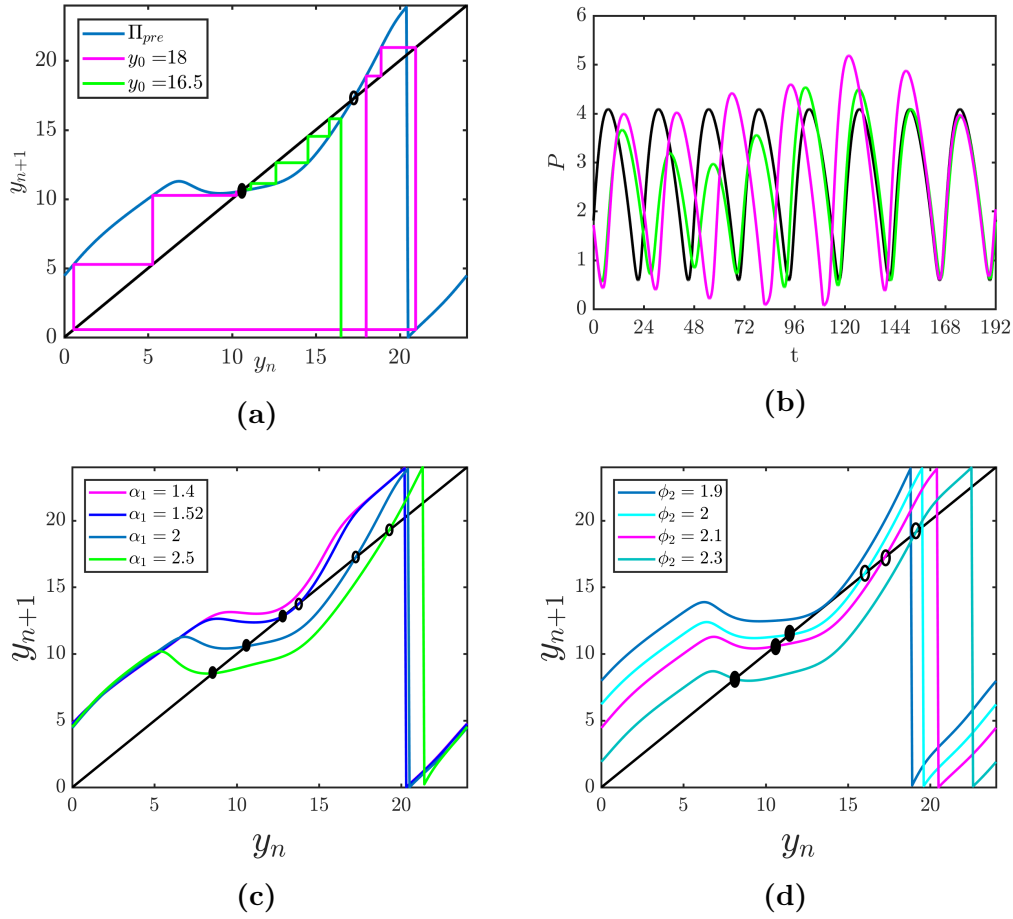


Figure 3.16 (a) The cobweb diagram for the O_1 -entrained map. We pick two different initial conditions and show how the iterates move to the stable fixed point. (b) The approach to the stable solution (black curve) in the t vs P plane; the colors correspond to the two initial conditions in (a). (c) The map displays a saddle-node bifurcation by decreasing α_1 . (d) Decreasing the intrinsic period of O_2 by decreasing ϕ_2 also leads the map to display a saddle-node bifurcation. Fixed points shown as open circles are unstable, and those shown with solid circles are stable.

Notice that the O_1 -entrained map we construct is not monotonic, which makes it different from the 1-D entrainment map found in [14]. To understand this nonmonotonicity, we take two initial conditions ($y_0 = 6$ and $y_0 = 8$) near the local maximum of the map in Figure 3.17(a), and analyze the dynamics of the system. Associated with the return time plot in Figure 3.17(b), we found that the return time is between 28 and 29 when y is less than the local maximum point. But when it crosses that point, the return time decreases quickly with the derivative $\rho'(y) < -1$. In Figure

3.17(c), we plot the trajectories with the two initial conditions. The trajectory for $y_0 = 6$ flows to the left branch of the P -nullcline, which increases the return time since evolution near this branch is slow. Alternatively, the trajectory for $y_0 = 8$ doesn't flow near the left branch and thus has a shorter return time. A minor consequence of this non-monotonicity is that some solutions converge to the stable fixed point by initially phase delaying, but then ultimately phase advancing. For example, in Figure 3.17(d), we take $y_0 = 18$ then cobweb the map. We find that the first four iterates initially phase delay. The fourth iterate lands near the local maximum of the map, which lies above the value of the fixed point. This causes subsequent iterates to phase advance. This non-monotonicity foreshadows a more complicated picture that arises under the dynamics of the 2-D map.

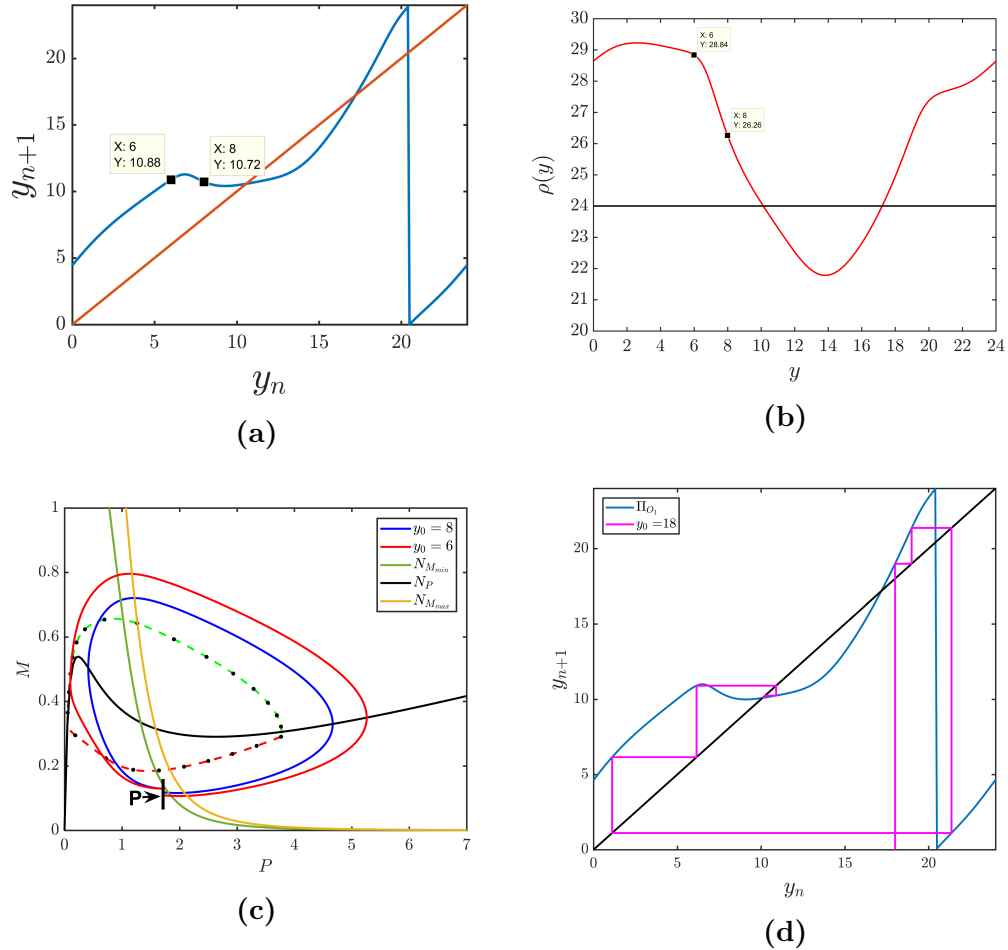


Figure 3.17 Non-monotonicity in the entrainment map leads to convergence initially due to phase delay but ultimately due to phase advance. (a) The non-monotone O_1 -entrained map and two choices of initial conditions near the local maximum. Note that the local maximum lies above the value of the fixed point of the map. (b) The return time plot associated with the two initial conditions. (c) The corresponding phase plane. The solid blue trajectory for $y_0 = 8$ does not approach the left branch of N_P , while the solid red trajectory for $y_0 = 6$ does, causing its evolution to slow down. (d) Starting with an initial condition $y_0 = 18$, the first four iterates phase delay. The fourth iterate lands near the local max of the map, and subsequent iterates then phase advance.

3.2.6 The results of the general 2-D map

In this section, the analysis of the 2-D map is presented. We follow ideas first derived by Akcay et al. [1] and followed up on in [2] to find fixed points of the map via a geometric method. The entrainment time and the direction of entrainment are

analyzed by iterating the map. We also compare these results with simulations. At the end of this section, we show that the map is also applicable to the semi-hierarchical model.

Basic results from the map Both parts of the 2-D map Π_1 and Π_2 are surfaces in relevant 3-D spaces. Because of the mod 24 operation, each surface will contain discontinuities. In Figure 3.18a and 3.18b, we project the surface onto the $x-y$ plane. For Π_1 , the purple part of the surface are points lying above the diagonal plane $z = x$, in other words, $x_{n+1} > x_n$. The red part of the surface of Π_2 are points lying above the diagonal plane $z = y$, i.e. $y_{n+1} > y_n$. The points of grey color denote all points that are below the diagonal planes, $x_{n+1} < x_n$ and $y_{n+1} < y_n$. The white curves indicate locations of discontinuity of the map. The separation of the two different colors are curves which indicate the points where $x = \Pi_1(x, y)$ and $y = \Pi_2(x, y)$. Here we define those curves as nullclines of the map:

$$N_x = \{(x, y) : x = \Pi_1(x, y)\}, \quad N_y = \{(x, y) : y = \Pi_2(x, y)\}$$

which are plotted in Figure 3.18c. The purple curves denote N_x . Similarly, the red curves denote N_y . Their intersections are four fixed points of the map. We numerically calculated the Jacobian at those fixed points and found the eigenvalues of the linearization. These values and the corresponding stability of each fixed point is shown in Table 3.1.

Table 3.1 Numerical Computation of the Eigenvalues of the Map at the Four Fixed Points

	x	y	eigenvalue	stability
A	10.6	10.6	0.1609, 0.4453	sink
B	17.2	17.2	2.0858, 0.4238	saddle
C	10.6	21.1	2.325, 0.2734	saddle
D	17.2	3.7	1.595+0.77 <i>i</i> , 1.595-0.77 <i>i</i>	source

From the results of the O_1 -entrained map, points A and B lying on the diagonal line correspond to the stable solution of O_1 . For O_2 , point A corresponds to the stable solution. For point B, the trajectory of O_2 returns to the Poincaré section after 24 hours but corresponds to the unstable solution of the O_1 -entrained map. At the fixed point C, O_1 lies on its own unstable periodic orbit. This can be inferred from and agrees with the calculation of Diekman and Bose [14] who showed that the original 1-D entrainment map has an unstable fixed point that corresponds to an unstable periodic orbit. Thus, O_1 is entrained to a 24-hour LD cycle and provides a 24-hour forcing to O_2 . From simulation, we found that the trajectory of O_2 stays for several cycles near what appears to be a stable limit cycle, though it is different from the limit cycle corresponding to point A since O_1 is unstable and the forcing signal to O_2 is different. At point D, if we check the difference between C and D, we can see that

$$(x_D, y_D) = (x_C, y_C) + 6.6 \text{ mod } 24$$

so O_1 is still on its unstable periodic orbit. That is, points C and D represent conditions where the forcing $M_1(t)$ is identical, but just phase shifted by 6.6 hours. Thus, O_2 still receives 24-hour forcing so we also expect there to exist an unstable O_2 limit cycle for this case.

One advantage of the map is its ability to estimate the entrainment time. Starting from different initial conditions, we iterate the map $(x_{n+1}, y_{n+1}) = \Pi(x_n, y_n)$ until $\|(x_{n+1}, y_{n+1}) - (x_s, y_s)\| < 0.5$, where point A has coordinates (x_s, y_s) . Then the entrainment time is the sum of the return times corresponding to each iterate. In Figure 3.18d, we show the entrainment times corresponding to different initial conditions on the torus expanded as a square. We also plot the nullclines N_x and N_y on top of it for illustrative purposes. The color for each point on the square denotes the entrainment time needed for that initial point.

Notice that, in Figure 3.18d, there are two light green curves. Along these curves, the entrainment time is much longer than other regions. Additionally, they appear to connect the two saddle points B, C, with the unstable source D. Though not proven here, we believe that these curves locate where the stable manifolds of the saddle points B and C ($W^s(B)$ and $W^s(C)$) are. To completely understand the dynamics of the entrainment map, it is useful to numerically find the stable and unstable manifolds.

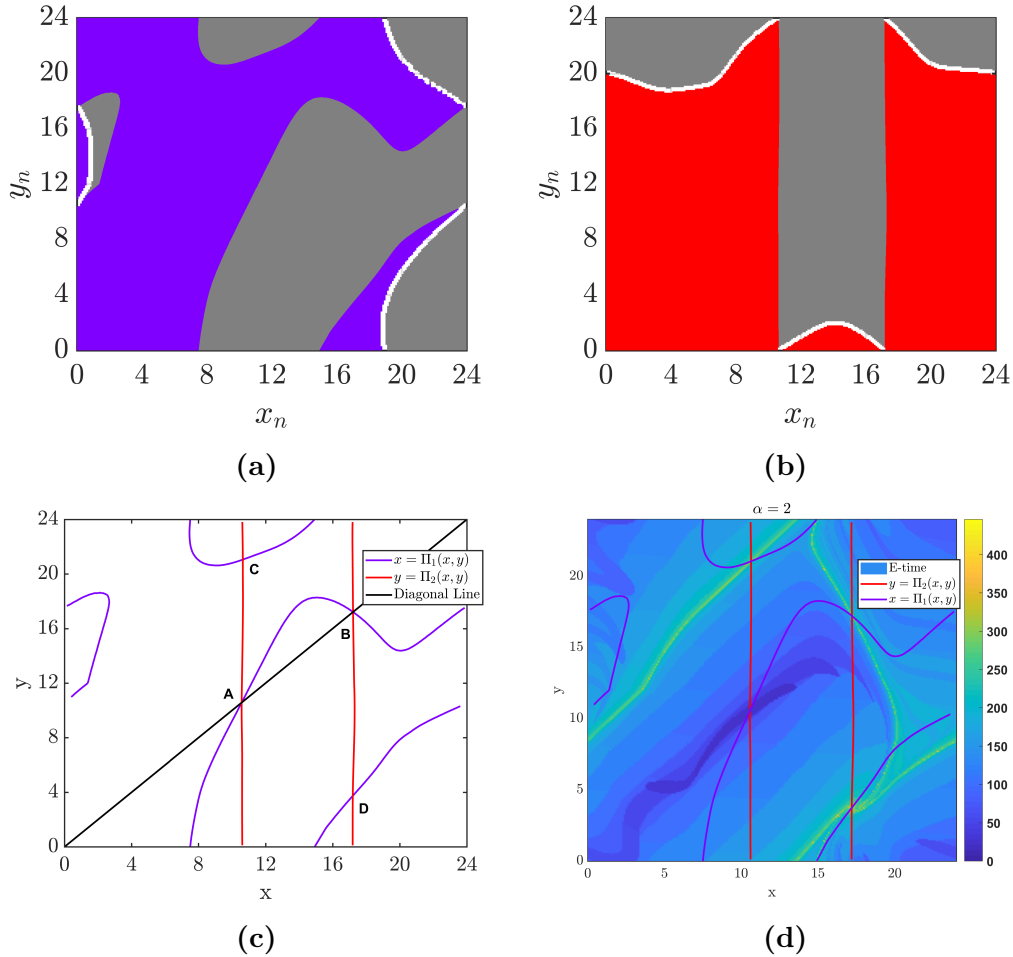


Figure 3.18 (a) and (b) The 2-D entrainment map is plotted as two separate maps Π_1 and Π_2 , and projected onto the domain space (x_n, y_n) . The purple and red color in both maps denote all points that are above the diagonal plane. The grey color denotes points that are below the diagonal plane. The white curves denote the discontinuity. (c) The purple curves denote points of Π_1 's nullcline N_x where $x = \Pi_1(x, y)$, the red curves denote points of Π_2 's nullcline N_y where $y = \Pi_2(x, y)$. Their intersections are the four fixed points of the map. (d) The entrainment time is plotted with a heatmap. The color denotes the entrainment time starting from a specific initial condition. The light green curves locate $W^s(B)$ and $W^s(C)$ from near which the longest entrainment times occur.

The algorithm we used to find the manifolds of the entrainment map are based on the following results. For the unstable manifold, Krauskopf and Osinga [32] introduced a growing method to calculate the unstable manifold point by point. They initially iterate points chosen in a neighborhood of the fixed point along the associated unstable eigenvector and accept new points as lying on the unstable manifold if they

satisfy specific constraints. For the stable manifold, the search circle (SC) method introduced by England et al. [17] utilizes the stable eigenvector to find points within a certain radius that iterate onto a segment of the stable eigenvector. The SC method has the advantage that it does not require the inverse of the map to exist, which is important for us since our map is non-invertible. Both of these methods are constructed for planar non-periodic domains. In our case, the map lives on a torus, but is graphically shown on a square. Whenever an iterated point exceeds the boundary of the square, we use the modulus operation to define the correct value within the square. Thus, we develop our algorithm to account for this discontinuity. Another difference is that the terminating conditions for both the growing and SC methods rely on calculating the arclength of the manifolds up to a certain predetermined length. However, in our map, the stable manifolds of points B and C are generated from the source point D, while their unstable manifolds terminate at point A. Thus, our algorithm terminates when these manifolds enter prescribed neighborhoods of those corresponding fixed points D and A.

In Figure 3.19a, we choose initial points ranging from $0 < x < 24, 0 < y < 24$, and iterate N times for each initial point. The arrows on each coordinate are pointing to its own next iterate. The obtained vector field give us another visualization of the map. In Figure 3.19b, the numerical result of stable and unstable manifolds of B and C are plotted. $W^s(B)$ and $W^s(C)$ agree with the light green curves in Figure 3.18d. $W^u(B)$ is exactly the diagonal line of the phase plane, which is not surprising. Because the diagonal line corresponds to the O_1 -entrained case, if an iterate starts on the diagonal line, it stays on it. The numerical calculation of the eigenvector of $E^u(B)$ is approximately $(0.7, 0.7)$ on the diagonal line, which means $W^u(B) = E^u(B)$. $W^u(C)$ also matches the darkest region in Figure 3.19(a). Indeed, these dark regions indicate the location of the unstable manifolds of points B and C.

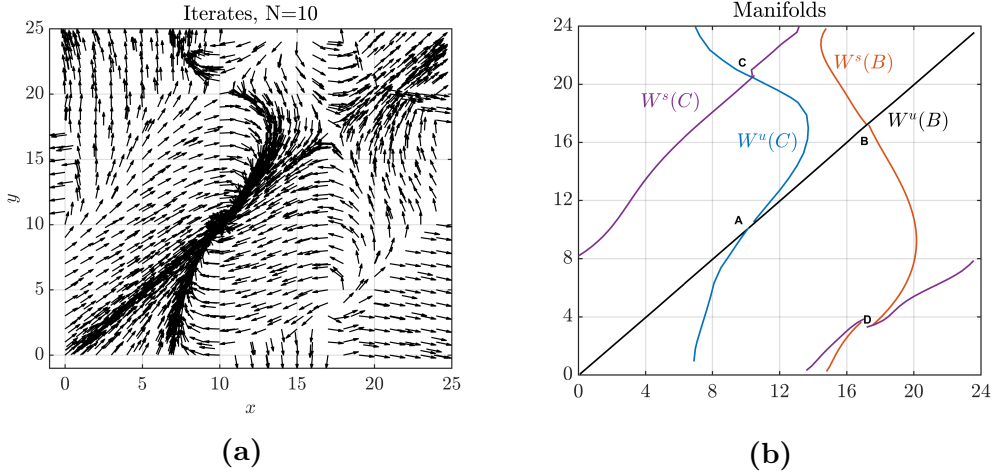
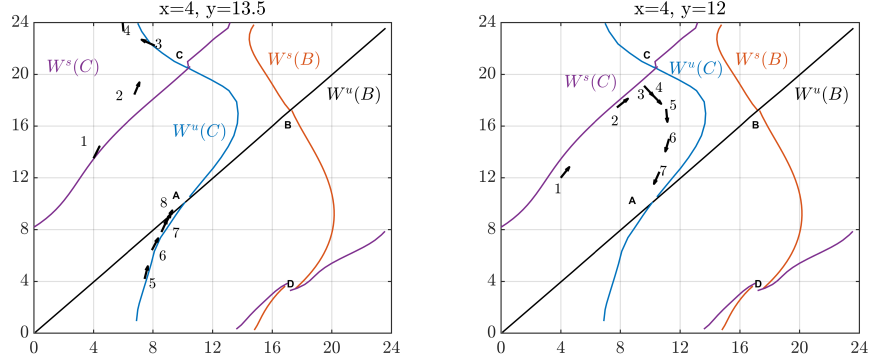


Figure 3.19 (a) $N = 10$ iterates from various initial points are shown. The arrows at each coordinate point in the direction of the next iterate. The vector field indicates that there may exist a separatrix type structure at both points B and C. (b) Stable and unstable manifolds of B and C as generated through the generalization of the search circle and growing methods (see text). The labeled manifolds do appear to provide a separatrix type behavior despite this being a map and not a flow.

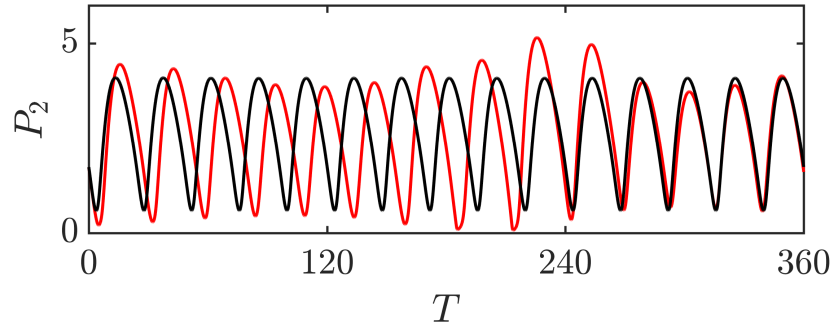
The located manifolds are also helpful for understanding the direction of entrainment of 2-D maps. In the case of 1-D map, the direction of entrainment is essentially either phase advance or delay, and the longest entrainment times happen for initial conditions lying near the unstable fixed point. In the case of 2-D map, the direction of entrainment need no longer be monotonic. The manifolds associated with the saddle points B and C appear to behave like a separatrix, despite this being a map and not a flow. To classify the direction of entrainment in the 2-D map, we consider phase delays and advances in the x and y directions separately. For the x direction, if the rotated angle from x_n to x_{n+1} is greater than 2π , we call it phase delay, otherwise we call it phase advance. For the y direction, we use the same definition as in the O_1 -entrained map. To illustrate different directions of entrainment, we pick several initial conditions near the stable manifolds, then iterate the map. We also run simulations with the same initial conditions for comparison. For Figure 3.20(a), in the left panel, we pick an initial point slightly above $W^s(C)$. It entrains to the

stable solution by phase delay in the y direction, and phase delay-advance-delay in the x direction. In the right panel, the initial point is slightly below $W^s(C)$, but the entrainment is through phase delay-advance in y , and phase delay-advance in x . The corresponding simulations in Figure 3.20(b) agree with the direction of entrainment found through the map and demonstrate the sensitivity to initial conditions.

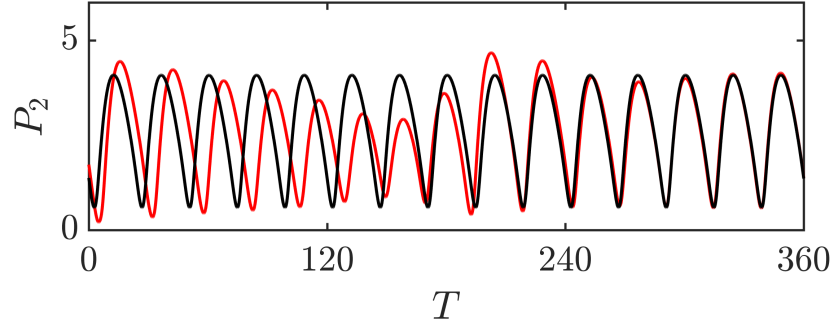


(a)

$x = 4, y = 13.5$



$x = 4, y = 12$



(b)

Figure 3.20 Direction of entrainment depends sensitively on initial conditions. (a) The initial point (labeled 1) in the left panel lies above $W^s(C)$, while the similarly labeled point in the panel to the right lies below $W^s(C)$. Numbers indicate iterates. As shown, the direction of entrainment differs significantly. (b) Corresponding simulations agree with the iterates. Note the top panel shows that O_2 (red time course) entrains through phase delay to the entrained solution (black time course); the lower panel shows O_2 entraining through phase delay-advance.

Parameter dependence of the map In the section on the O_1 -entrained map, we calculated the O_1 -entrained map for four different values of α_1 , and found the system

will lose entrainment if the coupling strength is too small. Now we calculate the 2-D map at different values of α_1 to see how the fixed points and the entrainment time depend on α_1 . In Figure 3.21a and 3.21b, we show the x and y nullclines for three different α_1 values; the points with solid circle are the stable fixed points, the points with open circles are the unstable fixed points, and the starred points are saddle points. In Figure 3.21c, we show the heatmap of entrainment times for $\alpha_1 = 1.52$. In Figure 3.21d, we show the heatmap of entrainment times for $\alpha_1 = 2.5$. Note that $\alpha_1 = 2$ is our canonical case, and was presented before in Figure 3.18d. Increasing α_1 , in general, decreases the entrainment time as can be observed from the color scale values (yellow max value ≈ 700 for $\alpha_1 = 1.52$) verus 400 for $\alpha_1 = 2.5$. In other words, stronger coupling between the central to peripheral oscillator speeds up entrainment.

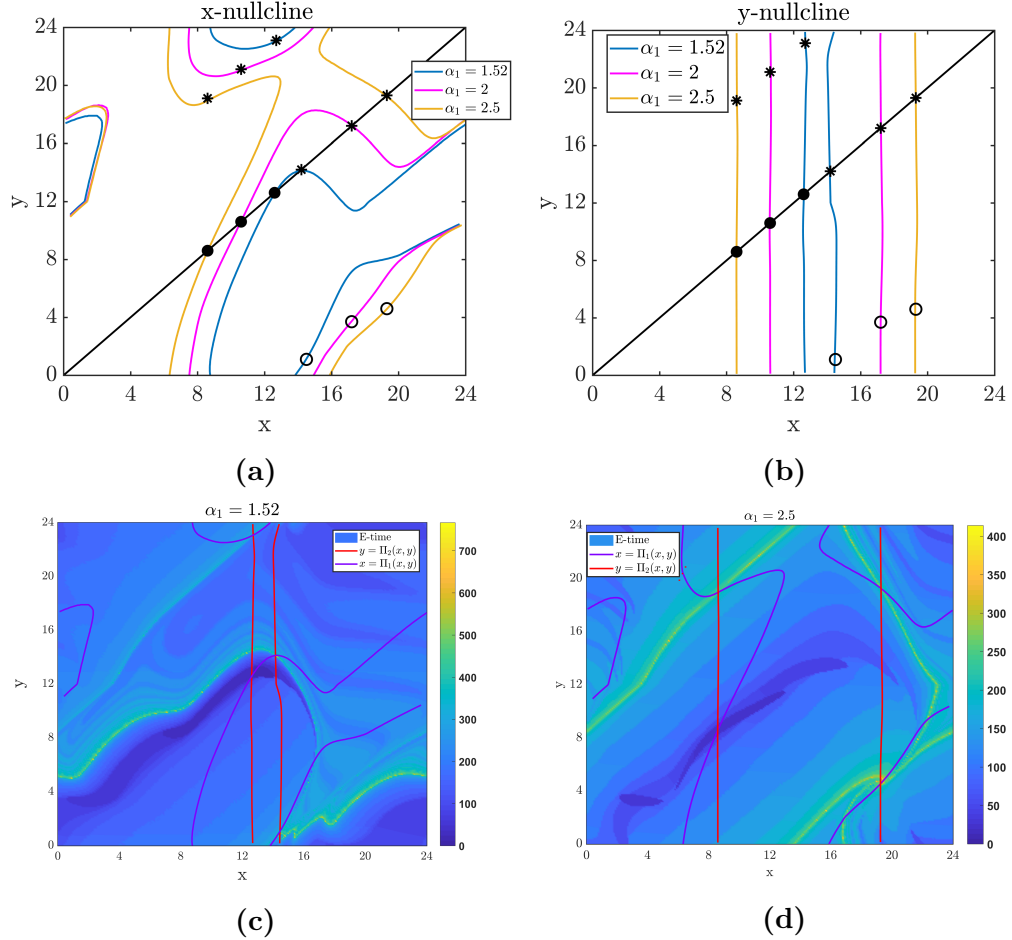


Figure 3.21 (a)-(b) The x and y nullclines under different α_1 values. Solid circles denote unstable fixed points, open circles stable fixed points, and stars saddle points. (c)-(d) The heatmap of entrainment times for different values of α_1 . Note the difference in numeric value of the maximum value of the color scale.

The 2-D map for the semi-hierarchical case For the strictly hierarchical model with only one feedforward connection from O_1 to O_2 , we have shown how to construct both the O_1 -entrained map and the general 2-D entrainment map. Here we will show that the 2-D map can be derived for the model when $0 < k_{L_2} < k_{L_1}$. In this case, O_1 is still dominant, allowing us to keep a semi-hierarchical structure.

We take $k_{L_2} = 0.025$, and keep the values of other parameters the same, so that O_1 and O_2 both receive light forcing. We define the Poincaré section $\mathcal{P} : P_2 = 1.72, |M_2 - 0.1548| < \delta$. We then obtained a 2-D map for this model. In Figure 3.22(a)

and (b), the top view of Π_1 and Π_2 are presented. In Figure 3.22(c), we similarly obtained 4 fixed points (A,B,C,D) as in the strictly hierarchical case. Compare to the strictly hierarchical model, we found that the additional light forcing into O_2 accelerates the entrainment process, so that the time to return to \mathcal{P} is decreased. Thus, the whole surface shifts down, which causes A to move to the left of the diagonal, and B to move to the right of the diagonal. For points C and D, the limit cycle of O_2 is now determined by both O_1 and the light forcing, which changes the location of C and D. In Figure 3.22(d), we calculated the first 10 iterates of each initial point. Comparing these results with the strictly hierarchical case, the stability of each fixed point remains unchanged, but their location has changed. Further, the entrainment time required for each initial condition is reduced because of the LD forcing into O_2 .

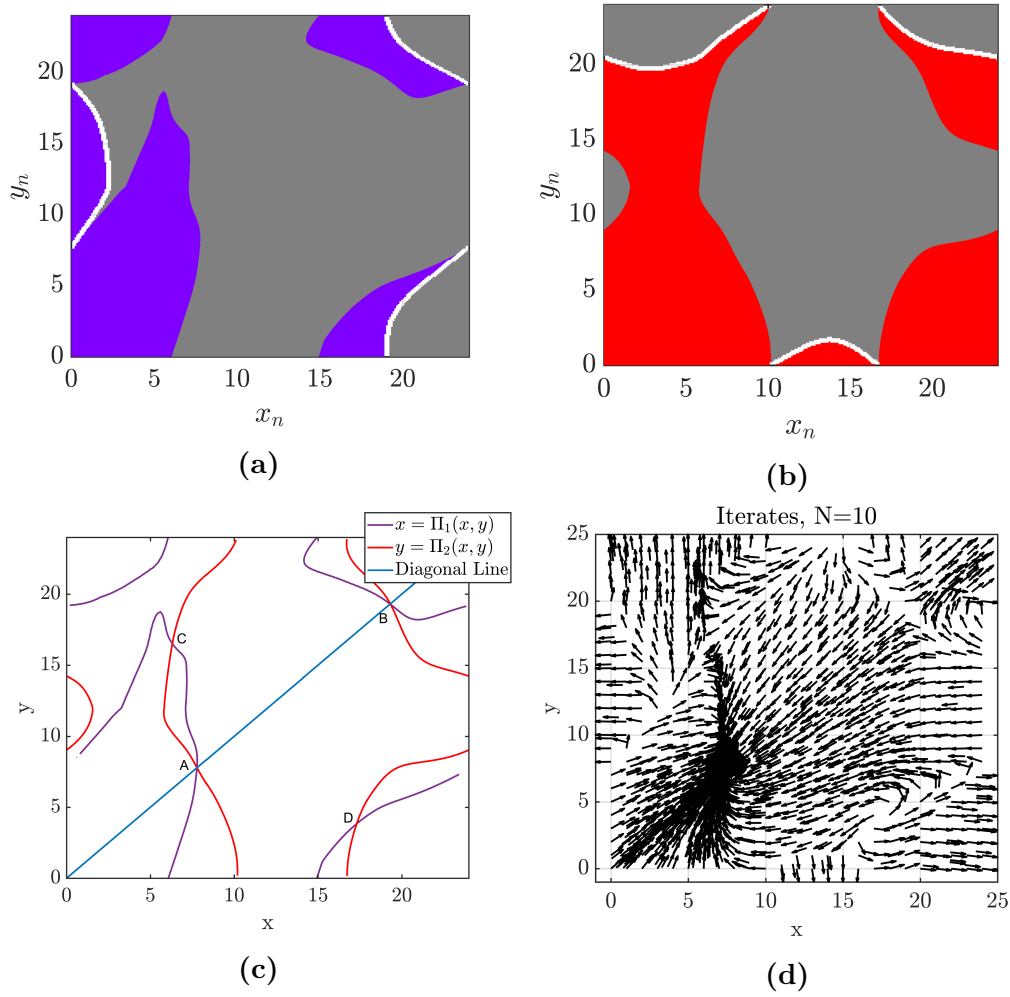


Figure 3.22 2-D semi-hierarchical case. (a)-(b) The top view of Π_1 and Π_2 are presented; see Figure 3.18a and 3.18b for an explanation of color coding. (c) we obtained 4 fixed points (A,B,C,D) with similar stability of the canonical model. (d) Ten iterates of each point. The vector field looks qualitatively similar to the strictly hierarchical case shown in Figure 3.19a.

CHAPTER 4

DISCUSSION

Circadian oscillations exist from the sub-cellular level involving genes, proteins and mRNA up to whole body variations in core body temperature. These oscillations are typically entrained to the 24-hour light dark cycle. Additionally, food, exercise, exterior temperature and social interactions can also act as entraining agents in certain species [43]. In these cases, various pathways in each species exist which carry the entraining information to relevant parts of the circadian system. In this thesis, we referred to the set of oscillators that first receive this input as central circadian oscillators. In turn, these central oscillators send signals about the time of day to other peripheral oscillators. When viewed in this manner, we obtain a hierarchical circadian system. For example, in the strictly hierarchical model (Figure 3.13a), the central oscillator O_1 could represent the suprachiasmatic nucleus (SCN), the master pacemaker in the hypothalamus of mammals. The peripheral oscillator O_2 that does not receive light input could represent circadian clocks in organs such as the heart or kidney. Alternatively, O_1 could represent the part of the SCN that directly receives light input (the ventral core), and O_2 could then represent the part of the SCN that does not (the dorsal shell) [26]. For the semi-hierarchical model (Figure 3.13b), O_1 and O_2 could represent the central and peripheral clocks in *Drosophila*, since in flies the clock protein cryptochrome is a photoreceptor and thus even peripheral organs receive some direct light input [13]. The main goal of this thesis has been to develop a low-dimensional method to study the basic properties of hierarchical systems such as the existence and stability of entrained solutions, together with how the phase and direction of entrainment of the constituent oscillators depends on important parameters.

4.1 Summary of the Main Results.

The major work of the dissertation involves model reduction techniques and mappings to understand limit cycle oscillators and phase models in the context of circadian rhythms. For the study of phase models, a modified coupled Kuramoto oscillator was introduced and the entrainment map was constructed to study the existence of periodic solutions and their stability. For the study of limit cycle oscillators, a coupled circadian oscillator (Novak-Tyson) was developed, different techniques were applied to understand the entrainment process and invariant manifolds of circadian oscillators.

Existing model reduction techniques and visualization of geometrical structures. In Chapter 2, the phase reduction method [8, 55, 27], Floquet theory and parameterization method were introduced. Phase reduction is a widely used technique to study weakly connected neural networks, but it is also limited by studying networks with weak couplings. The introduction of the Floquet normal form [20] allows the reduction for more general situations. A parameterization method [12] based on the Floquet theory was then introduced. A numerical algorithm of finding the limit cycle and the fundamental matrix solution was derived for the parameterization. The parameterization was applied on the NT model, FitzHugh-Nagumo model and Morris-Lecar model, and their isochrons were obtained. Additionally, an implementation of the Lagrangian descriptors method [40] was applied on the entrainment map of coupled Kuramoto oscillators.

Entrainment map for hierarchical coupled circadian oscillators In this dissertation, we have focused on how a hierarchical circadian system entrains to an external 24-hour light-dark cycle. We developed a method, partly analytic and partly computational, to assess the existence and stability of the entrained solution. Generalizing the approach of Diekman and Bose [14], we derived a Poincaré map by

placing a section in the phase space of the peripheral oscillator O_2 . The phase of O_1 with respect to a reference point on its own limit cycle, x , and of lights y was then determined to derive the 2-D map. The 2-D map approach was then applied on two models (coupled Kuramoto model and coupled Novak-Tyson model). With this approach, we were able to determine that over a large set of parameters, the 2-D map possesses four fixed points, each of which corresponds to a periodic orbit of the hierarchical circadian system. Only one of these fixed points is asymptotically stable. The other three fixed points are unstable. For the coupled Kuramoto model, a bifurcation analysis, Figure 3.3, is presented numerically to study how the stability of fixed points changes when two different parameters (forcing strength and coupling strength) change. We also showed how different manifolds connect with each other by the method of Lagrangian descriptors (Figure 3.6). This allowed us to better understand how these manifolds organized the iterate structure of the map. For the coupled NT model, We showed how one of them, labeled D in Figures 3.18c, 3.19a and 3.22d, is a source from which iterates emerge, including the stable manifolds of the two saddle points B and C. These manifolds appear to act as separatrices in the x - y domain of the map in the sense that, although they are for a map and not a flow, the manifolds separate the direction of convergence towards the stable fixed point A. Perhaps this is not so surprising as the saddle structure of the fixed points implies the existence of a saddle structure of the periodic orbits associated with points B and C. In the full five-dimensional phase space of the flow, each of the corresponding one-dimensional stable and unstable manifolds from the map become three dimensional; the motion along the O_1 and O_2 limit cycles provide the additional two dimensions. This would be enough to form a separatrix in the five-dimensional phase space.

There are several findings of our work that are readily revealed through the two-dimensional map. First, in a strictly hierarchical system, central oscillators

typically entrain first. This can be seen quite clearly from Figure 3.19a which shows that iterates of the map congregate along the diagonal line, which represents the O_1 -entrained subset of the two-dimensional map. This figure also shows that the peripheral oscillators may entrain in a different direction than the central oscillator or may in fact change their direction of entrainment during the transient. Given that direct light input speeds up entrainment, it is intuitively clear to see why entrainment times are, in general, less for semi-hierarchical compared to strictly hierarchical systems; Figure 3.22. A second finding involves the stable and unstable manifolds of the fixed points. Despite this being a map, these manifolds help to organize the iterate structure. In particular, the stable manifolds of the unstable saddle points create a tubular neighborhood of initial conditions that lead to very long entrainment times, as seen in Figure 3.18d. Determining that the unstable node and saddle points of the map actually exist is yet another important consequence of our map-based approach. Simulations alone would be unlikely to reveal either the existence or the role of these fixed points. Finally, effects of changing relevant parameters are readily explained using the map. For example, the limits on parameters of entrainment are readily observed if the coupling to the peripheral oscillator is too weak or if that oscillator is intrinsically too slow; Figure 3.16. Alternatively, stronger coupling from central to peripheral oscillators speeds up entrainment as shown in Figure 3.21.

When studying the invariant manifolds of the map, the Lagrangian descriptor method is applied to the map for coupled Kuramoto oscillators. Alternatively, to locate the manifolds of the map for coupled NT oscillators more accurately, the Search Circle (SC) method [17] and growing method [32] were applied to numerically compute the stable and unstable manifolds of fixed points. To implement these methods, we slightly changed each algorithm. The original growing method grows the points on the manifolds by controlling the distance and angle between consecutive mesh points, and terminates when a predetermined arclength is reached. In our entrainment map,

we know that the stable manifolds are generated from the source point, while their unstable manifolds terminate at the sink point. So our terminating condition is based on detecting when the manifolds reach a neighborhood of the source or sink points of the map. Another difference is that the domain is a square with identified sides, i.e. a torus. The value of the map at any point is computed as modulus by 24. When a manifold exceeds a boundary, it is reinjected on the opposite side of the square. This requires us to modify the existing methods to detect boundary crossings and then to restart the tracking of the manifold from the opposite side of the square. Thus each manifold is constructed in a piecewise manner.

Kuramoto model vs. CNT model We studied the entrainment map in two different models. The manner in which we add the hierarchical coupling to each model has biological differences. In the coupled Kuramoto model, the coupling is modeled as a sine function, which causes synchronization of the peripheral oscillator to the central oscillator. While in the CNT model, the coupling is modeled as a linear function to the M_2 equation of the second oscillator, which is based on the experimental results from Roberts et al. [50]. Biologically, it provides an inhibition to the second oscillator. However, the numerical results show some mathematical commonalities in both models. For example, we found the loss of entrainment through a saddle-node bifurcation in the 1-D map of both case. In the 2-D map, the manifolds of the saddle fixed points both behave like a separatrix of the direction of entrainment properties. Though the CNT model makes more sense as a circadian model, the coupled Kuramoto model is more straight forward to do analysis. In the CNT model, the 2-D map is a reduced system from a 5-D system, it is hard to prove the existence of unstable periodic orbits corresponding to the unstable fixed points, since the classical method would require the analysis of a 4-D Poincaré map, where the existence of fixed points of the map would imply the existence of actual periodic orbits of the

flow. However, we can easily prove the existence of unstable orbits in the coupled Kuramoto model, and we have additionally proved the upper bound of the number of fixed points.

Advantages and disadvantages of the entrainment map The map has the following advantages. Aside from allowing us to calculate entrainment times and directions as discussed above, the method provides a clear geometric description of why these results arise. Namely, the stable manifolds of various fixed points organize the iterate structure of the dynamics. Our method does not specifically require the LD forcing to be weak in amplitude or short in duration. This is in contrast to methods that use phase response curves and thus require weak coupling or short duration perturbations [8, 45].

Secondly, the dimension on which we perform analysis is reduced by one in the coupled Kuramoto phase model, and is significantly reduced from five to two dimensions in the coupled NT model. The classical Poincaré map can reduce the dimension of the original system by one. For example, Tsumoto et al. [53] construct a Poincaré map for 10-dimensional Leloup and Goldbeter model of the *Drosophila* molecular clock [36], reducing the dimension to 9. The phase reduction techniques of Brown et al. [8] can reduce the dimension of limit cycle oscillators to 1-D, however this method is not accurate for strong coupling.

There are some disadvantages of the map. First, the fixed points B, C and D of CNT map do not necessarily correspond to actual periodic orbits. This is because we restrict the type of perturbations that we are considering to allow only for a shift of the LD cycle or a shift of the central oscillator along its own limit cycle. In particular, we don't know if there is an unstable or stable structure outside the basin of attraction of the stable entrained solution without additional analysis. Secondly, the phase angle

method works well with two-dimensional systems. For higher dimensional systems, it would require additional assumptions.

4.2 Related Work

The mechanisms of communication between clock neurons is a topic of much ongoing research in the circadian field. The neuropeptide pigment-dispersing factor (PDF) is thought to act as the main synchronizing agent in the fly circadian neural network [38]. The analogue of PDF in the mammalian circadian system is vasoactive intestinal peptide (VIP), which plays a major role in synchronizing SCN neurons [41]. Although it is clear from studies with mutants that these neuropeptides provide important signals to synchronize circadian cells, the manner in which the signals interact with the molecular clock is not well understood [16]. Mathematical modeling can be used to explore the effect of different coupling mechanisms on clock network synchronization. In our model, we have assumed that production of the synchronizing factor is induced by activation of the clock gene in oscillator 1 (M_1), and that the effect of the synchronizing factor is to directly increase transcription of the clock gene in oscillator 2 (M_2). This type of coupling is similar to how Gonze et al. [22] modeled the action of VIP in the mammalian clock network, however in the Gonze model they included a linear differential equation for the production and decay of the coupling agent. Thus, in their model the coupling agent is a delayed version of the clock gene activity. In the Roberts et al [50] model of the fly clock network, the coupling signal is also increased by clock gene activity. As in our model, the coupling signal then instantaneously increases the clock gene transcription rate in other oscillators. In addition, the Roberts model included a second type of coupling where the coupling signal depends on clock protein levels, rather than clock gene activity, and the effect of the coupling signal is to instantaneously reduce the clock gene transcription rate in other oscillators. Their simulations suggested that networks with both coupling

types promoted synchrony and entrainment better than networks with either type of coupling alone. In a more detailed model of the fly clock network, Risau-Gusman and Gleiser [49] explored 21 different coupling mechanisms and found that synchronization of the network can only be achieved with a few of them. In future work, it would be interesting to use generalized entrainment maps to try to gain insight into why certain types of coupling promote synchrony and entrainment better than others.

Several prior modeling studies on entrainment of circadian oscillators exist. Bordyugov et al. [7] used the Kuramoto phase model and found, via Arnold tongue analysis, that the forcing strength and the oscillator amplitude both affect the entrainment speed. As noted in their work, a limitation of the method is that it only works for relatively weak coupling. An et al. [3] found that large doses of VIP (vasoactive intestinal polypeptide) reduce the synchrony in the SCN, which then reduces the amplitude of circadian rhythms in the SCN. In turn, they show that this leads to faster reentrainment of the oscillators in a jet lag scenario. Lee et al [34] directly introduced a linear phase model to study the entrainment processes. They found that the period of the central and peripheral oscillators are not the only predictors of the entrained phase. The intensity of light forcing to the central oscillator and the strength of coupling from the central to the peripheral oscillator also play a role in determining the stable phase. Their results are consistent with what we found for the O_1 -entrained map shown in Figure 3.16. Roberts et al [50] studied a population of coupled, modified, heterogeneous Goodwin oscillators under DD and single light pulse conditions. Their model simulations of a semi-hierarchical system show that because of heterogeneity, a single light pulse can desynchronize and phase disperse the oscillators. This can lead to a change in the coupling strength between oscillators which in turn leads to a new periodic solution of different amplitude than before the light pulse. Although they didn't consider 24-hour LD forcing, Roberts et al suggest that this desynchrony can be an important component in assessing reentrainment

of semi-hierarchical networks after jet lag. Our 2-D entrainment shows that this is indeed true. Namely, a shift in the light phasing that retains synchrony between O_1 and O_2 is equivalent to changing the initial y -value of our map, but keeping x fixed. Whereas a shift of light phasing accompanied by a desynchronization is equivalent to changing both x and y from the stable fixed point. As our simulations show (Figure 3.22d), the reentrainment process can be quite different in these two cases.

There are two modeling papers of hierarchical systems that are quite relevant to our work. In Leise and Siegelman [35], the authors consider a multi-stage hierarchical system to assess properties of jet lag. They utilized a two dimensional circadian model due to olde Scheper et al [47] to show that the direction of entrainment of peripheral oscillators need not follow that of the central oscillator. This is referred to as reentrainment by partition. To understand this idea more clearly, consider the concepts of orthodromic and antidromic reentrainment which are studied in the context of a time zone shift as in jet lag. Orthodromic reentrainment is defined as the oscillator shifting in the same direction as the forcing signal (e.g. advancing in response to an advance of the light/dark cycle) and antidromic reentrainment is when the oscillator shifts in the opposite direction as the forcing signal (e.g. delaying in response to an advance of the light/dark cycle). The situation is more complicated for hierarchical systems where different parts of the system may shift in different directions. For example, when Leise and Siegelman simulated a jet lag scenario involving a phase advance of 6 hours, they found that the pacemaker oscillator responded by phase advancing but the intermediate and peripheral oscillators responded by phase delaying. Similar to Leise and Siegelman, we also observe reentrainment by partition in our model. With the parameter values that we used in this dissertation, a 6-hour phase advance leads to orthodromic reentrainment in our model with both oscillators responding by phase advancing. However, simulating a 10-hour phase delay of the light-dark cycle places the initial

condition in the vicinity of the saddle fixed point C, leading to reentrainment through partition depending on the exact location relative to C. Our results are consistent with those of Leise and Siegelman, as they note that in their model reentrainment by partition can also be observed in response to phase delays of the light-dark cycle for certain values of the coupling strength between the master pacemaker and the intermediate component. The qualitative similarity in our results suggests that our findings can be used to infer that the Leise-Siegelman multistage model also possesses unstable saddle fixed points whose properties govern the reentrainment process. A second more recent paper due to Kori et al. [30] developed a hierarchical Kuramoto model to study the entrainment of circadian systems. They applied the model to predict the reentrainment time after two types of phase shifts, a single eight-hour shift versus a two-step shift with 4-hour shifts in each step. It turns out the latter requires fewer days to recover. In the dissertation, this can be related to the properties of stable manifolds of B or C. For example, in Figure 3.18d, for a single eight-hour shift near the fixed point A, the new point will stay close to $W^s(C)$, which makes the reentrainment time longer. For two successive four-hour shifts, the new point will be further from $W^s(C)$, which decreases the reentrainment time. This result generalizes findings from Diekman and Bose [15] and Kori et al. [30].

Regarding the numerical methods that we used to find stable and unstable manifolds, we basically applied the search circle for stable manifolds [17] and the growing method [32] for unstable manifolds. One difference between those methods and ours is the domain of the map, \mathbb{R}^2 versus a torus \mathbb{T}^2 in our case. Instead of growing one curve, our manifold is cut off when it hits the boundary of the domain. We then restart the calculation at the equivalent periodic point of the domain, e.g. $x = 24$ is reset to $x = 0$. Another difference is the terminating criteria for both growing and SC methods rely on calculating the arclength to a predetermined length. However, in our map, the manifolds are generated from a certain point (the source D or the sink

A), thus our algorithm terminates when those manifolds enter a neighborhood of the corresponding fixed points D and A.

Recently Castej  n and Guillamon derived a different 2-D entrainment map [10]. This map applies to a single oscillator (not necessarily a circadian oscillator), subject to pulsed periodic input. The variables of their map are the phase and amplitude of the oscillator. They use phase-response curve type methods to show that their 2-D map is more accurate in tracking the phase-locking dynamics as compared to a 1-D map of simply phase. While they use the term 2-D entrainment map, it appears that their method applies to a class of problems that are different than the ones considered in this dissertation.

4.3 Future Directions

The work of the entrainment map is based in part on analysis and in part on simulations. We have proved that the correspondence of the findings of the 2-D map, e.g. existence and stability of fixed points, actually exist for the hierarchical system of ODEs. We used a one-dimensional phase model, Kuramoto model [33] for each oscillator. Alternatively, we believe this method of mapping should be applicable to other models, such as Goodwin [23], Gonze [22] or Forger, Jewett, Kronauer [21] oscillators which are all higher dimensional. Verifying this, at the moment, would have to rely on checking agreement with simulations. The 2-D entrainment map should also be applicable to understand the interaction of circadian and sleep-wake rhythms to generalize the findings of Booth et al [6].

A necessary condition of our method is the existence of limit cycle solutions of the forced system, so that we can map any point in the phase plane to a point on the limit cycle. Light input is not the only forcing signal that a circadian oscillator receives. For instance, exercise, the intake of meals and taking melatonin can also be

considered as an external forcing. We would like to develop the entrainment map for multiple forcing signals.

Our expectation is that the method should work for any oscillators with a stable limit cycle. To apply our method to other limit cycle oscillators, the main difficulty is to determine a consistent way to assign phase to points in the phase plane that lie close to the limit cycle. In our current work this is done by a simple projection method. However, if the coupling between oscillators is strong, then the amplitude cannot be neglected, and we will have to extend the phase map into a phase-amplitude map to describe the entrainment process more precisely. A recent work, Castejon and Guillamon [10], developed a phase-amplitude entrainment map, and they applied the map for a canonical model. It would be of interest to extend their method for some classical circadian oscillators.

Diekman and Bose's paper [14] discussed how to build an entrainment map using real data instead of a mathematical model. This remains an open question even in the context of a 1-D map. How one might further extend this a hierarchical system is certainly an important next step to consider. The main challenge would involve how to perform perturbations of the phase relationship between peripheral and central oscillators in an experiment.

On the topic of revealing geometrical structure of dynamical systems, the Lagrangian descriptor method is applied for a 2-D entrainment map derived from coupled Kuramoto oscillators. It would be of interest to apply the method to the entrainment map of coupled NT oscillators.

The parameterization we introduced in Chapter 2 is valid for a one dimensional stable manifold. Only the first two terms (linear approximation) are computed, but we mentioned that the higher order term is solvable and is computable using Fourier series. The future work is to derive the practical recurrence equations

for the coefficients of the Fourier series. Another future direction is to apply the parameterization for unstable manifolds and higher dimensional stable manifolds.

REFERENCES

- [1] Zeynep Akcay, Amitabha Bose, and Farzan Nadim. Effects of synaptic plasticity on phase and period locking in a network of two oscillatory neurons. *J. Math. Neurosci.*, 4(1):8, 2014.
- [2] Zeynep Akcay, Xinxian Huang, Farzan Nadim, and Amitabha Bose. Phase-locking and bistability in neuronal networks with synaptic depression. *Phys. D*, 364:8–21, 2018.
- [3] Sungwon An, Rich Harang, Kirsten Meeker, Daniel Granados-Fuentes, Connie A Tsai, Cristina Mazuski, Jihee Kim, Francis J Doyle, Linda R Petzold, and Erik D Herzog. A neuropeptide speeds circadian entrainment by reducing intercellular synchrony. *Proc. Natl. Acad. Sci.*, 110(46):E4355–E4361, 2013.
- [4] J Aschoff. Problems of re-entrainment of circadian rhythms: asymmetry effect, dissociation and partition. In *Environmental endocrinology*, pages 185–195. Springer, Berlin, Heidelberg, 1978.
- [5] R Ben-Shlomo and B Kyriacou. Circadian rhythm entrainment in flies and mammals. *Cell Biochem Biophys*, 37:141–156, 2002.
- [6] Victoria Booth, Ismael Xique, and Cecilia G Diniz Behn. One-dimensional map for the circadian modulation of sleep in a sleep-wake regulatory network model for human sleep. *SIADS*, 16(2):1089–1112, 2017.
- [7] Grigory Bordyugov, Ute Abraham, Adrian Granada, Pia Rose, Katharina Imkeller, Achim Kramer, and Hanspeter Herz. Tuning the phase of circadian entrainment. *J. R. Soc., Interface*, 12(108):20150282, 2015.
- [8] Eric Brown, Jeff Moehlis, and Philip Holmes. On the phase reduction and response dynamics of neural oscillator populations. *Neural Comput.*, 16(4):673–715, 2004.
- [9] Xavier Cabré, Ernest Fontich, and Rafael De La Llave. The parameterization method for invariant manifolds iii: overview and applications. *Journal of Differential Equations*, 218(2):444–515, 2005.
- [10] Oriol Castejón and Antoni Guillamon. Phase-amplitude dynamics in terms of extended response functions: Invariant curves and arnold tongues. *Commun Nonlinear Sci.*, 81:105008, 2020.
- [11] Oriol Castejón, Antoni Guillamon, and Gemma Huguet. Phase-amplitude response functions for transient-state stimuli. *The Journal of Mathematical Neuroscience*, 3(1):13, 2013.

- [12] Roberto Castelli, Jean-Philippe Lessard, and Jason D Mireles James. Parameterization of invariant manifolds for periodic orbits i: Efficient numerics via the floquet normal form. *SIAM Journal on Applied Dynamical Systems*, 14(1):132–167, 2015.
- [13] Ruchi Chauhan, Ko-Fan Chen, Brianne A Kent, and Damian C Crowther. Central and peripheral circadian clocks and their role in alzheimer’s disease. *Dis. Models Mech.*, 10(10):1187–1199, 2017.
- [14] Casey O Diekman and Amitabha Bose. Entrainment maps: A new tool for understanding properties of circadian oscillator models. *J. Biol. Rhythms*, 31(6):598–616, 2016.
- [15] Casey O Diekman and Amitabha Bose. Reentrainment of the circadian pacemaker during jet lag: East-west asymmetry and the effects of north-south travel. *J. Theor. Biol.*, 437:261–285, 2018.
- [16] Christine Dubowy and Amita Sehgal. Circadian rhythms and sleep in drosophila melanogaster. *Genetics*, 205(4):1373–1397, 2017.
- [17] James P England, Bernd Krauskopf, and Hinke M Osinga. Computing one-dimensional stable manifolds and stable sets of planar maps without the inverse. *SIADS*, 3(2):161–190, 2004.
- [18] G Bard Ermentrout. n: m phase-locking of weakly coupled oscillators. *Journal of Mathematical Biology*, 12(3):327–342, 1981.
- [19] Richard FitzHugh. Impulses and physiological states in theoretical models of nerve membrane. *Biophysical journal*, 1(6):445, 1961.
- [20] Gaston Floquet. Sur les équations différentielles linéaires à coefficients périodiques. In *Annales scientifiques de l’École normale supérieure*, volume 12, pages 47–88, 1883.
- [21] Daniel B Forger, Megan E Jewett, and Richard E Kronauer. A simpler model of the human circadian pacemaker. *J. Biol. Rhythms*, 14(6):533–538, 1999.
- [22] D Gonze, S Bernard, C Waltermann, A Kramer, and H Herzel. Spontaneous synchronization of coupled circadian oscillators. *Biophys J*, 89:120–129, 2005.
- [23] B Goodwin. Oscillatory behavior in enzymatic control processes. *Adv Enzyme Regul*, 3:425–428, 1965.
- [24] Changgui Gu, Huijie Yang, and Zhongyuan Ruan. Entrainment range of the suprachiasmatic nucleus affected by the difference in the neuronal amplitudes between the light-sensitive and light-insensitive regions. *Phys. Rev. E*, 95(4):042409, 2017.

- [25] Antoni Guillamon and Gemma Huguet. A computational and geometric approach to phase resetting curves and surfaces. *SIAM Journal on Applied Dynamical Systems*, 8(3):1005–1042, 2009.
- [26] Sato Honma. The mammalian circadian system: a hierarchical multi-oscillator structure for generating circadian rhythm. *J Physiol Sci*, 68(3):207–219, 2018.
- [27] E Izhikevich and F Hoppensteadt. Weakly connected neural networks. Springer, New York, NY, 1997.
- [28] Jaekyoung Kim and Daniel Forger. A mechanism for robust circadian timekeeping via stoichiometric balance. *Mol Syst Biol*, 8:630, 2012.
- [29] Karl E Klein, Reinhold Herrmann, Paul Kuklinski, and Hans-M Wegmann. Circadian performance rhythms: experimental studies in air operations. In *Vigilance*, pages 111–132. Springer, Boston, MA, 1977.
- [30] Hiroshi Kori, Yoshiaki Yamaguchi, and Hitoshi Okamura. Accelerating recovery from jet lag: prediction from a multi-oscillator model and its experimental confirmation in model animals. *Sci. Rep.*, 7:46702, 2017.
- [31] Kurt Kräuchi. How is the circadian rhythm of core body temperature regulated? *Clin. Auton. Res.*, 12(3):147–149, 2002.
- [32] Bernd Krauskopf and Hinke Osinga. Growing 1d and quasi-2d unstable manifolds of maps. *J. Comput. Phys.*, 146(1):404–419, 1998.
- [33] Y Kuramoto. *Chemical Oscillations, Waves, and Turbulence*. Springer: Heidelberg, Germany, 1984.
- [34] Kwangwon Lee, Prithvi Shiva Kumar, Sean McQuade, Joshua Y Lee, Sohyun Park, Zheming An, and Benedetto Piccoli. Experimental and mathematical analyses relating circadian period and phase of entrainment in *neurospora crassa*. *J. Biol. Rhythms*, 32(6):550–559, 2017.
- [35] T Leise and H Siegelmann. Dynamics of a multistage circadian system. *J Biol Rhythms*, 21:314–323, 2006.
- [36] Jean-Christophe Leloup and Albert Goldbeter. A model for circadian rhythms in drosophila incorporating the formation of a complex between the per and tim proteins. *J. Biol. Rhythms*, 13(1):70–87, 1998.
- [37] Howard Levine. Health and work shifts. *Shift Work and Health. RENTOS, PG, SHEPHARD, RD (eds.). Washington D.C. : US Dept. Health, Ed. and Welfare*, pages 57–69, 1976.
- [38] Yiying Lin, Gary D Stormo, and Paul H Taghert. The neuropeptide pigment-dispersing factor coordinates pacemaker interactions in the drosophila circadian system. *Journal of Neuroscience*, 24(36):7951–7957, 2004.

- [39] Carlos Lopesino, Francisco Balibrea, Stephen Wiggins, and Ana M Mancho. Lagrangian descriptors for two dimensional, area preserving, autonomous and nonautonomous maps. *Communications in Nonlinear Science and Numerical Simulation*, 27(1-3):40–51, 2015.
- [40] Ana M Mancho, Stephen Wiggins, Jezabel Curbelo, and Carolina Mendoza. Lagrangian descriptors: A method for revealing phase space structures of general time dependent dynamical systems. *Communications in Nonlinear Science and Numerical Simulation*, 18(12):3530–3557, 2013.
- [41] Cristina Mazuski and Erik D Herzog. Circadian rhythms: to sync or not to sync. *Current Biology*, 25(8):R337–R339, 2015.
- [42] James D Meiss. *Differential Dynamical Systems*, volume 14. Siam, 2007.
- [43] Ralph E Mistlberger and Debra J Skene. Nonphotic entrainment in humans? *J. Biol. Rhythms*, 20(4):339–352, 2005.
- [44] Catherine Morris and Harold Lecar. Voltage oscillations in the barnacle giant muscle fiber. *Biophysical journal*, 35(1):193–213, 1981.
- [45] Hiroya Nakao. Phase reduction approach to synchronisation of nonlinear oscillators. *Contemp. Phys.*, 57(2):188–214, 2016.
- [46] Béla Novák and John J Tyson. Design principles of biochemical oscillators. *Nat. Rev. Mol. Cell Biol.*, 9(12):981, 2008.
- [47] Tjeerd olde Scheper, Don Klinkenberg, Cyriel Pennartz, and Jaap Van Pelt. A mathematical model for the intracellular circadian rhythm generator. *J. Neurosci. Res.*, 19(1):40–47, 1999.
- [48] Hinke M Osinga and Jeff Moehlis. Continuation-based computation of global isochrons. *SIAM Journal on Applied Dynamical Systems*, 9(4):1201–1228, 2010.
- [49] Sebastián Risau-Gusman and Pablo M Gleiser. A mathematical model of communication between groups of circadian neurons in drosophila melanogaster. *J. Biol. Rhythms*, 29(6):401–410, 2014.
- [50] Logan Roberts, Tanya L Leise, David K Welsh, and Todd C Holmes. Functional contributions of strong and weak cellular oscillators to synchrony and light-shifted phase dynamics. *J. Biol. Rhythms*, 31(4):337–351, 2016.
- [51] Rüdiger Seydel. *Practical bifurcation and stability analysis*, volume 5. Springer Science & Business Media, 2009.
- [52] Sho Shirasaka, Wataru Kurebayashi, and Hiroya Nakao. Phase-amplitude reduction of limit cycling systems. In *The Koopman Operator in Systems and Control*, pages 383–417. Springer, Cham, 2020.

- [53] Kunichika Tsumoto, Tetsuya Yoshinaga, Hitoshi Iida, Hiroshi Kawakami, and Kazuyuki Aihara. Bifurcations in a mathematical model for circadian oscillations of clock genes. *J. Theor. Biol.*, 239(1):101–122, 2006.
- [54] John J Tyson, Christian I Hong, C Dennis Thron, and Bela Novak. A simple model of circadian rhythms based on dimerization and proteolysis of per and tim. *Biophysical journal*, 77(5):2411–2417, 1999.
- [55] Arthur T Winfree. *The geometry of biological time*, volume 12. Springer Science & Business Media, 2001.